UNIVERSITY OF CALIFORNIA SAN DIEGO

A Nondestructive Evaluation to Impact Residual Strength and Equivalent Crack Size Estimate: Relating a Characteristic Phase Velocity Wavelength to Impact and Through-hole Damages with the Average Stress Through-hole and Ideal Crack Criterion

A dissertation submitted in partial satisfaction of the
requirements for the degree
Doctor of Philosophy

in

Structural Engineering

by

Benjamin J. Katko

Committee in charge:

Professor Hyonny Kim, Chair
Professor Veronica Eliasson
Professor Charles Farrar
Professor Francesco Lanza Di Scalea
Professor Daniel Rudnick
Professor Michael Todd

2023

The dissertation of Benjamin J. Katko is approved, and it is acceptable in quality and form for publication on microfilm and electronically.

University of California San Diego

2023

DEDICATION

For those you came before and set the foundation. For those that guided when uncertainty was prevalent. For those to come, carry this torch forward and never give up.

To Dr. Meow Meow, thanks for being with me up until your end. You have been the best furry friend and our relationship was perfect. I am grateful that you had the chance to live your life on your terms. You had the chance of living many different places and meeting many friends. Your courage in the face of danger and boldness to stand up to it has taught me how to stand up for myself in so many ways. I wish you were here to celebrate, but I know you are around. You send me signs every now and again letting me know that I am doing things right.

EPIGRAPH

There is only experience and its decay.

\- Geoffrey Sonnabend

TABLE OF CONTENTS

LIST OF FIGURES

LIST OF TABLES

ACKNOWLEDGMENTS

The most sincere gratitude to my family, I love you all and am grateful for your unwavering support in the face of uncertainty and challenge after challenge.

The most sincere gratitude to Professor Hyonny Kim. Without your generosity, patience, and wisdom...none of this would have been possible.

The most sincere gratitude to Uncle Walt and Aunt Barb, thank you for the grace, support, and place to rest after a long day.

The most sincere gratitude to Professor Veronica Eliasson, your mentorship and wisdom has been irreplaceable.

The most sincere gratitude to my committee, thank you for your support.

The most sincere gratitude to Dr. Rodrigo Chavez, your attitude and spirit made this process bearable.

The most sincere gratitude to Dr. Heng Liu, your dedication to the craft is a true inspiration.

The most sincere gratitude to Dr. Jeff Newgard, thank you for all the laughs, witnessing me during this process, and accepting me for who I am.

The most sincere gratitude to Dr. Marion Vance, your encouragement to follow my own path was the spark that challenged me to be better.

The most sincere gratitude to New Mexico Institution of Mining and Technology - Mechanical Engineering Department, your team effort in educating the future has made my future bright.

The most sincere gratitude to Professor Irina Alvestad, for being more than my math teach. You taught me how to persist in the face of difficulty.

The most sincere gratitude to Erica Sorenson, your unwavering support through thick and thin is the true definition of Friend.

The most sincere gratitude to Isaac, Esme, and Isla, you are always pushing the limits of what is possible and illuminating the path for so many. You are without a doubt my best friends and I will always admire your zest for life.

The most sincere gratitude to Erica Zygelman and George, your hearts made the hard times bearable.

VITA

2008	B. A. in Exercise Science, Fort Lewis College
2018	B. S. in Mechanical Engineering *cum laude*, New Mexico Institute of Mining and Technology
2020	M. S. in Structural Engineering, University of California San Diego
2023	Ph. D. in Structural Engineering, University of California San Diego

PUBLICATIONS

Cui, Ranting and de Souza, Chaiane Wiggers and Katko, Benjamin J and di Scalea, Francesco Lanza and Kim, Hyonny, ”On-destructive damage localization in built-up composite aerospace structures by ultrasonic guided-wave multiple-output scanning”, Composite Structures, 292, 2022.

Mascareñas, David, et al. ”Augmented reality for enabling smart nuclear infrastructure.” Frontiers in Built Environment 5 (2019): 82.

Tansel, D. Z., Yasui, J. A., Katko, B. J., Marchi, A. N., Wachtor, A. J. (2017). Material characterization of self-sensing 3D printed parts. In Special Topics in Structural Dynamics, Volume 6: Proceedings of the 35th IMAC, A Conference and Exposition on Structural Dynamics 2017 (pp. 149-158). Springer International Publishing.

ABSTRACT OF THE DISSERTATION

A Nondestructive Evaluation to Impact Residual Strength and Equivalent Crack Size Estimate: Relating a Characteristic Phase Velocity Wavelength to Impact and Through-hole Damages with the Average Stress Through-hole and Ideal Crack Criterion

by

Benjamin J. Katko
Doctor of Philosophy in Structural Engineering

University of California San Diego, 2023

Professor Hyonny Kim, Chair

This dissertation focuses on investigating and developing techniques for measuring residual strength estimate of a damaged composites from purely nondestructive signals. The nondestructive evaluation (NDE) system relates an ultrasonic guided wave(s) (UGW) emanating from a structure and reasonably estimates the structures residual strength using the Average Stress Criterion.

The UGW signals are flexural and dependent upon the material properties and plate geometry, which change under impact or some other damaging mechanism and is thus destructively observable as a strength reduction. Correlating strength to signal requires three objectives to be accomplished: 1) Parameterize broadband mini-impactor excitation source, 2) develop algorithm for processing spatiotemporal data for phase velocity information, and 3) relate UGW degradation to physical strength all in the context of Average Stress Criteria.

Parameterization of the mini-impactor hammer, which is a broadband excitation source, was the starting point. Seventy-two design permutations of plate material, thickness, and mini-impactor define the experiment domain. Ten experiments per permutation results in seven hundred and twenty experiments filling the domain with temporally aligned raw data. Temporal and spectral analyses are conducted with the modus: “follow the energy” and found 75% of the analyses agree in terms of significant and deployable permutations to real world applications.

Knowing future data will be spatiotemporal UGW, an algorithm (WAVSVD) uses singular value decomposition to reveal all spatial and temporal patterns, some which are muted in our physical experience. WAVSVD is also used to denoise data. WAVSVD captures more datapoints than traditional 2DFFT and captures the phase velocity and frequency attenuation because of damage. WAVSVD is the UGW processing backbone and helps identifies the max characteristic wavenumber at attenuation as the degrading metric to use in the residual strength estimate.

Impact residual strength can be modeled with Average Stress Criterion. The assumption being that the stress distribution from edge of damage to edge of plate is developed as an Average Stress Criterion mixture of the material degradation and cracking. The Average Stress Through-hole correlates residual strengths of impacts to those of holes, while the Average Stress Crack captures the characteristic shift that needs to occur to relate the damage size to an equivalent crack.

Chapter 1

Dissertation Introduction

1.1 General Explanation of Research

This dissertation explores the question: *How do we estimate the remaining strength of a damaged aircraft with method(s) being straight-forward, field deployable, data-driven, and from noninvasive sources?*

With this question in mind along with my engineering modus of wanting to know how to Make, Break, Model, and Sense structures, a research program was developed. The research program consists of defining and developing a broadband excitation source specific to the material and thickness of the structure being interrogated. The second aspect is developing an algorithm that uses singular value decomposition to reveal hidden patterns in the data that ultimately describe the phase velocity more accurately. Using the excitation source and the revealed phase velocities of damaged laminates and testing for their strength a correlation can be made. This is summarized below.

This research has three main projects:

1. Mini-impactor Parameterization Study
2. WAVSVD Algorithm for Phase Velocity
3. Residual Strength Estimates from Phase Velocity Signal and Average Stress Criteria

This last project having the caveat, as no direct physical relationship exists between residual strength and phase velocity.

1.1.1 Aerospace Materials

All of the experiments conducted relate to the common aerospace industry. As the degree of isotropy increases so do challenges facing the researcher. The reason so much focus is spent upfront on aerospace materials is their a) applicability to the problem being addressed but more importantly it is measurable when observed with ultrasonic guided waves. It is known that the phase and group velocity dispersion relations are developed from transcendental equations with expressions containing the material properties of the plate or shell and it is possible to measure these as a result of an altering mechanism. At the very minimum if a composite is involved, a known isotropic is presented as a ground truth case.

Isotropics

It is common to find aluminum and steel in aerostructures. An excellent example is SpaceX's use of stainless steel in the Starship. These materials are straight forward and described by two elastic properties, Modulus and Poisson's Ratio. Strength and stiffness are well known and pretty straightforward to test for. It is great that so much effort has gone into developing this base of knowledge. This base of knowledge extends so much as to using the 6061 Al phase and group velocity dispersion curves as ground truths for a new method measuring ultrasonic guided waves.

Orthotropic

This is the challenging case. The material properties for the orthotropic case is now nine elastic constants needs to be experimentally determined. Classical Laminate Theory (CLT) is used to develop laminate level model from a representative volume element with known or estimated fiber to matrix ratios and properties. Ultimately the goal is to estimate these properties, for both material types.

When degradation occurs as a result of some damaging mechanism, measuring the degradation with noninvasive means will provide insight into the strength of the laminate with out risking taking the aircraft out of service.

1.1.2 Barely Visible Impact Damage

The aerospace industry has had an on/off relationship with composites with some of the earliest aircraft being wood and canvas to take advantage of the strength to weight ratio offered by the wood. Use of metals such as aluminum and stainless steel

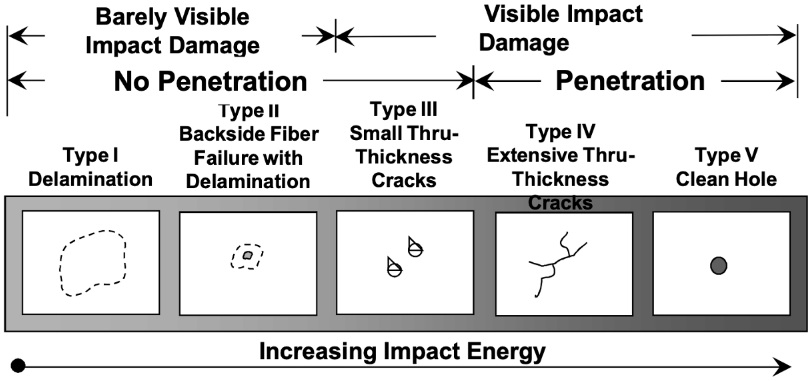

Figure 1.1: Impact Damage Levels. Types II, IV, and V are used to develop BVID impact residual strength relationship to NDE signals

dominated the design sphere around WWII to into the 1970's, though stealth projects were underway as well. The heavy reliance on high-performance metals, interrupted the Design for Fracture approach. Fracture Mechanics itself has been an emerging engineering field since the early 1920's and has not overlapped with engineering composite for long. The increase in material and layup complexity the strength, stiffness, and fracture toughness is all affected and often requires experiments to accurately measure a variable.

In this research, we narrow the domain to Impact Damage.

The Impact Damage Figure 1.1 domain is a spectrum of Damage Types. The Figure is organized hierarchically by impact energy and ranges from I-V. Type V is a Through Hole and Type IV is Through Crack. These two cases are well studied in Linear Elastic Fracture Mechanics. Type II is Barely Visible Impact Damage (BVID) and is very difficult to detect.

BVID has shown to exhibit skin side damages that are nearly non-exisistent nor indicative of the severity of damage that is located internal to the laminate or sandwich structure and/or the internal aerostructure system (HEWABI). A study suggests that 87% of damage on aerospace vehicles are due to impacts. Thus studying impacts are important we are motivated to study BVID and how it relates to many different factors 1) ultrasonic guided waves, 2) Damage Types 3) Damage Size, 4) Residual Strength and 5) Models.

1.1.3 Structural Health Monitoring and Nondestructive Evaluation

Understanding the importance of this research is to understand the initial source, the mini-impactor deployability. In this research the mini-impactor deployment is centered on aerospace structures, we broaden the perspective to the goal of damage detection in materials common to structures. Damage detection is cornerstone to disciplines such as Structural Health Monitoring (SHM) and Nondestructive Evaluation (NDE). SHM seeks an on-line evaluation of the structure with the current system state evaluated against a known baseline state. NDE is similar to SHM, but is typically an off-line technique. NDE also seeks to update the understanding of the damage at a known location which is a priori knowledge (Shull, 2002a).

Regardless of the on/off-line nature of the scheme both exploit the input/output relationship of the structure and prior knowledge to make inferences about the structural state. The motivation being the to delay the inevitable entropic decay of a structure.

If this entropic decay is not considered the structural degradation will be accelerated via environmental and operational mechanisms. For instance tribological effects between components or ion exchange resulting in the corrosion of a metal, such as steel. More rigorously, damage must be defined and will be defined in total agreement with(Farrar & Worden, 2012) *"Damage is the unintentional or intentional changes to the material and/or geometric properties of the system, including boundary conditions and system connectivity, which adversely affect the current or future performance of these systems"*.

An effective statistical pattern recognition program for SHM (Farrar & Worden, 2012) entails:

1. Operational Evaluation
2. Data Acquisition
3. Feature Selection
4. Statistical Modeling for Feature Discrimination

This research is focused on items 1 and 2 of the statistical pattern recognition program.

Operational Evaluation sets the domain for a given structural investigation. This includes justifying the structural investigation in terms of life-safety and/or economics concerns, defining a damage modes hierarchy with emphasis on the critical damage mode, how the investigation will be deployed, and data acquisition limitations.

Of main concern is Data Acquisition, this sets the stage for the quality and quantity of data obtained. Effective observation of the interrogated structure requires deliberate tool selection and is application specific. Any deployed interrogation scheme requires the collected data to be significant relative to non-deterministic signals. Other aspects of data acquisition are the cost of deployment, interval of interrogation, and storage of observations.

The workforce that implements the SHM/NDE program needs to be considered as well. Ideally, the workforce is capable of deploying and maintaining any evaluation system. Realistically, those designing the evaluation program should keep deployment as simple and straightforward as possible. Therefore, the deployment of an SHM/NDE program should be easy to develop, understand, implement, and maintain.

Optimal Baseline Subtraction

In this research, ultrasonic guided waves are selected as the dominant NDE information propagating resource. Propagating bulk or guided stress waves can be used in wavefield analysis, pulse/echo, pitch/catch and other NDE/SHM schemes that seek to reveal features that are indicative of geometric, material, and/or damage discontinuities. Using propagating elastic waves as a signal to evaluate for damage, it is imperative to consider the environmental and operational conditions in which the signal exists. Furthermore, signals indicative of damage can be dominated by other signals (e.g., reflections) which could provide a less accurate analysis of the interrogated specimen.

Considering the potential for a data set to be influenced by something like temperature and maintaining congruence with NDE and SHM foundational principles, it is necessary to perform a comparative analysis between the baseline state and the current state, (Farrar & Worden, 2012), (Shull, 2002a). Comparative analysis is a technique used to isolate signal features that may be indicative of damage from those that are not. Furthermore, it is desired to have an NDE or SHM system that is maximally sensitive to the damage feature(s) while being lean in deployment (Yue & Aliabadi, 2020), (Flynn, Todd, Wilcox, Drinkwater, & Croxford, 2011).

Comparative analysis involves subtraction of some historical baseline state to that of a newly collected health state estimate (Haynes, 2014). Due to the signal and measurement variability, it is possible to have baseline subtraction operation being near-zero but not perfectly zero.

A danger faced when using signals containing guided wave are their sensitivity to environmental and operational conditions (Yue & Aliabadi, 2020). One possible approach to overcoming the environmental and operational conditions that complicate an analysis is building a database of historical baseline data collected while in different environmental and operational conditions to perform an Optimal Baseline Subtraction (OBS). More specifically, temperature variation throughout a day (e.g, diurnal cycle) can alter the physical properties of the structure resulting in a baseline ultrasonic signal that is only valid for that specific environmental condition (Mariani & Cawley, 2021). Geometrically, the temperature change causes plate contraction/extension, density, and thickness to alter the time of flight of the guided waves (Salama & Ling, 1980). This results in an expression of material moduli that are specific to that environment. For example, Classical Laminate Theory requires knowledge about ply thickness to develop the laminate stiffness matrix (Daniel, Ishai, Daniel, & Daniel, 2006). This through thickness change can alter the moduli descriptive of the laminate which directly influences the Lamb wave dispersion curves.

An ensemble of datasets that represent permutations of environmental states allows the practitioner to better chose a baseline to subtract from the current health state (Farrar & Worden, 2012). Being adaptive to environmental conditions while assessing the health of a structure by using OBS minimizes the increased error associated with environmental variability (Mariani & Cawley, 2021).

Using an ensemble of datasets representative of different baseline states is not the only mechanism for performing optimal baseline subtractions. Much work has been performed in developing an optimal baseline subtraction for different scenarios/industries. Fundamental research on wavefield analysis and features indicative of damage, joinery, and/or geometric discontinuities (e.g., material step) is being performed (Tempelman et al., 2022) ,(Gardner et al., 2022) ,(Jacobson, Cummings, Fickenwirth, Flynn, & Wachtor, 2022).

The addition of "maximally" above, implies that a gradient of damage detection/localization techniques are available and are based in statistical analysis. A prime example being the use of a maximum-likelihood estimate of the damage location based upon scatter (Flynn et al., 2011). This technique outperformed seven other likelihood estimates and proves to be robust in damage localization.

The medical industry uses baseline subtraction to uncover features of cellular processes (Wasalathanthri et al., 2020). In a critical juncture of a pregnancy the managing medical professionals use optimal baseline subtraction to enhance the telehealth approach to noninvasive measurements of maternal electrocardiographic and phonocardiographic signals from wearable sensors (Mhajna et al., 2022)

Supervised and Unsupervised machine learning approaches to OBS is presented in (Qing et al., 2022) ,(Miorelli, Kulakovskyi, Chapuis, D'almeida, & Mesnil, 2021), and (Qing, Li, Wang, & Sun, 2019).

In total, when the environmental and operational conditions are of importance when evaluating datasets that are non-laboratory based OBS is a crucial step in the recovery of the true health state of the system under question when levied against its historical self.

1.1.4 Ultrasonic Guided Waves

Propagation of waves can occur in any material, except such extreme waves like gravitational and light which propagate in materials and/or a vacuum. Simplistically, wave transmission is the transfer of momentum from one portion of material to a neighboring portion of material. Inducing wave propagation requires a physical event. This physical event temporarily changes the local density creating a pressure differential and this pressure differential causes particle motion about a neutral point (Shull, 2002a; Ida & Meyendorf, 2019). Therefore, the transport of matter does not occur during this process. An alternative perspective is that energy is transferred from one global position to another, while the material remains local (Thien, Chiamori, Ching, Wait, & Park, 2008) .

Relevant to NDE are acoustic waves that propagate within engineering materials at frequencies greater than the audible range of humans (>20kHz), these waves are termed "ultrasonic". The use of ultrasonic waves in NDE is well established and widely used across many industries. Common applications are flaw and damage detection, damage quantification, material property identification, and medical imagery, to name a few.

Two major classes of ultrasonic waves exist and directly depend on the geometry of the structure being evaluated; they are however described by the same governing equation, they are Bulk and Guided. Consider a structure with significant geometry in three dimensions (i.e. plane strain case) the waves will propagate as Bulk waves. Bulk waves have two wave modes, longitudinal and transverse, that do not vary at a distance from the boundaries as the energy propagates through the structure. More specifically, they are non-dispersive meaning that the phase and group velocities are equivalent and non-changing (single wave packet containing all energy). Mathematically, boundary conditions do not need to be considered (Rose, 2014). Longitudinal stress waves induce dilation within a material and is caused by a stress acting in the direction of wave (energy) travel, this implies that they are normal stresses only. Coupled with Poisson effects, the longitudinal stress wave give rise to orthogonal normal stresses. The normal stresses imply that the particles translate in the direction of the longitudinal stress wave travel and do not cause rotation of the particles.

A structure that has significant geometry in the 1-2 direction with the 3-direction thickness being small (i.e. plane stress condition) and physical boundary conditions considered, then Lamb waves will propagate (Shull, 2002a; Rose, 2014). Lamb wave analysis is difficult because they are infinitely modal, dispersive, and attenuating (Rose, 2004). This thin structure confinement effectively channels and thus guides the propagating waves via critical refraction for each surface/wave interaction (Ida & Meyendorf, 2019). Technically, an isotropic plate has Lamb waves, and a composite laminate has Plate waves (Shull, 2002b), for the sake of continuity, this paper will use Ultrasonic Guided Waves (UGW). Three wave transmission modes occur: Longitudinal, Shear, and Shear Horizontal. Longitudinal stress waves (Symmetric, Sn) propagate along the same direction as the energy propagation and can be converted to shear waves via refraction. Shear stress waves (Anti-symmetric, An) propagate in the out-of-plane transverse direction and can convert to longitudinal stress waves via refraction. Shear Horizontal stress waves (SHM) propagate parallel to the plate surfaces, but do not convert to longitudinal stress waves (Shull, 2002a, Chp.6)

Of importance is the dispersive nature of the UGW because they define expected wave propagation velocities and frequencies within the plate. The UGW velocities are influenced by the plate thickness, the wave's spatial frequency, material properties such as stiffness and Poisson number, and wave mode. An infinite number of modes can exist in a plate-like structure. Dispersion, (i.e. mode conversion) is better understood as the relationship between the Group Velocity vs Frequency and the Phase Velocity vs Frequency. For the sake of mental imagery, refer to Figure 1.2, the Group Velocity, Equation 1.1, is akin to the velocity at which the low frequency envelope travels (think of a surfer riding a wave) and the Phase Velocity, Equation 1.2, are the high frequency carrier waves composing the low frequency, group envelope.

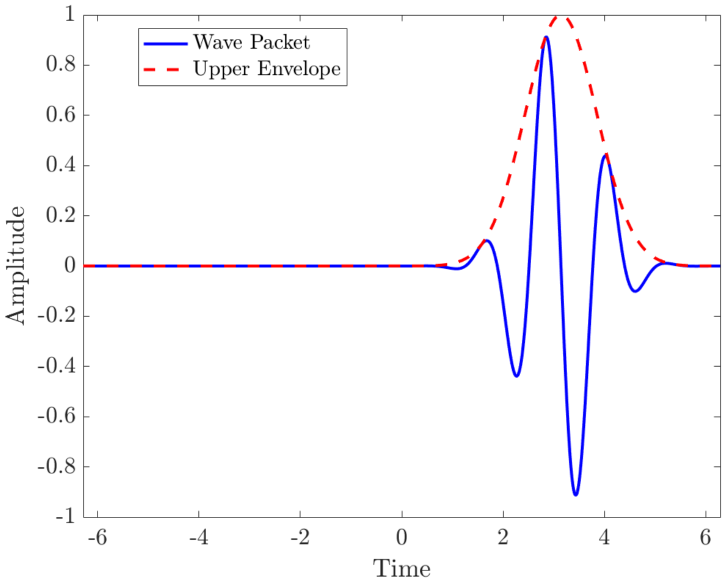

Figure 1.2: Group and Phase velocity example

Mathematically, the Group Velocity is defined as:

$$C_g = \frac{d\omega}{d\kappa} \tag{1.1}$$

and the Phase velocity is defined as:

$$C_p = \frac{\omega}{\kappa} \tag{1.2}$$

If Phase and Group Velocities are equivalent, then the system is non-dispersive and the wave behavior collapses back down to constant longitudinal and shear wave velocities characteristic to that material. Traditional NDE exploits the constant longitudinal and shear wave velocities for anomaly detection and material property identification. A tool that might be used to identify these characteristics could be a Modal Hammer or a Contact Transducer.

Building upon the Single Input, Dual Output scheme (Capriotti & Lanza di Scalea, 2020) and the very similar Single Input, Multiple Output presented in (R. Cui, 2021), (Kralovec & Schagerl, 2020), along with a tunable angle approach to target specific Lamb modes, such as was performed in (James, Mei, & Giurgiutiu, 2020). A Lamb scan approach that marries these techniques for guided wave measurement is feasible.

1.1.5 Singular Value Decomposition in Review

Engineering and science researchers are exploiting the mathematical operation in unique and clever ways. In this research we seek to estimate the phase velocity of A_0 mode and have developed and algorithm, WAVSVD, to do so. It relies heavily on SVD to accomplish its task. The algorithm's general flow: The outer product of the rank-reduced unitary matrices, which respectively encode an estimate of the temporal and spatial patterns is performed. This step exploits an interesting opportunity to correlate the tailored basis patterns in space and time without influence by the scaling singular values. This outer-product produces a spatiotemporal cross-covariance matrix unrestricted by the singular values which could prohibit mode feature(s) identification and is exact to this data set. It is important to note that prior to the second SVD, the outer product preserves the original dimension of the data as the inner matrix dimensions are the selected rank while the outer dimensions are the original data set size. The spatiotemporal cross-covariance matrix is passed through the SVD a second time and rank-reduced via a second threshold to denoise the data prior to data set reconstruction. After the reconstruction, the 2D power spectrum is calculated from the 2D Fast Fourier Transform (FFT). The wavenumbers and frequencies corresponding to the Lamb mode(s) are extracted and used to estimate all corresponding phase velocities. With this context we frame our use of SVD in the realm of other research.

Bioinformatics and medical imagery researchers seek to enhance identification anomalies, whether structural or electrical and exploit SVD to help achieve this goal. A common theme is denoising and decluttering signals and images with SVD reconstructions (Wall, Dyck, & Brettin, 2001), (Henningsson & Fontes, 2019), and(Demené et al., 2015) along with a confidence metric for the thresholding step (Wall et al., 2001). A general linearized model for structure within EEG signals was formulated using SVD (Harner, 1990). Cross-correlations were passed to the SVD algorithm for localization of target vesicles in an ultrasound environment (J. Kim, Hwang, Rho, & Yoon, 2020). Similarly, a covariance matrix of ultrasound signals is passed to the SVD algorithm for decluttering and development of a coherence "statement" between spatial and temporal components and(Demené et al., 2015). In the theme of correlations, researchers in the electrical engineering domain exploit the SVD of a 2D correlation for receiving angle estimates (Gu & Wei, 2007).

The Oil and Gas industry have used SVD to even forecast carbon prices using a multi-resolution SVD and machine learning approaches (Sun & Zhang, 2018) The environmental researchers have exploited SVD in approaches such as EOF. Other researchers seek to add the outer product of the spatial and temporal matrices to the SVD as a linear term and replaces other aspects of the spatiotemporal matrices with a model for enhanced resolution of temperatures across Sicily (ONORATI, Sampson, Guttorp, et al., 2013). Chemists use SVD for modeling of a distributed parameter system when the system is sparse (L. Chen, Li, & Yang, 2020).

Nondestructive Evaluation (NDE), which is an off-line monitoring scheme, employs SVD to identify a robust indicator of damage in noisy environments (X. Cui, Wang, Kang, Pu, & Deng, 2018). The singular vectors are also investigated and realized as approximations of the impulse response to a source and used to color a spatiotemporal image. Like NDE is Structural Health Monitoring (SHM), which is an online scheme and tends to incorporate machine learning for damage detection/localization/ prognosis. SHM uses SVD for as an operation and a feature source(s) for damage detection (Farrar & Worden, 2012). Exploiting DORT-MUSIC operations to image subwavelength damage in isotropic plates (J. He & Yuan, 2016). Lamb wave mode decomposition and rank-reduced reconstruction estimates following viscoelastic wave models (Cao, Zeng, & Lin, 2021), separating MIMO signals, perform time reversal operations (J. He & Yuan, 2016), (Farrar & Worden, 2012), and (Q. Chen, Xu, & Ta, 2021), only to name a few.

Ultrasonics is a generalization of NDE and SHM but can lead to researching similar goals. Obtaining high-resolution Lamb wave dispersion estimates for material property identification (inverse problem) (Q. Chen et al., 2021). Using UGW for localization of dual emitting damage sources (T. He, Xie, Shan, & Liu, 2018) and phased array imaging of attenuative materials (Rao et al., 2022). Damage detection for under complex environments was explored and very applicable to structures and mechanisms (Liu, Harley, Bergés, Greve, & Oppenheim, 2015). Furthermore, phase velocity measurements from a multi-emitter and multi-receiver array were found using SVD in the frequency domain (Minonzio, Talmant, & Laugier, 2010). Sparse SVD has been used for high-resolution extraction of dispersion curves via guided waves [8]. A transfer matrix approach is used for mode identification from a MIMO system (Minonzio, Talmant, & Laugier, 2011).

Assertion of Novelty Generally, SVD is a common analysis procedure with a lot of applicability to the sciences in breadth and depth. This literature review casts a wide net to identify if researchers have performed operations like the presented novel procedure. At the core of the novel procedure is this decomposition, rank-reduced outer product of the spatial and temporal matrices, the singular value decomposition of the rank-reduced outer product, and construction of the reduced-rank dataset. More concretely, this presented procedure is anomalous to the traditional signal processing procedure of moving from time series domain to correlation domain to the frequency domain but not yet observed as a possibility via the repeated SVD. The presented procedure is a reduced-rank outer product between the spatial and temporal patterns. The SVD of the outer product of U and V^* matrices minimize the noise in the procedure, while also eliciting more clearly spatiotemporal patters previously unidentifiable, i.e. increases the bandwidth within the wavenumber-frequency diagram. Furthermore, it is a disadvantage to incorporate the singular values until the final reconstruction as they can unreasonably decimate aspects of the matrix product. The result of this procedure results in the classical denoised and decluttered data while unbiasedly eliciting significantly stronger spatiotemporal patterns within the dataset.

The enhanced spatiotemporal information preserved at the end of the novel procedure is used to calculate the wavenumber-frequency plot. The power spectral perspective further rewards significant modes of interest while decimating insignificant features (noise artifacts), thus making mode extraction robust and clean. Thus, the analysis procedure will be termed WAVSVD.

What is SVD?

Singular Value Decomposition (SVD) is a mathematical operation that, at its simplest, can be used to reduce a high-dimensional data set into a lower dimensional data set estimate. SVD is a numerically stable and a hierarchically ordered tool excellent for identifying patterns in data (Brunton & Kutz, 2022). This linear algebra operation is made possible with modern computers and is an important tool for a data scientist to deploy. SVD is applicable to datasets composed of intelligently collected data and it is applicable across many engineering and science domains. Traditionally and most commonly, this technique is executed to reduce dimensionality and computational cost while preserving significant features within a dataset. Other applications of the SVD are calculating the pseudo-inverse of non-square matrices, provides solutions to under/over-determined linear equations, and denoise data (Brunton & Kutz, 2022). A subtle but valuable realization of SVD is that it produces a data-driven tailored basis whereas, for example, the fast Fourier transform provides a generic basis.

Two examples are presented to highlight some of the strengths of the SVD, how they can be deployed, and how they are exploited and combined in the WAVSVD algorithm. The first example is the use of SVD to compress an image for storage and transmission at lower computational costs relative to the original, non-compressed image. This example is motivated from (Brunton & Kutz, 2022). The second example indicates how periodicity can be orthogonalized from an image and cast as a correlation representation. The two examples do not exactly represent the WAVSVD but provide a tangible understanding of how the WAVSVD algorithm utilizes these two attributes of the SVD for signal analysis.

Example 1 - Image Compression

Shown is an example of how SVD is used in practice for data size reduction while preserving dominant information. This can also be thought of as a denoising operation because many datasets/images are so rich with data that not all patterns are required to describe fully the original image/data set. (Brunton & Kutz, 2022) provides an excellent description of this and example, this paper briefly reiterates their example. Briefly stated, high-resolutions provide excellent photos but at zoom into a local pixel region and the image looks like “noise”. This noise does not contribute to the entire domain in a significant way and can be removed via SVD. Truncating the dataset to denoise the image prior to reconstruction is valid and reasonable.

In this example an image is compressed/denoised using SVD, see Figure 1. Rank-reduced versions of the full image are generated. What is meant by rank-reduction is that a subset of the singular values and their corresponding singular vectors are preserved for reconstruction. The point being to highlight how selection of rank (singular values and corresponding singular vectors) allows the image to be reconstructed at various levels of quality. The general theme is this: The lower the rank chosen, the less the reconstruction resembles the original image. The higher the rank selected, up to full rank, the image is more completely reconstructed. At a of rank = 500 (1/6th of full rank), the image is nearly indistinguishable from the full rank image, but at a fraction of the storage space.

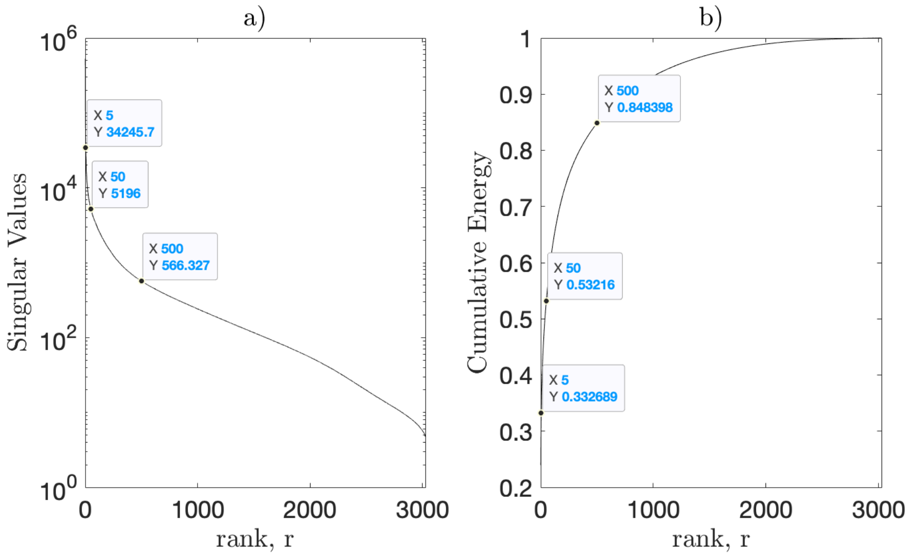

Figure 1.3: a) The singular valuesa re in descending order along with their respective rank. b) The cumulative energy measured from the singular values and normalized. The point of a) and b) are to highlight how the singular values and their rank relates to our experiencing the photo

The left graph in the Figure 2 below indicates how the SVD hierarchically organizes the singular values. Note that the organization is nonlinear and thus a truncation can be applied to select a rank. This is indicated on the right graph, the cumulative energy of all the singular values with cumulative energy levels at each rank. Another perspective to take with respect to hierarchically organized singular values are their representation of variance at each level and the highest variance is associated with the initial singular values while lower variance is reserved for the last singular values. The hierarchy essentially organizes the information that can be used to estimate the image with the initial singular values being best at estimation while the last singular values do not estimate the image (data set) significantly.

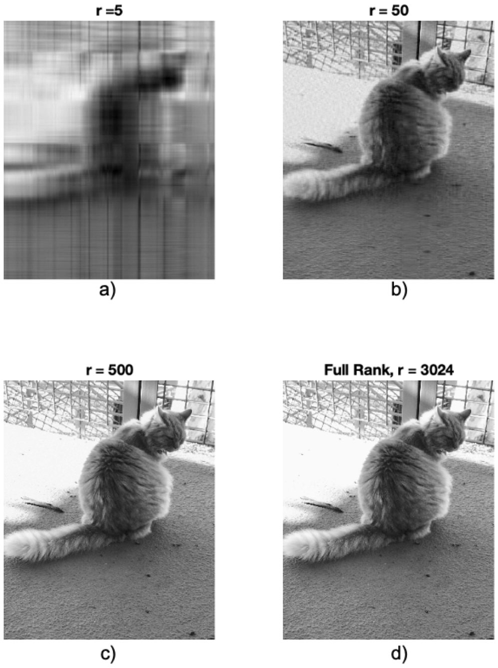

Figure 1.4: a) When only 5 singular values (rank =5) the recreation of Mr. Meow Meow is poor. b) and c) increase in resolution as the rank increases. d) The original image, notices how c) and d) are near indistinguishable? This is at the core image (data) compression.

Therefore, this corroborates the assertion that not all singular values and their corresponding singular vectors are required to represent the image and only a well selected subset can be used for reconstruction.

Example 2 - Periodicity and Correlation

An interesting extension of the SVD is its natural ability to extract and distribute patterns from a multidimensional dataset, in this case an image of artistic waves. Envision the waves in the image representing a snapshot of the same wave at different periods of time. This is like the signals collected and stored in this research, but not exactly. The reason it is not exactly is the image doesn't align perfectly with each wave pattern in the column space. The point remains the same, however, being that the SVD is capable of extracting patterns from a dataset that are orthogonal to each other.

Figure 1.5 is an artistic representation of waves. What is important about this is the periodic behavior inherent in the art. This periodicity can be decomposed using SVD.

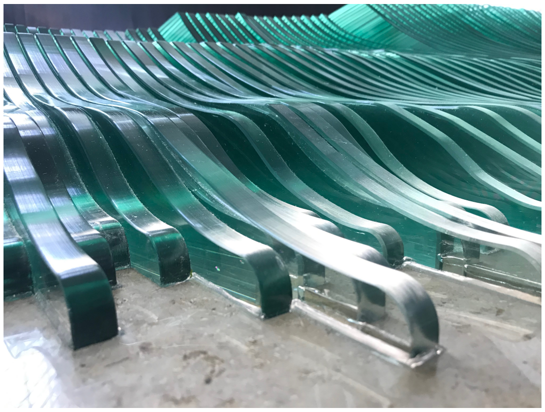

Figure 1.5: - Singapore Waves

Figure 1.6, below, indicates the SVD of the Periodic Waves image and decomposes the image into two unitary matrices, U and V^* (where * represent conjugate transpose).

The outer product of $U \otimes V^*$, which is essentially a cross-covariance representation of U and V^*, and the original image itself. This operation is performed in the tailored basis space, which is data-driven.

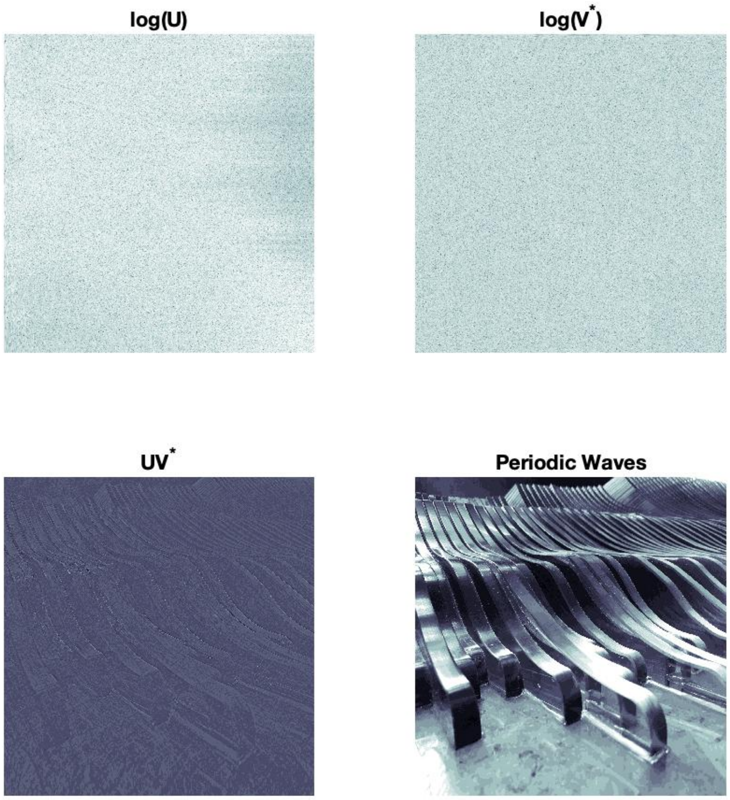

Figure 1.6: An example of the spatial patterns that are ”evolving” and what the WAVSVD the outer-produc results in, bottom left

For this example, the unitary matrices are not fully indicating the spatial patterns as the photo is not an image from directly above with each wave being aligned vertically. However, patterns are clearly observed in the U matrix and less so in $V*$

matrix. The outer product of the two matrices generates a ghostly representation of the original images but only is highlighting periodicity that is correlated between the two dimensions.

By combining the two examples, 1) image compression and 2) periodicity and correlation and aligning each timeseries experiment into the column space of the data array, X, the WAVSVD algorithm combines and exploits the attributes of both methods generating an excellent novel approach for researchers to cleanly extract representations of the periodicity in a spatiotemporal data set. This approach is intelligent, tailored, and a data-driven approach that is guaranteed to exist and is stable (Brunton & Kutz, 2022).

1.2 Brief Research Synopsis

1.2.1 Mini-impactor Parameterization Study

From the Mini-impactor Paramterization, Chapter2.1, specific Mini-impactor hammers are suggested for specific permutations of aerospace material and plate thickness. 72 experimental permutations define the experimental parameterization domain. Being uncertain in the initial spectral domain parameterization outcome, a second temporal domain analysis is conducted. Both analyses are grounded in ”following the energy”. At the conclusion of the study, both analyses suggested 75% of the same permutations. A research goal being to develop a Mini-impactor Deployability Table. Two major Perspectives with suggested deployments are: 1)

Universal and 2) Material-Thickness. The Universal Perspective suggests a single MI for any deployment. This is the "do it all" MI. It is MI #1 which is $38mm$x$[0_4]$ with aluminum shims. The second is a table and can be found at the end of Chapter2.1.

1.2.2 WAVSVD Algorithm

Between the giving WAVSVD the raw data and receiving the phase velocity information, numerous mathematical steps exist. Some of these steps are advantageous in an algorithmic sense. This algorithm is centered around Singular Value Decomposition (SVD), Chapter 1.1.5. SVD is a power mathematical tool that can decompose a matrix into two matrices which are orthogonalized with x direction patterns allocated to the first orthogonalized matrix and the y-direction for the second orthogonalized matrix. The center matrix is diagonalized and contains singular values. They are weights that amplify or diminish the matrix product of the two orthogonalized matrices.

For instance, this data set consists of space and time data, they are arranged in the space-time plane with amplitude being the z-direction. When decomposed the spatial patterns are extracted and allocated to one of the two unitary (orthogonalized) matrices in the decomposition. The other unitary matrix receives the temporal patterns descriptive of the experiments. The center diagonalized decomposition matrix is the matrix of singular values (weights). Operating of the outer product of the unitary matrices and cleansing the data allows for an estimate of the original data set without the weights (singular values).

The reconstruction of the original data set with the weights removed i an enhanced view of the spatiotemporal wave development. This enhanced view of spatiotemporal information is better represented in the wavenumber-frequency domain. This spectral domain is queried for the background content magnitude and significant wavenumber-frequency, $C_p = \frac{\omega}{\kappa}$ plotted as phase velocity vs circular frequency.

A second major observation occurred, that being hole specimen's phase velocity curve for a CFRP also exhibited this truncation effect. Interestingly, this also leads to an important yet familiar third major observation, that being the impacted specimen's phase velocity curve exhibited this truncation behavior too and perhaps there is a relationship to the Average Stress Criteria Through-hole case

1.2.3 Impact Residual Strength

With the goal of correlating NDE signals to strength data via a physical metric that degrades as a a result of damage. The NDE characteristic wavelength is a reasonable substitute for the Average Stress Criteria's characteristic damage size. This is backed by the observation that for both impacts and holes, phase velocity attenuates. The characteristic wavelengths are on the order of mm and reasonably constant. When using the destructive data with the substituted characteristic wavelength, half damage size, and fracture toughness for a similar sized specimen, then the impact residual strength correlation is completed by using the Average Stress Analysis for a Through-hole as a framework.

1.2.4 Novel Contributions

1. Mini-impactor Parameterized Deployability Suggestions -

   After performing 720 total experiments for 72 possible permutations and analyzing the data nearly 11.5 million data points for meaningful permutation related to energetic excitation, two perspectives are developed that state which permutation of mini-impactor, plate material, and plate thickness is best combined. The second perspective is the most universal impactor, this perspective is the mini-impactor that consistently performed well for most materials and thickness.

2. Developed WAVSVD algorithm to reveal more wavenumber-frequency content that is typically hidden by singular values

   Recognizing that the spatial and temporal patterns are separated into two unitary matrices with the singular values being the scaling, diagonalized matrix. Removing the influence singular values have on the patterns we typically observe, the reconstruction of the data set shows an expansion of bandwidth. This results in a better revealed experimental estimate of the phase velocity.

3. A process for correlating impact damage to UGW via characteristic length , a_κ

   Observing the phase velocity attenuation that occurs when ultrasonic guided waves propagate around a hole and the phase velocity attenuation of UGW that propagate through and around damage, it is realized that the presence of gross material degradation prohibits some frequency content from being excited or observed because of scatter. It is found that Average Stress Criteria is a suitable framework that is linked to Fracture Toughness. The similar degradation and fact that the characteristic wavelengths a_o and a_κ are interchangeable and led to the reasonable approximation of the impact and open hole residual strengths.

4. Defining a crack correctionfactor that locates the residual strengths at an equivalent crack (which is also correlated with a hole)

Considering the hole and the crack Average Stress Criteria are correlated, it is reasonable to assume so are the impact now that impacts are correlated with the through-holes. Using the Crack criterion, a correction length is found that takes the current half impact damage size and shifts the residual strength to that of an equivalent. This is actually the complete correlation, while the 3) is only correlated in strength.

Chapter 2

Parameterization of Mini-impactor Excitation Tool

2.1 Abstract

In this study a novel nondestructive impacting excitation tool is presented. The value of this impactor device is it's capability of exciting materials typical of aerospace structures into the hundreds of kHz frequency range, which is well beyond traditional impact hammers ($< 40kHz$). The proposed(H. S. Kim, 2020) impactor is a lightweight, carbon fiber reinforced polymer cantilever beam with a metallic tip. Colloquially, this impactor tool is termed "Mini-impactor." Defining the paramertization space, six versions of the mini-impactor, four plate materials, and three different plate thicknesses lend to a total of seventy two experimental permutations. The experimental domain includes ten experiment repetitions for each permutation. In total seven hundred and

twenty experiments comprise the dataset. Two independent data analysis approaches bolster the inferences found lending confidence of the mini-impactor's deployment to real-world applications. The common theme between signal analyses was to "follow the energy."

The first data analysis technique involved staying in the time domain and gating the signals at the first arrival of the anti-symmetric stress wave packet. A Normalized Residual Energy (Haynes, 2014) metric was used. The Normalized Residual Energy of a group of data is compared to a single experiment's relative energy. Ultimately this is the ratio of the sum of squares of the normalized and average of all data with the sum of squares of the individual normalized signal. A threshold of one standard deviation is applied to the relative energy identifying the permutations which exceed that level and are thus significant. Any permutation below the threshold is considered insignificant.

The second data analysis technique involved casting the time series signals into the frequency domain via the Welch method resulting in power spectral densities. An organized matrix factorization of the spectral data matrix, from highest energy to lowest energy, allowed for the dataset's global noise reduction and to be rebuilt for a statistical sorting. From the statistical sorting, non-influential ($< 90\%$ significance) permutations were excluded from consideration. This process resulted sin a suggested permutation for each base material and thickness permutation.

Both analyses found, with strong agreement (75% similarity), the permutations (mini-impactor, plate material, and thickness) that are best suited for deployment. Furthermore, this deployments are from the perspectives of universality, structural material, and structural thickness.

2.2 Introduction

Evolving needs for lightweight and nondestructive evaluation of aerospace structures, especially from the external surface only, have driven demand for enhanced interrogation tools. While many significant advances have been made in damage detection, location, and severity quantification, lesser advances have been made in development of excitation sources that effectively impart energy revealing higher frequency content (≥40kHz) of an aerospace structure. Cumbersome deployment, whether that is hardware, attachment, and/or deployment requirement(Sarafin & Larson, 1995),(Farrar & Worden, 2012), are reduced with the mini-impactor.

Traditional impact hammers apply a short duration impulse to a structure. However, the limitation being a low level of excited frequencies ($< 40kHz$) (Liu, Zang, Li, & Petrov, 2020). Considering this limitation, it is realized that the low level of excited frequencies are suitable for gross damage detection (Ida & Meyendorf, 2019) but fail to specifically locate more complicated damages modes such as delamination or embedded damages. These complicated damages are not gross in dimension but will reduce the life of the structure. Any wavelength greater is size than the damage will simply pass by the damage, it wont be detected.. Clearly this is unattainable by traditional hammers.

Turning to the current state-of-the-art excitation modal hammers which include Inertial and Rotary, Mechatronic-Flexible, and Pile Driver designs (Blaschke, Schneider, Kamenzky, & Alarcón, 2017; Steinbauer, 2018; Singh & Moore, 2021; Maierhofer, Mahmoudi, & Rixen, 2020), these excitation sources are not yet capable of exciting frequencies required to resolve signatures of sub-millimeter size damages in any significant and in some cases repeatable manner. A Rotary-esque impact hammer was observed by this researcher at a local engineering company, the repeatability was suitable enough for these engineers, but only for that application.

The limitation in excitation frequency is in direct contradiction to the critical damage modes associated with aerospace structures that have experienced low energy impact(s) producing damage which can only be revealed by frequencies in the hundreds of kHz (Capriotti, 2019; H. S. Kim, 2020). High frequency techniques include permanent bonding of low-profile transducers (piezoelectric patches) to aerospace structures for on-line monitoring(Farrar & Worden, 2012). This is a challenge for external aerospace surfaces cannot support this kind of transducer/receiver network deployment because of the extreme environment and additional system weight. Additionally, traditional high frequency techniques require equipment to excite transducers, such as a piezoelectric patch or laser vibrometers, and could require amplifiers, power supplies, and other hardware. This is not ideal and therefore due to weight and power setup times can be extensive (Sarafin & Larson, 1995), a design space has been identified and filled through the parameterization and suggested deployments of the novel mini-impactors.

The mini-impactor excitation tool exploits the proportionality of tip hardness and beam mass. Using this proportionality, the mini-impactor overcomes current exciter limitations. The mini-impactors are manufactured from unidirectional carbon fiber prepreg with an aluminum tip. The mini-impactor beams were first approximated using mathematical models to identify the respective beam's stiffness and natural frequencies. The waveguides are representative of aerospace structures and consists of four plates materials: 6061-T6 Aluminum, Heat Treated Steel, Carbon Fiber (Hexcel 282 3K/Kaneka GR6862), and (EGlass 7781/Kaneka GR6862).

Six versions of the mini-impactor, four plate materials, and three different plate thicknesses leads to seventy two experimental permutations defining the experimental domain. Experimentation consisted of selecting a impact excitation of the plates and recording the time series impulse response with a R15s AE sensor (Mistras). To ensure that the appropriate ultrasonic guided waves being observed and recorded consistently, a simple switch circuit was used to trigger the oscilloscope at the moment of impact. Building the dataset involved repeating the experimental process ten times for each permutation leading to seven hundred and twenty experiments performed and over eleven million data points collected.

The first data analysis technique involved the time domain. Two perspectives were evaluated. They are the systemic level (global) and the particular level (local). The global perspective sought to identify the significant universal permutations, while the local perspectives sought to identify permutations directly relevant to material type and thickness. To achieve this, the common analysis framework involved preprocessing the time series data so that only the anti-symmetric stress waves were considered. This involved gating and windowing the signal. Each perspective was evaluated for a baseline signal (average). The baseline average was removed from the corresponding experiment, within that perspective, yielding a signal residual. The null hypothesis is the baseline average experiment for that perspective. A detector was established and is rooted in a Gaussian probabilistic framework. The detector leverages the ratio of the experimental signal residual's probability density function with that of the baseline signals probability density function. By doing so an energy ratio metric is established. The metric is termed "Normalized Residual Energy" (Haynes, 2014). Identification of the significant experiments required calculating the mean and standard deviation of that perspective. Any experiment greater than one standard deviation was considered significant.

The second data analysis technique was performed in the spectral domain from the perspective of Power Spectral Density (PSD). The dataset was structured into categories of plate material, thus four sub datasets were constructed out of the total dataset. The covariance matrix (16004x16004) was calculated from mean-centered spectral dataset matrix (180x16004) and factored via Singular Value Decomposition for each material category. This technique decoupled the experiments into 180 orthogonal components whilst maintaining correlation. By utilizing the covariance matrix, the decomposed centeral matrix results in the eigenvalues (variance). The variance, in this instance, can be abstracted to signal energy. The factorization of the covariance matrix provided an opportunity to organize the relevant PSD components that are significant relative to the mean PSD. Hotelling's T^2 metric was used to locate experiments relative to the null hypothesis (mean PSD). If a permutation happens to be similar to the null hypothesis (mean signal) the permutation is considered insignificant. The top 10% of significant experimental permutations were found and organized into the deployment perspectives of universality, structural material, and structural thickness.

This dual and independent data analysis approaches, rooted in versions of signal energy, strengthens the inferences and reinforces applicability of the mini-impactor to structural interrogation of aerospace structures.

2.3 Theory

2.3.1 Impact Hammer Design

In the perspective of excitation sources, it is reasonable to assume that an impact hammer can be tailored to a specific application or a domain of applications/deployments. An impactor design directly influences the duration and magnitude of the applied impulse. A structure's response to an impactor is inversely proportional to the impactor mass and directly proportional to impactor tip hardness. Excitation of high frequency content (hundreds of kHz) within a structure requires the a low impactor mass and the impactor tip, at contact, to have sufficient momentum and hardness. Alternatively, to assertions made by (Halvorsen, Brown, et al., 1977) and (Ida & Meyendorf, 2019) chose to manipulate tip stiffness rather than impact hammer mass to excite different frequency content within a structure. From this perspective, it is apparent that if an impactor tip is chosen to be metallic or more generally sufficiently stiff (e.g., Delrin), then the impulse duration does not differ significantly (Halvorsen et al., 1977). This broad choice of tip material generally leaves room for improvement with respect to impactor mass. Regardless, both indicate excited structural frequencies up to 500kHz range. It is important to note that in both resources, the impact hammer resembles a traditional hammer (i.e., stiff handle with a rigid impacting body), which is also a constraint upon the elicited frequencies.

2.3.2 Welch's Method

Modern computation has revolutionized the data analysis, in this instance researchers sought efficient ways to approximate a signal's periodogram. In the 1960'san algorithm was developed to exploit the Fast Fourier Transform (FFT) for estimation of the signal's power spectra (Welch, 1967). The technique involved sectioning, performing the FFT on each section, estimating the section's periodogram, and averaging the periodograms together to approximate the the power spectra. This method is termed Welch's Method. The underlying assumptions of the Welch's method are that the signal is stationary, second-order stochastic and the ensemble of the signal has zero mean. In making these assumptions the following can occur:

Let the total signal be $\mathbf{X(j)}, where j = 0, ..., N-1$ from this total signal we segment and potentially overlap the segments into length of L of the original data sequence. The first segment is:
$\mathbf{X_1(j)} = X(j),\ where\ j = 0, ..., L-1$ likewise we can express the sequence of K

segments as with the understanding that $(K-1)D+L=N$):

$\mathbf{X_2(j)} = \mathbf{X_2(j+D)},\ where\, j = 0, ..., L-1$

$\mathbf{X_K(j)} = \mathbf{X_K(j+(K-1)D)},\ where\, j = 0, ..., L-1$

Now that the data has been segmented and overlapped, each segment's periodogram can be approximated using the discrete Fourier transform. A window $\mathbf{W(j)}$ $j = 0, ..., L-1$ where can be applied and forming $\mathbf{X_1(j)W(j)}...\mathbf{X_K(j)W(j)}$.

$$A_k(n) = \frac{1}{L}\sum_{j=0}^{L-1}\mathbf{X_K(j)W(j)}\exp^{\frac{-2kijn}{L}} \tag{2.1}$$

Moving from the Discrete Fourier Transform (DFT) to a single windowed and overlapped segment periodogram involves squaring of the DFT and normalization by the windowing, resulting in:

$$\mathbf{P_k(f_n)} = \frac{L^2}{\sum_{j=0}^{L-1}\mathbf{W(j)^2}}|A_k(n)|^2 \tag{2.2}$$

where $k = 1, 2, ...K$.

Obtaining the spectral estimate of the power spectra involves averaging all $P_k(f_n)$ estimates:

$$\mathbf{\tilde{P}_k(f_n)} = \frac{1}{K}\sum_{k=1}^{K}\mathbf{P_k(f_n)} \tag{2.3}$$

2.3.3 Principal Component Analysis

Singular Value Decomposition (SVD) is one of the most powerful mathematical techniques of the computational era (Brunton & Kutz, 2022). Excellent commentary on SVD can be found in (Brunton & Kutz, 2022) and a short excerpt is provided. *Applying the SVD algorithm to* $n \, \text{x} \, m$ *yields a numerically stable decomposition that is guaranteed to exist.* Typically, the dataset is a tall,skinny matrix $n >> m$. Each column is an experiment and every row is a measurement of the experiment.

$$\mathbf{X} = \begin{bmatrix} | & | & | & | \\ \mathbf{x}_1 & \mathbf{x}_2 & ... & \mathbf{x}_m \\ | & | & | & | \end{bmatrix}$$

The values of **X** could be complex and measurements from experimentation or other data sources.

$$\mathbf{X} = \mathbf{U}\mathbf{S}\mathbf{V}^* \tag{2.4}$$

Both $\mathbf{U}_{nxn}$ and $\mathbf{V}_{mxm}$ are unitary, meaning the the complex conjugate unitary matrix multiplied (left or right) by the non-complex conjugate matrix, will result in the identity matrix, **I**. The center matrix **S** has non-zero values along the diagonal. If $n \geq m$ then the **S** will potentially have m non-zero values. This stability and guaranteed existence of the decomposition achieved by SVD algorithm is the backbone to the success of Principal Component Analysis (PCA).

PCA is a data-driven technique that seeks to hierarchically decompose a potentially high-dimensional and correlated dataset into its most statistically significant components. The decomposition results are all orthogonal (independent) while maintaining correlation.

SVD is deployed to achieve this. Mathematically, PCA is the energy-ranked variance of the SVD of the dataset's covariance matrix,$\mathbf{C}$.

$$\mathbf{B} = \mathbf{X} - \bar{\mathbf{X}} \tag{2.5}$$

$$\mathbf{C} = \frac{1}{n-1}\mathbf{B}^*\mathbf{B} \tag{2.6}$$

$$\mathbf{C} = \frac{1}{n-1}\mathbf{B}^*\mathbf{B} = \mathbf{USV}^* \tag{2.7}$$

Extracting the non-zero diagonals from $\mathbf{S}$, we can recognize that these are the eigenvalues of the decomposed covariance matrix, but more usefully, these are the variance of the covariance matrix. Performing the cumulative sum of the variance results in the cumulative energy of the system. It is common to find a truncation point such that only a select Principal Components (PC) are needed to sufficiently describe the dataset. For instance, all of the hierarchically ranked singular values (or principal components) that cumulatively sum to an energy of 95% are maintained and used for reconstruction.

2.3.4 Hotelling's T^2 metric

This metric statistically improves our understanding of the significance of each principal component relative to the center of the dataset. Being distant from the center represents a significant experiment, while being near the dataset centroid results in being insignificant.

$$\mathbf{T^2} = \frac{(\mathbf{\bar{x}_k} - \mu)\mathbf{C}(\mathbf{\bar{x}_k} - \mu)^{\mathbf{T}}}{n} \tag{2.8}$$

High statistical significance results when $\mathbf{\bar{x}_k} \gg \mu$. This implies that the null hypothesis is the dataset centroid and when the the measurement is at the centroid, then significance is not present as their is no difference between the mean of the dataset and measurement. More significantly is when the measurement is distant from the centroid.

2.3.5 Normalized Residual Energy

Pursuing a metric that represents data effectively is not trivial. A metric must be identified that represents the data significantly. To achieve this, the process began using signal detection theory and the metric's inspiration stemming from (Haynes, 2014).

In general, Detection Theory seeks to differentiate information-containing signals from non-deterministic (e.g. noise) containing signals (McDonough & Whalen, 1995). In the context of this research, the signals being evaluated are either "energetic" or "non-energetic". This is congruent with the analysis modus of "Following the

Energy".

In this research, the signals are assumed to be linear that re not influenced by non-linearities (i.e. no physical phenomena like crack opening/closing). This is a reasonable assumption as the signals being observed,$\mathbf{y}$, are filtered($\mathbf{h}$) versions of the input, $\mathbf{x}$, signals with additive white noise, $\mathbf{n}$.

$$\mathbf{y} = \mathbf{hx} + \mathbf{n} \tag{2.9}$$

The noise, $\mathbf{n}$ is assumed to be "white", that is, from one sample to any other sample in time, the correlation between the two samples is zero.

$$\mathbf{R}[\mathbf{n}(\mathbf{t_k})]\mathbf{R}[\mathbf{n}(\mathbf{t_{k+m}}) = 0 \tag{2.10}$$

, where $\mathbf{k}$ is the time step and $\mathbf{m}$ is the shift operator.

Furthermore, the intensity of this random process is constant, which is best observed in the Power Spectral Density domain, which is shown to be a horizontal, non-sloping spectra, hence "white". A solid explanation of the statistical assumptions can be found in (Haynes, 2014).

The procedure at which to develop the detector is as follows

1. Collect Raw Data
2. Isolate the A_0 wavepacket via windowing

3. Calculate baseline average signal from all pertinent signals

4. Subtract baseline average signal from the single signal of interest, in this case a permutation

5. Envelope the signals with a Hanning Filter

6. Perform sums of squares of the windowed and filtered baseline average signal $\mathbf{x}_{baseline}^2$ and the windowed and filtered permutation signal $\mathbf{x}_{permutation}^2$ to obtain respective energies

7. Normalize the permutation's energy with that of the baseline average energy

$$\mathbf{NRE} = \frac{\sum \mathbf{x}_{permutation}^2}{\sum \mathbf{x}_{baseline}^2} \tag{2.11}$$

The Normalized Residual Energy, Equation 2.11, is developed for the global and local perspectives. To determine some level of significance vs insignificance, the first standard deviation was calculated for each respective perspective. Any of the permutation's NRE that exceeded the first standard deviation was considered significant and suggested as a mini-impactor deployment.

2.4 Experimental Design

2.4.1 Mini-impactor Design

Prior to mini-impactor fabrication, physical attributes of the mini-impactor were first approximated, namely cantilever beam stiffness, 2.12, and first natural frequency (in hertz), Equation 2.13.

$$k = \frac{3E_1 I}{L^3} \tag{2.12}$$

$$\omega_o = \frac{1.875^2}{2\pi L^2}\sqrt{\frac{E_1 I}{\rho A}} \tag{2.13}$$

The variables populating 2.12 and 2.13 are:

(i) E_1 - Longitudinal Young's Modulus

(ii) I – 2nd Moment of Area

(iii) ρ – Mini-impactor Density

(iv) A – Cross-sectional Area

(v) L – Beam Length

Mini-impactor Manufacturing

A mini-impactor, see Figure 2.1 is a proximally and distally shimmed composite beam and encastered to the structure being interrogated at the beam's proximal end. The beam material is a unidirectional T800/3900-2 prepreg all oriented along the longitudinal axis of the beam. Crucial MI beam designs is stiffness and in this case a range of 1000 – 3000 N/m were permissible.

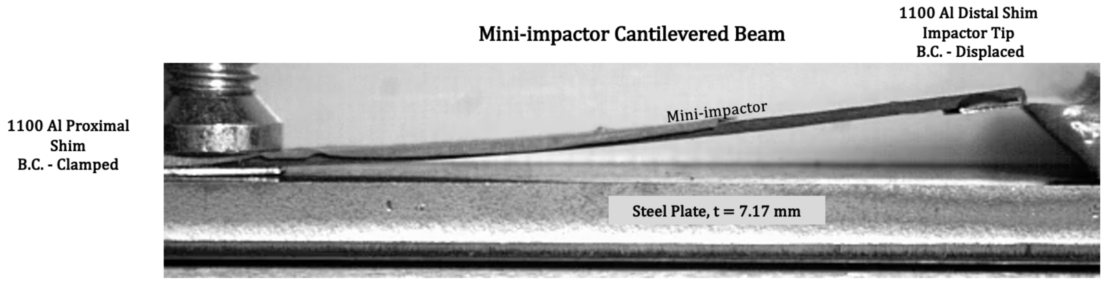

Figure 2.1: A representative mini-impactor. The mini-impactor is clamped to a steel plate and mini-impactor's tip is displaced normal to the plate to a height of 6.35mm.

With this in mind, three beam thicknesses were targeted and enforced via number of T800/3900-2 prepreg plies. These plates were debulked at a pressure of 1atm. Debulking occurs after the first ply and then after every four plies laid down.

After debulk, the stock plates are cured at an elevated temperature ($177^{o}C$) under 1atm of compaction pressure. The stock plates are cut to lengths 25.4mm longer than desired with an average width of 6.44mm. This 25.4mm extra length provides a sufficient beam section to be clamped at the time of experimentation. The remaining length of the mini-impactor beam is the length used in determination of the stiffness metric. The mini-impactor beam lengths varied from 38.1 to 89.1mm, as well as, the extra 25.4mm. The mass of the impactor beams ranged from 0.25 - 1.38g.

Aluminum 1100 (Brinell Hardness 23) shim stock of 0.5mm thickness elevated the T800/3900-2 beam above the waveguide surface. Shimming the Mini Impactors are crucial for exciting waveguide frequencies an order of magnitude greater than traditional impact hammers. The flat nature of the shims ensured at impact, the entire surface area of the impacting tip would strike uniformly and completely upon the waveguide. The proximal shim is on the clamped portion of the mini-impactor and is 25.4mm x 6.44mm while the distal shim is the impacting tip and is 6.44mm x 6.44mm. The average mass of impactor tip is 0.05g and a significant mass relative to beam mass. Without consideration of tip mass, the first natural frequency of the beams was stiffer than reality, resulting in first natural frequencies overestimated by $8-22\%$ relative to the finite element model determined natural frequency. Presented in **??** are the FEM natural frequencies instead of the hand calculations. Structural adhesive (Aeropoxy ES6228) bonded, under compaction, the T800/3900-2 beams to the 1100 aluminum shims and post-cured at $60^{o}C$ for 2h. At completion of this step, the mini-impactors are capable of being deployed for ultrasonic guided waves generation in a waveguide.

Table 2.1: Experimental Mini-impactor Design Parameters

Mini-impactor (M.I.) ID	**1**	**2**	**3**	**4**	**5**	**6**
Number of Plies per Beam	4	4	6	6	8	8
Cantilever Length, [mm]	38.4	44.5	57.2	69.9	76.2	88.9
Width [mm]	6.13	6.10	6.68	6.88	6.58	6.84
Thickness ,[mm]	0.74	0.73	1.17	1.18	1.58	1.50
Beam+Tip Mass, [g]	0.11	0.11	0.20	0.25	0.34	0.38
Stiffness, [N/m]	1682	999	2121	1227	2170	1216
Natural Frequency, [Hz]	642.1	476.6	494.3	338.5	390.4	277.1
Strain Energy, [mJ]	32.9	19.5	41.4	24.0	42.4	23.7

2.4.2 Waveguide Design

Waveguides are thin plates and often described as *plate guides*, for the sake of communication, waveguides will be maintained throughout the paper. The purpose of mini-impactors are to create ultrasonic guided waves within waveguide aerostructures. Framed by this, the waveguides selected for experimentation are selected with aerospace industry structural materials in mind. The aerospace structure materials selected have different levels of isotropy: a) Completely Isotropic and b) Orthotropic. Orthotropic materials have three planes of orthogonal symmetry resulting in nine elastic constants that dictate their mechanical behavior. The elastic constants are mathematically expressed, mostly, as combinations of the engineering properties descriptive of the lamina and an angle of orientation of the Warp-direction fibers. A laminate are a build-up of lamina that are bonded together. The orientation of all the lamina and their respective material properties directly influence the propagation of UGW. On the other hand, a completely isotropic material requires only three elastic constants. The planes of orthogonality are reduced completely.

Structural Materials

The structural materials selected for excitation by the mini-impactors are:

1. 6061-T6 Aluminum
2. Heat Treated Steel
3. Hexcel Plain-Woven Carbon Fiber 282 3K/ Kaneka GR6862 Epoxy (GFRP)
4. Fiberglast E-Glass 7781 8H/ Kaneka GR6862 Epoxy (CFRP)

Aluminum 6061-T6 is a precipitation hardened alloy class of aluminum for the purpose of enhancing yield strength and is a structural material common in wing and fuselage structures.

Steel Heat treated steel is a iron ore with elemental impurities, such as nitrogen and/or carbon. After purification of the iron ore, alloying elements can be added to create various alloys of steel (e.g. stainless steel). For this research, a low carbon steel was selected for its representative material properties as well as its price point. The heat treatment was favored for improving the steel's mechanical properties (e.g. hardness, ductility,...).

Carbon Fiber/Epoxy Plain carbon fiber from Hexcel (Type 282 3K) infused via Kaneka GR6862 Vacuum Assisted Resin Transfer Molding (VARTM) Epoxy was fabricated in-situ. All the warp tows were aligned with the longitudinal direction and therefore all fill tows were aligned in the transverse direction. Using the VARTM technique, the three carbon fiber impact plates are best manufactured as a single entity and trimmed to the plate specific width and length (300mm x 300mm). To achieve as nominal impact plate thicknesses as possible, 4, 6, and 22 plies were arranged within the vacuum bag and "stair-stepped" from thickest to thinnest plates. After a 24hr room temperature primary cure and a secondary cure at an elevated temperature, the resulting plates properties are provided in Table2.

Fiberglass/Epoxy Fiberglass 7781 8-Harness (8H) Weave is a drapeble fabric and is commonly used for tough geometries to fill. The 8-Harness Weave is when on tow of fibers goes over eight fiber tow bundles and under one, then back over eight. For example, the compound curvature about a nose cone is better fit with this fabric than a fabric with a plain weave (over one fiber tow bundle, under one fiber tow bundle).

Plate Thicknesses Furthermore, three waveguide thicknesses have been targeted and within scope of aerospace structural wall thicknesses. The targeted waveguide thicknesses are 0.8mm, 1.5mm, and 6.35mm. The waveguides were ordered or manufactured and trimmed to dimensions of 300mm x 300mm and of this dimensionality to mitigate ultrasonic guided wave reflections and interferences observed at the sensing location. Therefore, twelve waveguides of four different aerostructure materials and three thicknesses per material, are NDE by the Mini Impactor.

Table 2.2: Plates excited by mini-impactors.
[a]Three plate thicknesses per material.
[b]Transverse Anisotropic Wave Speeds Calculated at 150 kHz

Material	6061-T6 Aluminum	Heat Treated Steel	Fiberglass/ Epoxy (GFRP)	Carbon Fiber/ Epoxy (CFRP)
Ply Angles [^{o}]	Isotropic	Isotropic	0_10	0_10
Thickness[a] [mm]	0.86 1.65 6.67	0.76 1.48 7.17	0.99 1.45 5.46	0.99 1.39 4.86
Extensional Modulus [GPa]	68.9	200	29.7	58
Density [$\frac{kg}{m^3}$]	2700	7800	1970	1380
Extensional Velocity [$\frac{m}{s}$]	6139	5851	4968	6490
Flexural Velocity[b] [$\frac{m}{s}$]	3095	3205	459 562 1124	497 607 1166

2.4.3 Mini-impactor Switch Circuit

A simple switch circuit probing for voltage potential change was implemented to trigger an oscilloscope reliably and consistently at the moment of mini-imapctor's impact upon the plate.

It is critical to the UGW measurements that every impact occur at the same starting time, that is $t_o = 0s$. This avoids unnecessary and time consuming temporal signal alignment. To avoid this cumbersome time alignment, a switch circuit was integrated into the mini-impactor and plate system. For every experiment permutation, the mini-impactor *is* the switch. The mini-impactors had a copper conducting tape adhered to the aluminum tip and connected to the voltage supply. The plate is also energized by the voltage supply and all are connected to a common ground. An oscilloscope (Picoscope 4824) probes for the step change in voltage from ground, $V = 0$, to the power supply voltage, $V_s = 5V$ and triggers when the voltage sensed meets a threshold of $1V$. Figure 2.2 is an electrical schematic of the circuit.

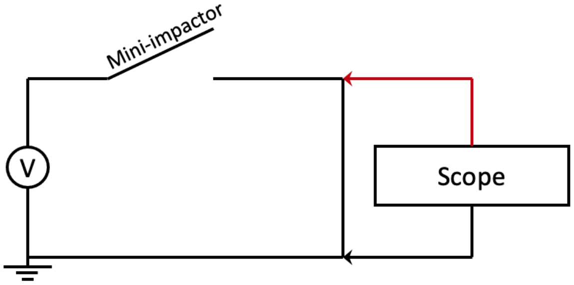

Figure 2.2: Simple switch circuit schematic

The metallic waveguides were simple in assumption that they themselves were part of the circuit and grounded accordingly. The anisotropic waveguides were more complicated, but they too were modified with a thin conducting copper layer completing the backend of the circuit. The circuit is “closed” when the mini-impactor contacts the waveguide. At this intance a driven current propagates across the oscilloscope probes, which via Ohms Law $V = IR$, is recognized as a voltage step because the oscilloscope with a built-in resistance. The oscilliscope senses a voltage potential develop across the positive and ground probes and the Picoscope 4824 records the experiment’s vibrations at the receiver.

2.4.4 Data Collection Methodology

The data acquisition system is prepared by connecting the mini-impactor switch circuit to the DC voltage supply. The positive lead is connected to the plate’s conducting pathway. The DC power supply negative lead is then connected to common ground. Likewise, the negative probe from the oscilloscope is connected to common ground. The positive probe from the oscilloscope is connected to the conducting pathway on the mini-impactor. The proximal end of the mini-impactor is clamped to the plate and the distal end of the mini-impactor is displaced out-of-plane by 6.35mm, resulting in a cantilever formation and storing strain energy within the beam. Additionally, this causes the simple witch circuit to be in the “open” state. At this step, the oscilloscope’s trigger is primed and waiting for the mini-impactor switch circuit to be “closed,” see Figure2.3.

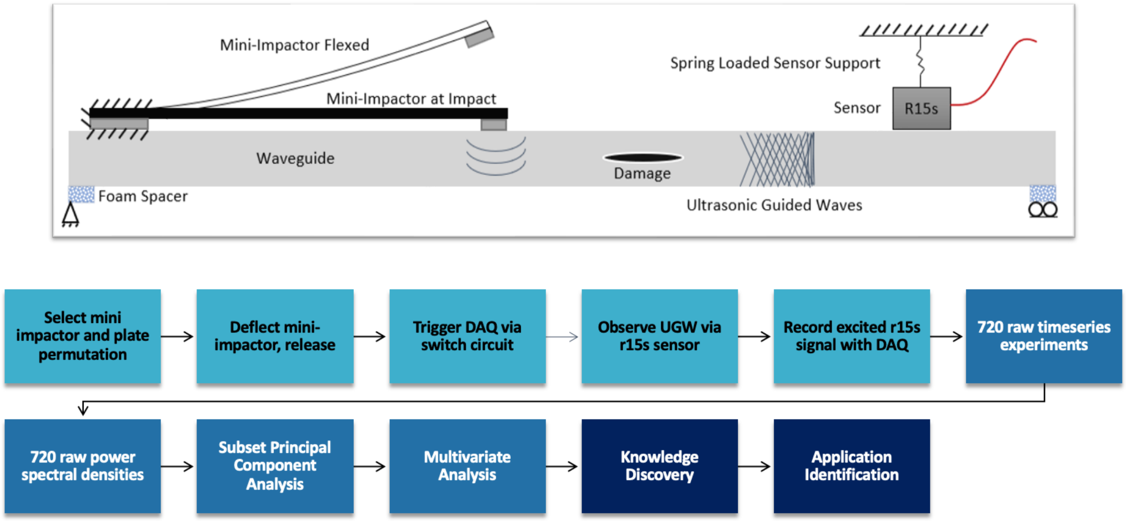

Figure 2.3: The experimental process. The color coding is as follows: Light Blue refers to a single experiment. Blue refers to the dataset analysis, while the dark blue indicates the translation of results to applicability

The distal tip shim (displacing mechanism) is removed, and the beam undergoes a transfer of energy. The stored strain energy in the beam is converted to kinetic energy due to the mini-impactors desire to come to stable rest, which is an unflexed position . Hypothetically, if the mini-impactor were allowed to oscillate after the initial displacement was removed, the beam would undergo a damped oscillation. The mini-impactor exploits this free-vibration behavior, but instead of allowing the free-vibration to propagate, the impacted plates are introduced at the zero displacement location, forcing the mini-impactor to undergo an impact event. At this moment of contact, the oscilloscope is triggered and recording the experiment. Simultaneously, the impact event generates stress waves. At a distance from impact, these stress waves coalesce into ultrasonic guided waves. The ultrasonic guided waves propagate through the plate and excite the gel coupled R15s AE sensor which is at a distance of

101.6mm from the mini-impactor excitation location. The R15s AE sensor is in direct alignment with the pointing-direction of the mini-impactor. The R15s AE receiver is under a minor but constant downward force to ensure consistent coupling with the impact plate via the gel couplant. Crucial to mitigation of test frame influences, the impact plates are supported in each corner with a porous, compliant foam. The impedance mismatch between the impact plates and foam is sufficient in preventing transmission of UGW into the test frame. The remainder of the boundary is under a free-free boundary condition and interacting with air at standard temperature and pressure.

Maintaining the temporal representation of the data, the Symmetric (S_0) and Anti-symmetric (A_0) dispersive modes can be observed, Figure 2.4. Every time series signal was metered at 80MS/s and collected over a period of 200μs. A sample period of 12.5ns resulted and a total of 16004 samples defining the waveguide's time series response to the mini-impactor excitation.

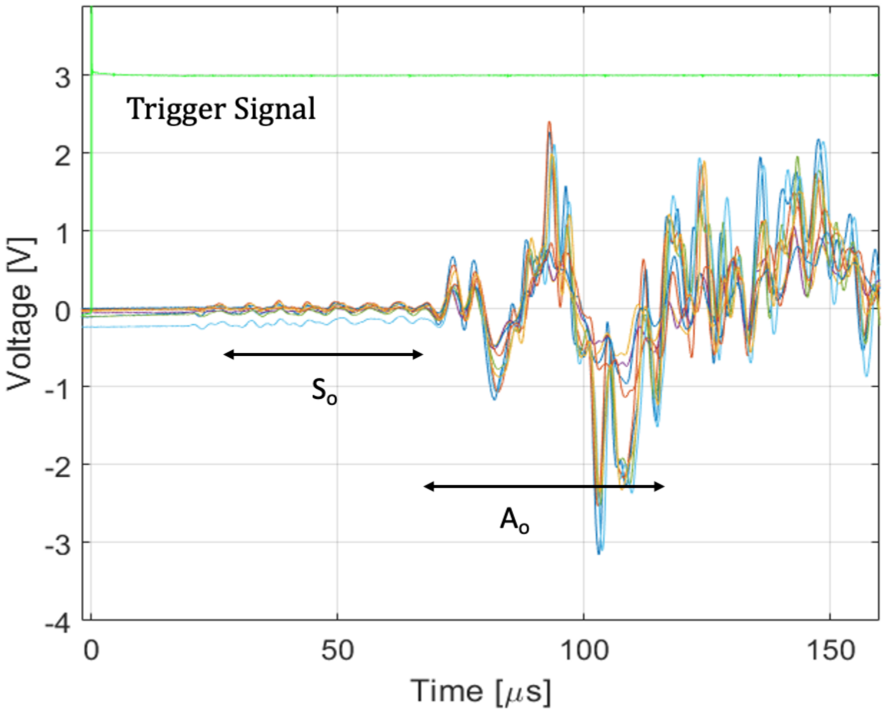

Figure 2.4: An example of 10 repeated experiments for a single permutation. Note the green trigger signal, it is actually 10 signals.

This time series observation is repeated a total of 10 times for each experimental permutation. All are thus time aligned by mini-impactor switch step function-like signal, and stored for analysis. This prior mentioned process is repeated for all 72 experimental permutations, resulting in 720 recorded time series experiments.

The researcher is the first line of defense against poor experimentation and rejects or accepts an experiment. Each time series signal is centered about 0V (mean detrending). This removes any linear trends that might artificially affect the casting of the time series signal into the frequency domain, which is for the second analysis procedure soon to be discussed.

2.4.5 Data Analysis Methodology

The data analysis involves two independent analysis flows. The goal of having a strong, data-driven, inference regarding permutations of experiments that are significant for deployment in the aerospace NDE industry was the motivation. The first being a spectral analysis coupled with Principal Component Analysis sorted with Hotelling's T^2 statistical metric. The second data analysis work flow is strictly in the time domain and involves pre-processing the data to identify and isolate the anti-symmetric (A_0) wave packet. The baseline (average experiment for that perspective) was removed and a detection scheme using wave packet energies was used, along with mean and standard deviation to identify the relevant experiments and permutations

Method 1 - Temporal Analysis Methodology

The baseline average signal is removed from each experiment resulting in a residual curve. The energy within the both the baseline and residual signals are calculated. The Normalized Residual Energy ratio is taken along with the statistical properties of the group of data. The NRE greater than the first standard deviation was the metric at identifying the significant experiments and permutations. Coupling the two data analyses together is the concept of signal energy. The spectral technique utilizes the variances as a form of signal energy and the time domain technique utilizes the wave packet energy.

Method 2 - Spectral Analysis

Fourier Transform and the Welch Approach Every experiment was recorded in the time domain with an R15s AE receiver sampling at 80MHz, implying the the Nyquist frequency being 40 MHz. Sufficient sampling occurred to avoid any possibility of aliasing. The time series signals were pre-processed to remove any trends. The time series signals were then cast into the frequency domain and expressed as a Power Spectral Density (PSD) via the Welch method. Six Hanning windows with a 66% overlap was utilized. The PSDs were then organized into four matrices organized by plate material. This was done to avoid biasing the dataset towards the isotropic materials which have similar wave speeds.

The now four material specific matrice's PSDs were organized into a format congruent with PCA analysis and decomposed into their respective most prominent components. Hotelling's T^2 metric was applied to each matrice's PCs and the top 10% experiments from each data matrices are extracted and related back to the experimental permutation.

2.5 Results

2.5.1 Method 1 - Temporal Analysis

The time series data analysis method produced gated and windowed time histories, baseline and residual signals, NRE ratios, and their respective statistics. The results presented are the perspectives ranging from universal to thickness to material specific.

Universal Perspective

The Universal perspective involved comparing all timeseries experiment to the baseline average of all the experiments performed. It is looking at the entire dataset and determining one or more MI that could be significant from the NRE metric. Indicated as significant permutations are those experiments that

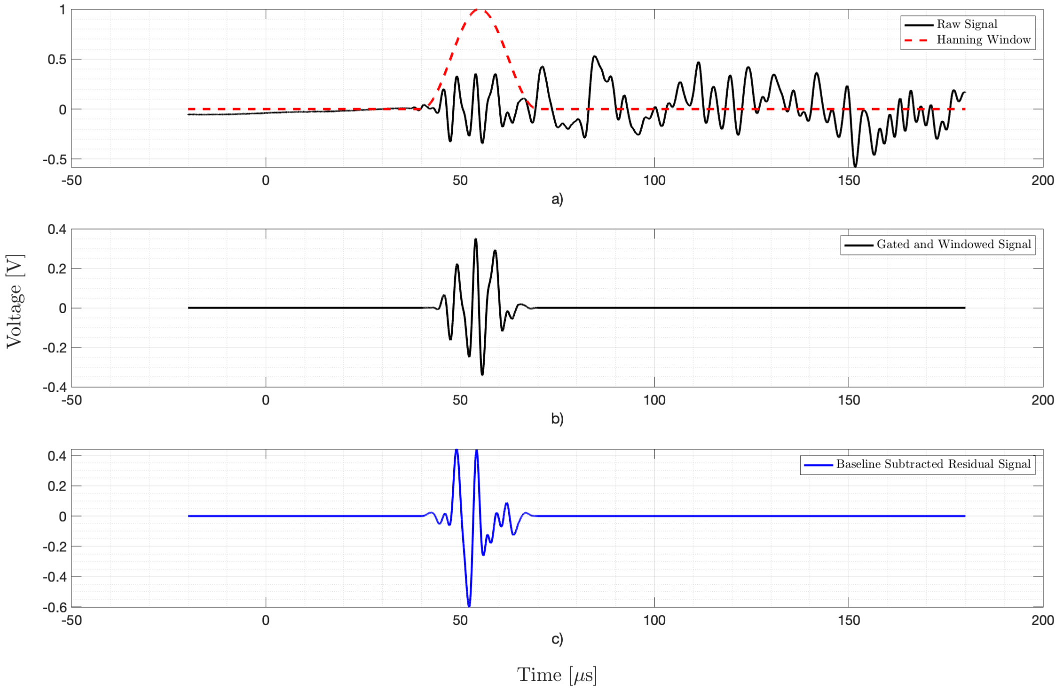

Figure 2.5: a) From the universal perspective, a raw signal with the Hanning window overlaid. b) Hanning windowed raw signal. c) A residual signal which is the windowed raw signal with the windowed baseline removed.

The mean NRE but especially the 1^{st} standard deviation, has parsed the significant from the insignificant permutations. In this case the 6plyx57mm MI (ID 5) is the indicated as the most universal. Also indicated is MI # 1.

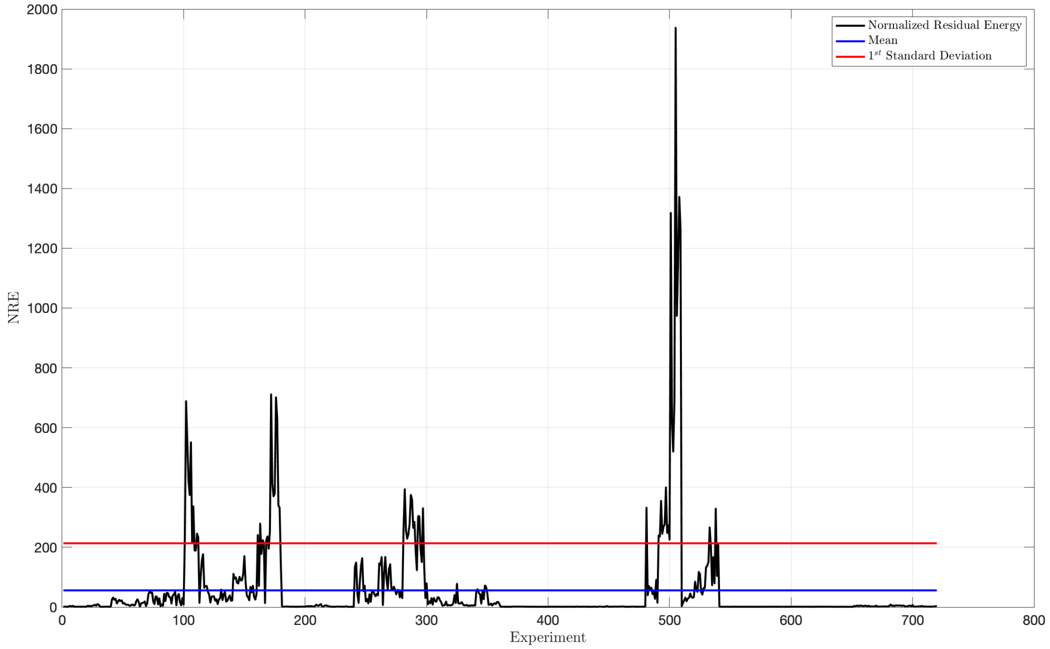

Figure 2.6: Normalized Residual Energy for the Universality perspective with the mean and standard deviation shown. Any experiment greater than the 1st standard deviation was considered significant. From left to right, the signficant MIs # 1, 2, 3, and 5. MI# 8 is also indicated.

Plate Material-Thickness Perspective

The plate material perspective involved comparing every time series experiment within that thickness category to the baseline average of all the experiment, Figure 2.7 for that material category.

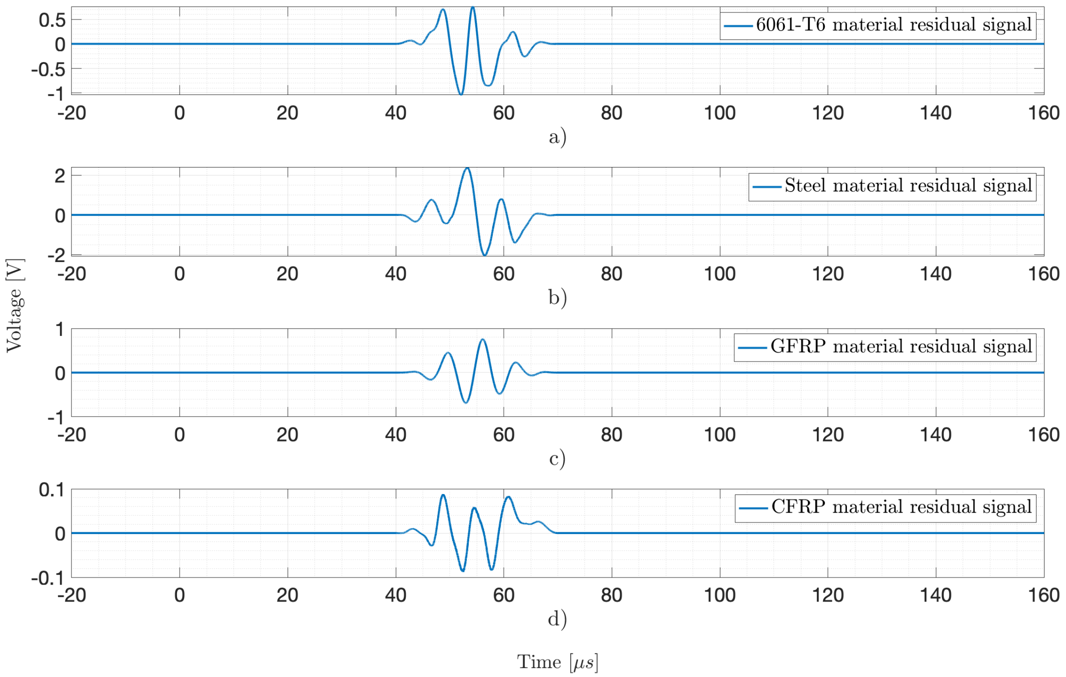

Figure 2.7: The four graphs are the NRE for each of the plate material types

The NRE for the four respective plate material are show in Figure 2.8 along with the NRE mean and 1^{st} standard deviation. Any NRE greater than the 1^{st} standard deviation is considered significant. The figure indicates that each material type has significant impactors that could be suggested as a deployable permutation. Figure 2.8 also shows that each material is excited by the upper half of the MI's 4-6, while with little influence from MI's 1-3.

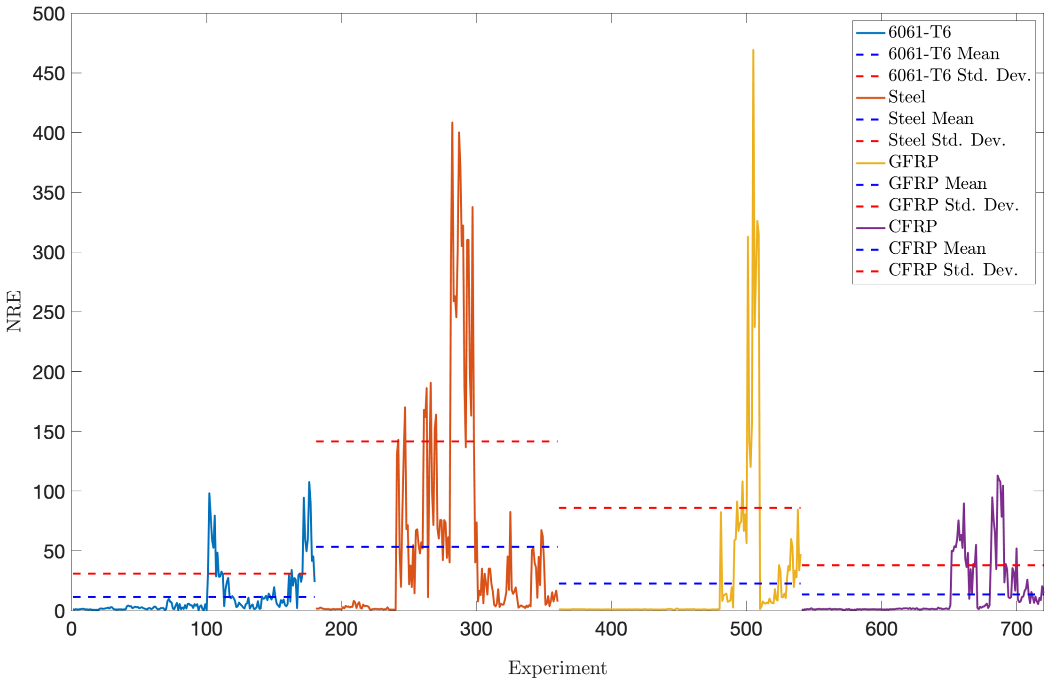

Figure 2.8: Normalized Residual Energy for the Plate Material perspective with the mean and standard deviation shown. From left to right are: 6061-T6, Steel, GFRP, and CFRP.

2.5.2 Method 2 - Spectral Analysis

The spectral data analysis method produced power spectral density plots, eigenvalues (i.e. variance) and Principal Components determined from the PCA, and Hotelling's T^2 metric used for ranking permutations. The results are presented from perspective of the plate materials, which is congruent with minimizing potential global biases (i.e. aluminum and steel results being weighted together due to similar bulk wavespeeds). The analysis presents the local perspective followed by the global perspective.

The way the data is presented for the four materials is separately and organized by thickness and MI ID. The rows are all MIs at for the same thickness, while the columns represent individual mini-impactors. The Welch Power Spectrum plot's axis is in a semilogy format to capture the 99% confidence range (uncertainty) as a single vertical bar (red) (Mack, 2015) and (Bendat & Piersol, 2011).

Aluminum Plates

The aluminum plates and mini-impactors Power Spectrum on the whole seem consistent. Digging deeper will prove otherwise. For instance, Figure 2.9's upperleft most Power Spectrum, MI #1 and 0.8mm thick, has two steps of excited frequency content, which ends at 1MHz. Another noticeable feature is found for the 1.65mm thick plate, all mini-impactors generated a peak power spectrum greater than 1.

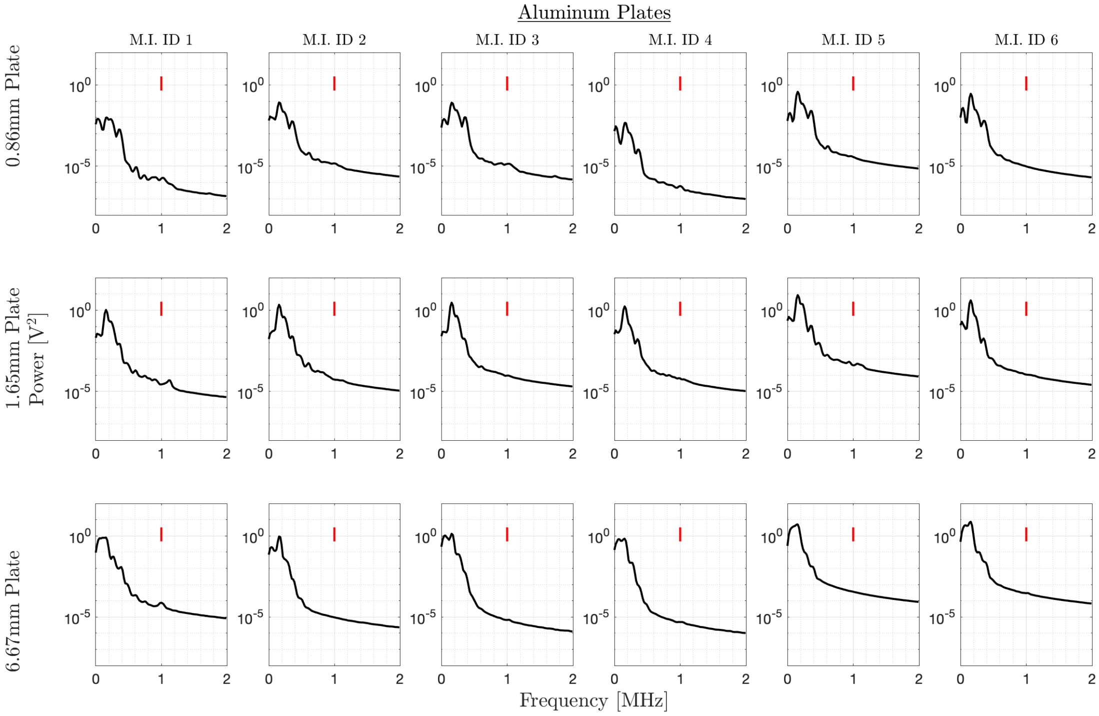

Figure 2.9: Welch power spectra of all eighteen aluminum plate - mini-impactor permutations with a spectral confidence range of 99%

Steel Plates

The steel responded strongly to MI #1, Figure 2.10 (leftmost column). MI #1 excited the plates well into the 1-2MHz range. The caveat being this is very low energy relative to the max spectral peak of 1. Mini-impactor #5 also excited the two thicker plates similar to MI #1, but not nearly as broadband but with the max peak of all steel power spectra.

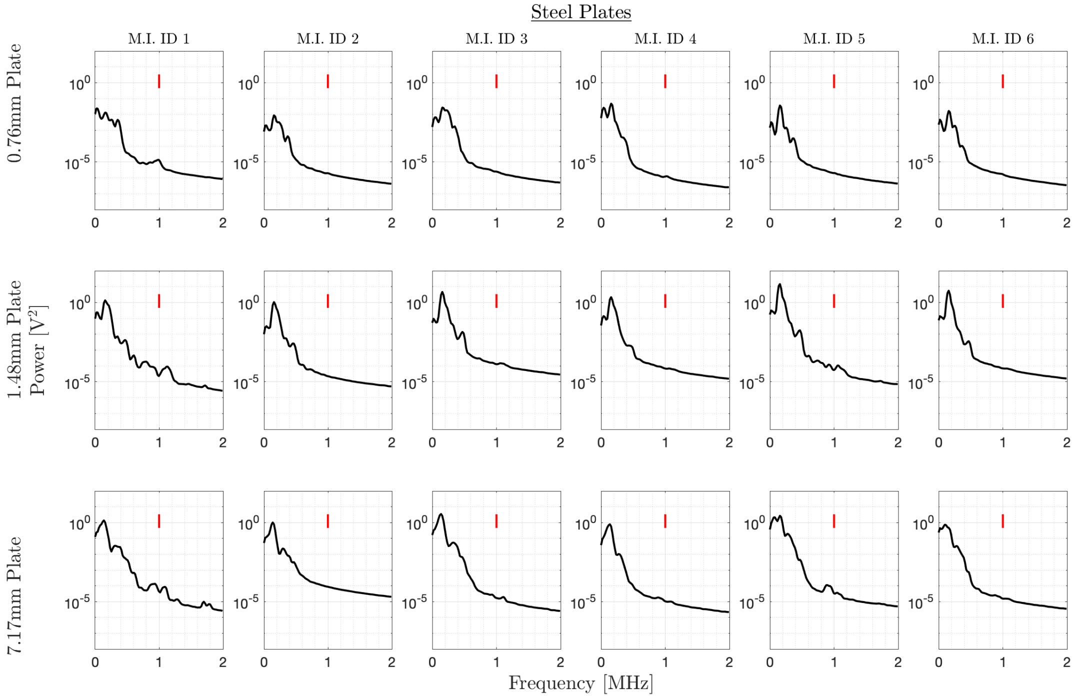

Figure 2.10: Welch power spectra of all eighteen steel plate - mini-impactor permutations with a spectral confidence range of 99%

GFRP Plates

A noticeable change occurred in the power spectra when switching to the orthotropic plates, the spectra for all GFRP permutations never generated frequency content greater than 1MHz. The higher frequency excitation is being attenuated by the GFRP orthotropy.

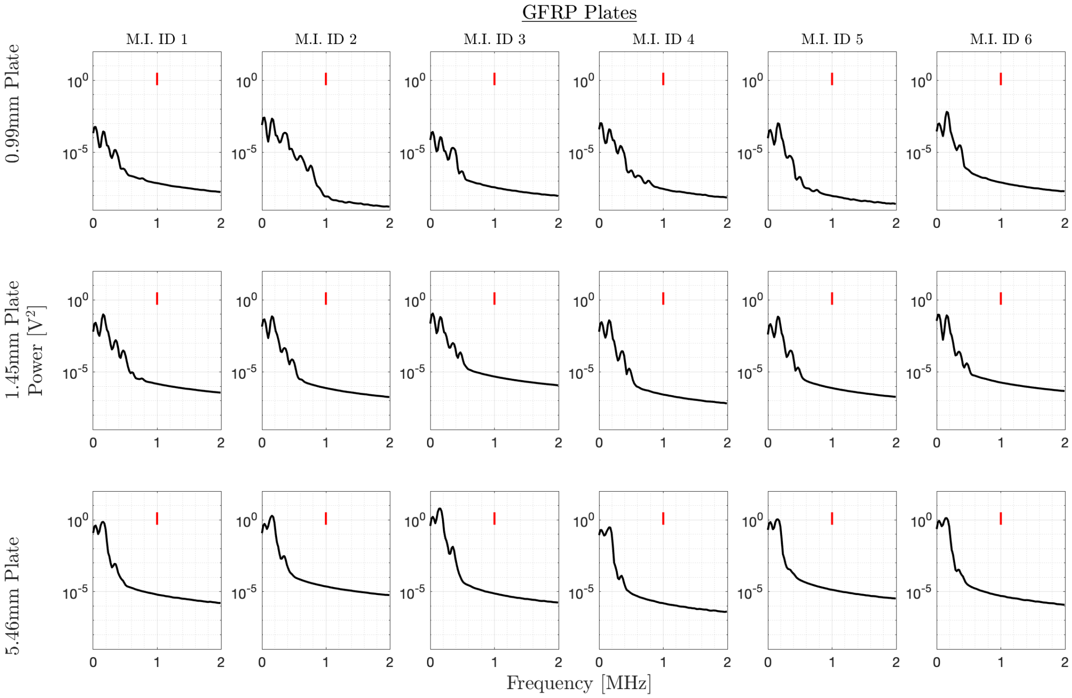

Figure 2.11: Welch power spectra of all eighteen GFRP plate - mini-impactor permutations with a spectral confidence range of 99%

CFRP Plates

The CFRP plates are more responsive to some of the mini impactors. However, MI#1 has consistently excited most the plates. That includes these except the 4.8mm plate, it has less features than the other two thicknesses.

The power spectrum with mini-impactor #8 and 0.9mm plate thickness, is also exhibiting the two-step behavior that is exhibited in the Aluminum MI#1 and 0.86mm thick plate.

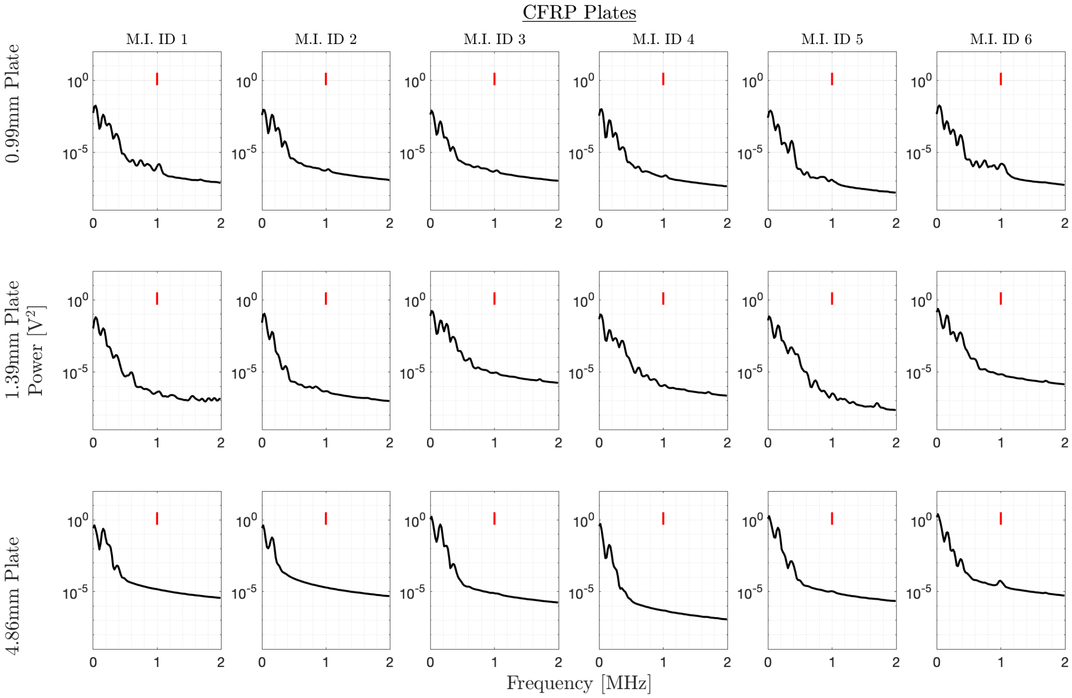

Figure 2.12: Welch power spectra of all eighteen CFRP plate - mini-impactor permutations with a spectral confidence range of 99%

Power Spectra Conclusions The mini-impactors fabricated served one purpose, generating noticeable UGW. All of the MI have generated frequency content well beyond that of a traditional modal hammer. So with disregard to everything, one could excite a structure reasonably into the hundreds of kHz. This isnt desirous though becuase observing the different material power spectra, there ARE some difference that need to be addressed.it is best to use a statistical metric to determine significant permutations.

Principal Component Analysis

Presented are the material specific Principal Components(PC) that contribute to 95% of the energy within each dataset. Performing PCA naturally sorted significant energy contributions from each spectral feature. Figure 2.13 are Pareto plots for each material. The bars are representative of PC that that contribute to the 95% threshold. Additionally, the cumulative energy growth is shown.

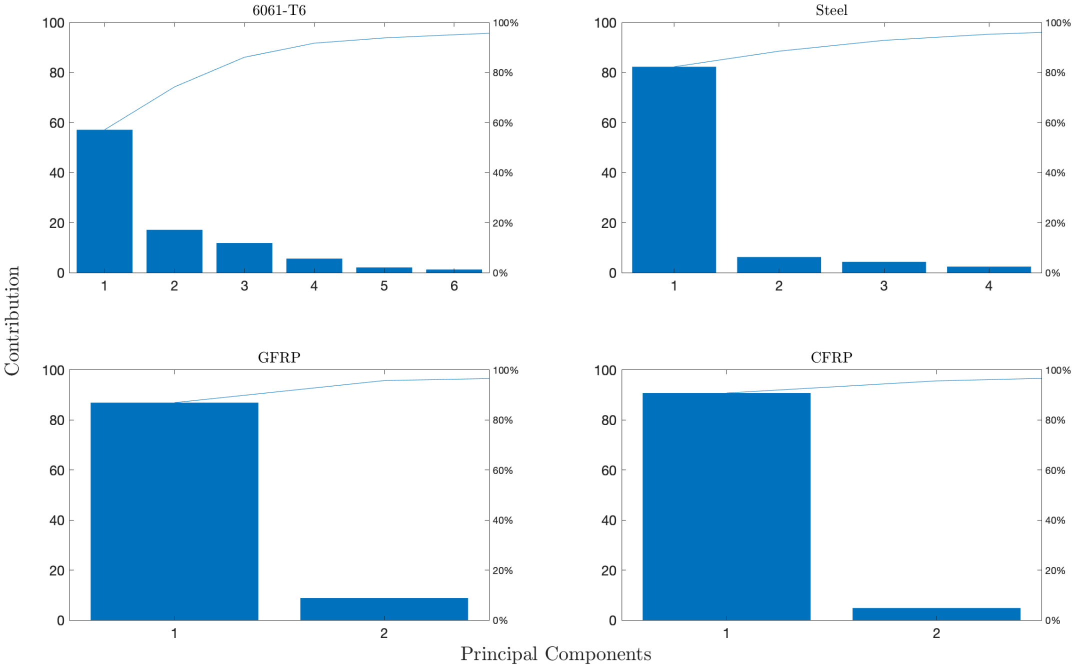

Figure 2.13: Pareto plots of the PC that cumulatively contribute to a 95% threshold.

The isotropic materials, aluminum and steel, require more PC, 6 and 4 respectively, to describe their dominant pattern behavior. The anisotropics only require two PC each to describe their dominant patterns up to 95% energy level.

It is interesting to graphically see what a Principal Component is. Figure has the 6061 top 6 PCs along with the original spectra and weighted reconstruction of the original spectra.

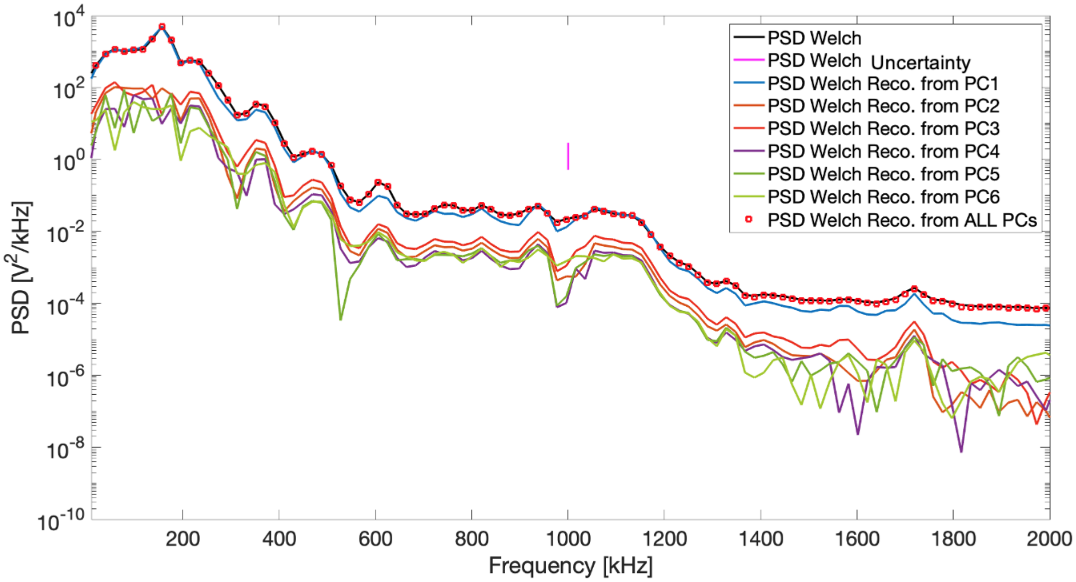

Figure 2.14: Principal Components 1-6 are orthogonal (independent), weighted, representations of the spectra (think mode shapes for structures). Reconstructing the original spectra is the linear combination of the weighted PC's.

Hotelling's T^{2} Metric

Performing the PCA analysis, the Hotelling T^{2} statistics are calculated to statistically sort insignificant from significant experiment permutations. The metric's null hypothesis is the mean of the dataset. Any permutation near the mean is less significant, while more distant from the dataset mean is significant. The T^2 metric is measures the multivariate distance of each observation from the mean of the dataset (Krzanowski & Krzanowski, 2000).

Figure **??** graphically represents the T^2 metric sorted by significance. All experiments that are less than the cut-off of 18, are considered significant and the rest discarded. The significant experiments have an uniquely identifying number than relates it to the permutation number. These permutations were then mined for information that would allocate them to a specific deployment, whether universal or local.

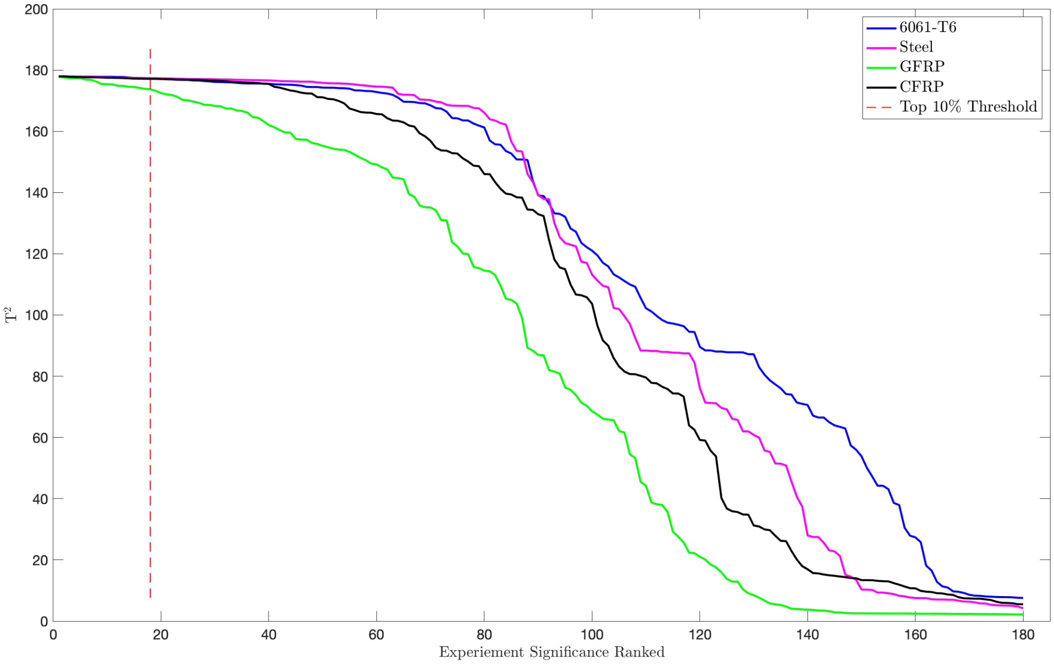

Figure 2.15: Hotelling's T^2 statistic plotted with top 10% threshold applied to identify the significant experiments.

2.6 Conclusions

2.6.1 General Observations

The results generally indicate that across the experimental domain and significance not accounted for yet, the mini-impactors are capable of exciting frequencies greater than 10x that of traditional impact/modal hammer devices. Immediately, this indicates that the conceptual design of a mini-impactor is reasonable for exciting aerospace structures beyond traditional capabilities.

2.6.2 Honed Purpose

The purpose of this research is to identify statistically significant experiment permutations for the deployment of mini-impactors as an excitation source for structural interrogations. To maximize the possibility of energetically exciting the plate frequencies within the range of potential damages, especially w.r.t. to composites, energy metrics were evaluated to identify the best permutations. It is best to observe the statistically significant permutations, first, from the plate material and thickness perspective (local) then the universal perspective (global).

2.6.3 Plate Material and Thickness Perspective

From the two independent and domain-different analyses, along with a common guiding theme of *following the energy*, the experimental permutation deployments are identified, see Figure 2.3. The deployments identified in each analysis are in remarkable agreement with each other (75%).

Table 2.3: Suggested deployments of the mini-impactor for plate material and thickness combinations.
^{a} The time series analysis indicated two mini-impactors to deploy.

Plate Material	**Plate Thickness [mm]**	**Time Series Analysis M.I. ID** ^{a}	**Frequency Analysis M.I. ID**	**Frequency Range [kHz]**
6061-T6	0.86	5, 1	1	[0 800]
	1.65	5	5	[0 600]
	6.67	6	6	[0 550]
Steel	0 .76	2	1	[0 550]
	1.48	6, 5	5	[0 600]
	7.17	3	3	[0 700]
GFRP	0 .99	1	1	[0 500]
	1.45	3	3	[0 600]
	5.46	3	3	[0 600]
CFRP	0.99	1	1	[0 900]
	1.39	6	6	[0 700]
	4.86	3, 1	3	[0 600]

2.6.4 Universal Perspective

The universal perspective has yielded to the M.I. 1, the 4ply x 38mm mini impactor (ID#1). This impactor did not generate the most energy for each permutation it was involved in but did reoccur in the analyses as a significant propagator of energy packets. Investigating the power spectra this impactor generated interesting frequency content for most of the plate-thickness permutations.

The reasons underlying the discordance (6061-T6 x 0.86mm, Steel x .076mm, and Steel x 1.48mm) between the two methods and their suggested permutations are not well understood at this time. The discordance occurs in the isotropic plates and care

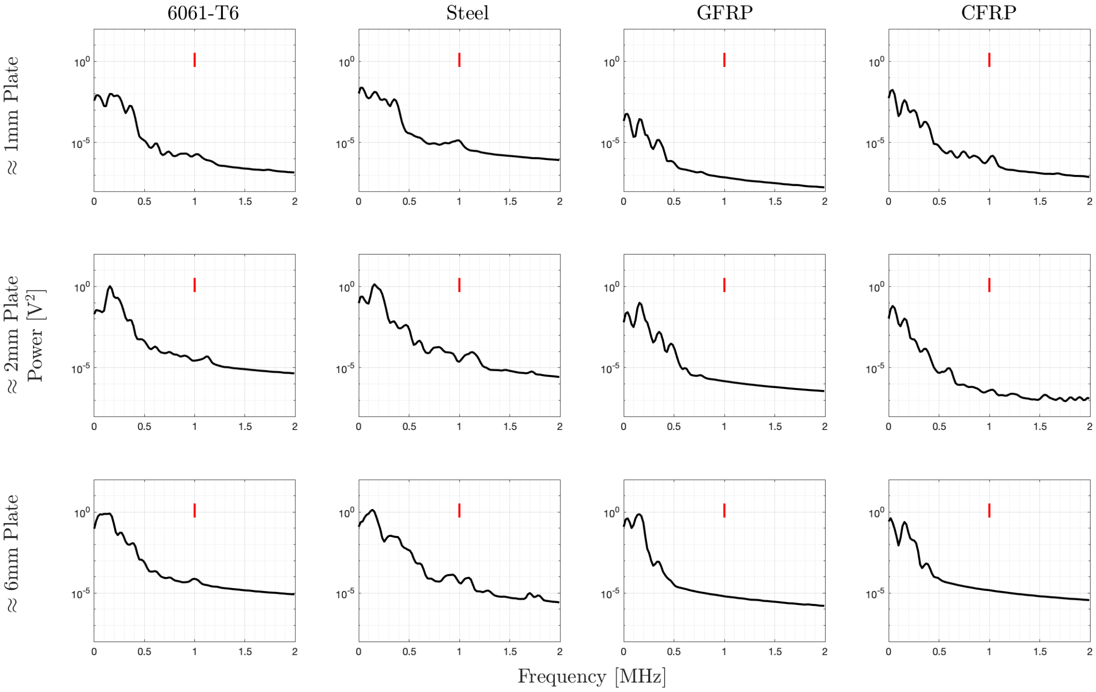

Figure 2.16: M.I. 1's influence on power spectra for all plate-thickness permutations.

was taken to eliminate inherent bias (similar bulk wave speeds) by separating in both data analysis methodologies the signals by material type before analysis.

Mining the datasets using the two independent data analysis approaches identified the statistically significant experimental permutations. Remarkably, 75% of the suggested deployments are in agreement between the two independent data analysis methods.

Chapter 3

WAVSVD Phase Velocity Algorithm

3.1 Abstract

A novel signal analysis method, WAVSVD, is presented. This signal analysis algorithm reveals more frequency-wavenumber bandwidth of Lamb modes and enhances the estimate of phase velocities of guided waves traveling in plates and plate-like structures from data collected during experimentation. Estimation of propagating Lamb wave velocities via their experimentally observed wave dispersions is non-trivial. WAVSVD exploits the mathematical attributes of Singular Value Decomposition (SVD) natural ability to decompose a spatiotemporal dataset into a data-driven, set of tailored basis (Brunton & Kutz, 2022). In this case the spatiotemporal data are decomposed into two spatial and temporal unitary matrices, as well as a third

scaling matrix. The two respective unitary matrices encode the spatial and temporal patterns within the dataset. The unitary matrices are then used to calculate a cross-covariance matrix. The cross-covariance matrix is then decomposed a second time and rank-reduced to denoise the dataset. After the cleansing mathematical operations, a reconstruction of the original dataset is performed. The reconstruction is cast to the power spectral domain with Lamb modes being identified and used for phase velocity estimation.

To achieve the required datasets, experimentation consisted of collecting broadband acoustic signals emanating from a plate commensurate with leaky Lamb waves. The two plates tested are aluminum and carbon fiber, they are representative of aerospace structure material and in the aluminum's case, a ground truth. The ultrasonic guided waves are generated using a broadband excitation source. The measured ultrasonic guided waves are recorded by a pair of broadband air-coupled transducers (MicroAcoustics BAT-1). The broadband excitation and sensing ensure all frequencies between 20kHz and 3MHz, are potentially generated and collected. The MI-Sensor Pair combo are for all intents and purposes, a pitch/catch nondestructive scan. The sensor pair is rastered away from the excitation source at increments of 1mm and temporal sampling occurred every 12.5ns. These sampling schemes essentially observes for all wavelengths up to 500m and frequencies up to 40MHz. The data collection process is ushered using an oscilloscope (4000 Series Picoscope) which is triggered consistently at impact with a switch circuit leaving no doubt about time-of-flight information. The data is preprocessed and passed to the WAVSVD algorithm. Results for both isotropic and specially-orthotropic plates in the wavenumber-frequency domain as well as the associated phase velocities are provided relative to a traditional estimation scheme as well as an analytic solution. The results are in good agreement with the analytic solution and significantly expand the identifiable bandwidth in the wavenumber-frequency domain.

3.2 Introduction

The novelty of the approach lies in the signal processing. The approach termed WAVSVD is described in totality. The Introduction has a strong commentary on what SVD is along with intermediary examples of the mathematical process operating within the algorithm and how they motivated the signal processing scheme.

Briefly, the dataset was preprocessed and consisted of the gating and windowing. In this case a boxcar window is used, and the preserved signal was normalized to capture the arrival of the A_0 and (potential S_0) wave modes. After windowing and normalization, the preprocessed data is decomposed using the powerful linear algebra tool, SVD. Traditionally researchers and mathematicians will select a decomposition rank threshold that corresponds to the amount of energy of each singular values contribution to the cumulative sum of energy within the dataset. The researchers and mathematicians then reconstruct the dataset from a reduced rank that is commensurate with the energy threshold, this is often seen in image compression. The novel nature of this proposed signal process ignores this reconstruction and operates on the decomposed dataset.

The outer product of the rank-reduced unitary matrices, which respectively encode an estimate of the temporal and spatial patterns is performed. This step exploits an interesting opportunity to correlate the tailored basis patterns in space and time without influence by the scaling singular values. This outer-product produces a spatiotemporal cross-covariance matrix unrestricted by the singular values which could prohibit mode feature(s) identification and is exact to this dataset.The spatiotemporal cross-covariance matrix is passed through the SVD a second time and rank-reduced via a second threshold to denoise the data prior to dataset reconstruction. It is important to note that prior to the second SVD, the outer product preserves the original dimension of the data as the inner matrix dimensions are the selected rank while the outer dimensions are the original dataset size. After the reconstruction, the 2D power spectrum is calculated from the 2D Fast Fourier Transform (FFT). The wavenumbers and frequencies corresponding to the Lamb mode(s) are extracted and used to estimate all corresponding phase velocities.

This technique's advantages become apparent when inspecting the wavenumber-frequency plot. It is clear bandwidth in both low and high frequency directions are extended relative to a traditional approach. The traditional approach is direct calculation of wavenumber-frequency from the preprocessed dataset. WAVSVD significantly enhances the dispersive A_0 mode. S_0 not present due to singal-to-noise. The S_0 mode was not large in amplituderelative to the noise in the timeseries experiment. The timeseries is dominated by A_0 mode and is typically present on the 2D power spectral estimate. The power spectrum is selected because amplitudes associated with modes of interest are further amplified and the noise features remaining are further reduced (small number squared produce smaller numbers, converse for large numbers). The experimental phase velocity calculations for 2024-T3 aluminum and Carbon Fiber Hexcel 282 Plain 3k/Epoxy (CFRP) plate are compared to analytical solutions from an open-source software program, DispersionCalculator (DC). The DC software is validated with Disperse, which is not open-source but considered a standard for calculating dispersion relations. Results indicate that the experimental phase velocities for both isotropic and orthotropic materials are valid when compared against their analytic solutions.

3.3 Math

A flowchart is presented to help organizethe math and the resulting subsectionstions. This is meant to walk from cell to cell in the methodology explaining the math process.

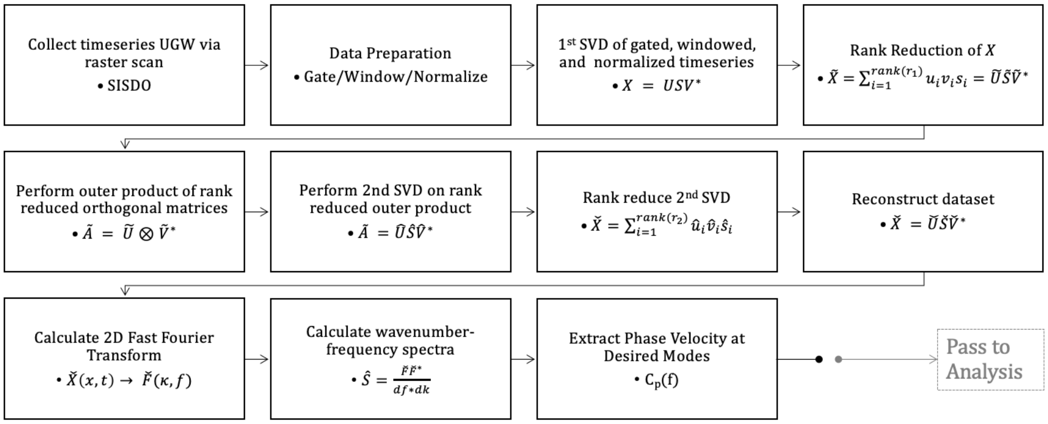

Figure 3.1: The core WAVSVD algorithm with pertinent equations

3.3.1 Single Input, Sliding Dual Output SISDO

Experimental design has been methodically performed to reduce specimen variability, minimizing doubt through spatial and temporal measurement resolution with reasonable. The sensors spatial resolution is controlled via Linear Stage Translator (LST) and digital calipers measuring relative spatial displacement from the origin(s) of the sensor pair. Three main experimental parameters were considered when preparing to execute SISDO: 1) waveguide material and geometry, 2) excitation source, and 3) data acquisition hardware.

Waveguides Two waveguide material are used, 1) Aluminum 2024-T3 and 2) CFRP laminate of Hexcel Plain 3K tow carbon fiber reinforced with SC 780 epoxy resin with layup angle orientations $[0/45/0/-45/0]_s$. The 2024-T3 Al plate geometry is 610mm x 304mm x 3.175mm and the CFRP plate dimensions are 889mm x 762mm x 2.2mm. Both plates were isolated from the support environment using a low-density acoustic reduction foam rendering the surfaces and boundaries in as traction-free as possible.

Excitation Source Exciting the plates are a broadband excitation impactor tool. In this case it is a Mini-impactor appropriate to the Aluminum plate that is approximately 6mm thick. see Chapter 2.6.4

Data Acquisition System On the receiving end, two broadband air-coupled transducers (BATs)(MicroAcoustics) with a bandwidth rang of [0 3] MHz. The BATs are a capacitiv-based sensor and are excellent at detecting the Lamb waves emanating from the plate as the UGW propagates. The BATs are lofted above the plate surfaces with a 0^o incident angle ensuring all possible Lamb modes between high to low velocities, within the A_0 and S_0 regime, are potentially observed. The two BATs are constantly spaced at 125mm. A high-pass filter with a cutoff frequency at the transition from acoustic to ultrasonic was used to selected to further eliminate any low frequency content. An oscilloscope (Picoscope 4842) was used to record the experimentation. The Nyquist frequency of the temporal sensing is 40MHz and the Nyquist wavenumber of spatial frequency is 500m. The data acquisition was initiated at impact. The impacting device, plate and adding a power supply creates a switch circuit which consistently triggers data acquisition at the moment of impact and intrinsically aligns all data in time.

The experiments consisted of keeping the location of excitation constant and the distance between the sensors constant, while incrementally rastering the sensors in 1mm increments, in-line, away from the excitation location. A digital caliper was integrated to the linear stage translator accurately measuring the incremental rastering. Using the dual outputs decreased the experiments required by half.

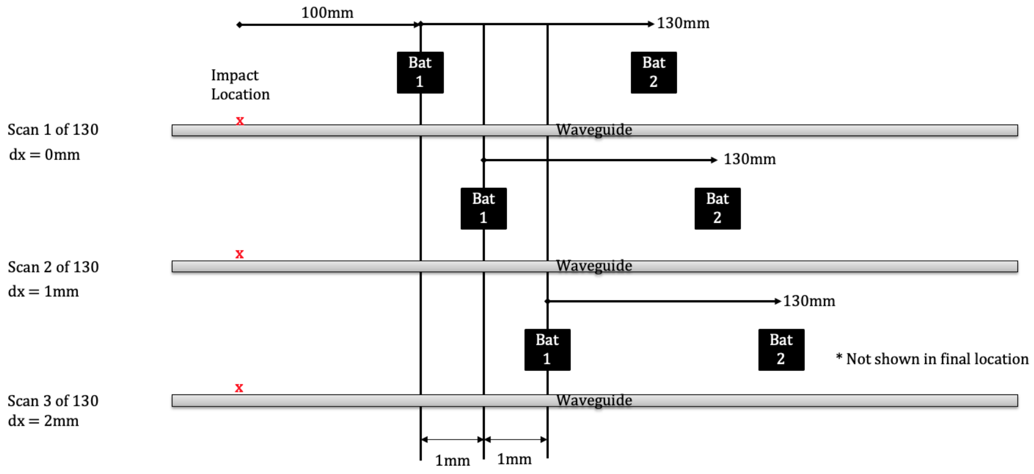

Figure 3.2: Experimental Setup for WAVSVD validation, SISDO

In totality, the experimental setup is a Single Input, Sliding Dual Output (SISDO) arrangement with broadband excitation and receiving that is adequately sampled in space and time ensuring that wavenumber-frequency estimation is conducted at fine enough resolutions to best estimate phase velocity.

3.3.2 Data Preparation

The raw data is modified assuming that the preparation process positively influences the analysis outcome. Though this is not a major source of concern for the analysis in general. The data is normalized to the max time amplitude for that experiment. Doing the windowing and normalizing of the data helps tell the bigger picture that exists for the dataset. An example of why this is important is that the global spatiotemporal amplitude behavior can change as a result of damage. The damage is located in space and so appears at an assumed damage location.

3.3.3 SVD 1 - Prepared Data

This proposed methodology deals with non-stationary, propagating Lamb waves bounded within plates. The goal of the method is to effectively extract wavenumbers and frequencies that are associated with dispersive modes descriptive of propagating stress waves. The data analysis procedure soon presented is operating on Boxcar windowed and normalized time series signals corresponding to S_0 and A_0 modes. These windowed and normalized signals are subjected to SVD resulting in two unitary matrices and an amplifier matrix. With consideration to the orientation of the experiments in the original matrix, the two unitary matrices will encode, respectively, the spatial and temporal patterns descriptive of the dataset. This is akin to 1.1.5 in the SVD Introduction Section above and clear example, from the full rank aluminum dataset, is presented in Figure 3.3.

3.3.4 Rank-Reduce SVD 1

This takes the prepared spatiotemporal dataset and decomposes the orthogonal space-time data into respective unitary matrices U and V, while S is a diagonal matrix of singular energy values that while amplify or decimate the spatial pattern contribution at that corresponding moment.

$$X = USV^* \tag{3.1}$$

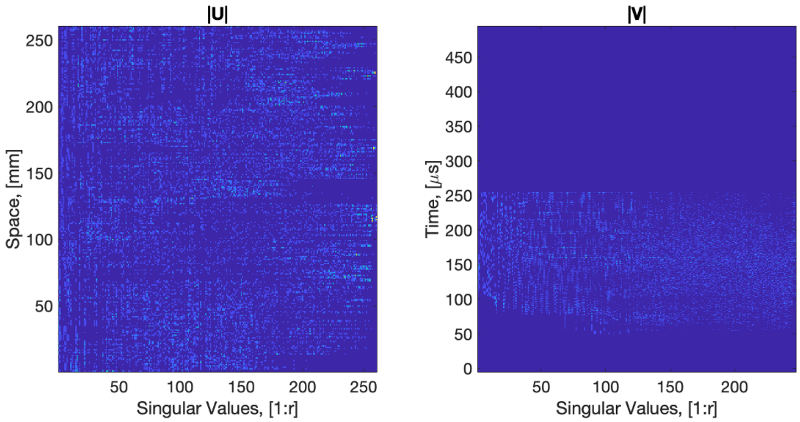

Figure 3.3: The two unitary matrices, U and V. Observing the U matrix, spatial patterns are apparent on the LHS of the graph. This is akin to similar to what might be seen in a wavelet decomposition scheme, though not an exact 1:1 translation

This step maintains 99% of the original data information but truncates the data and maintains space for the using guaranteed invertibility later, which is asserted in(Brunton & Kutz, 2022).

$$\tilde{X} = \sum_{i=1}^{rank, r_1} u_i v_i s_i = \tilde{U}\tilde{S}\tilde{V}^* \tag{3.2}$$

3.3.5 Ũ and Ṽ Outer-Product

The amplifier matrix, S, contains the singular values along the main diagonal indicating how much contribution each singular value mode is contributing to the entire dataset. A thresholding value is selected to preserve the data and used to construct a noise reduced version of the original dataset. This technique is valid, but a recognition has been made that not all the information is potentially being extracted, especially in the spirit of extracting all possible spatiotemporal information contained within dataset. The SVD of a spatiotemporal dataset generates a data specific basis that effectively represent space and time patterns. These are effectively an extraction process akin to a time/space transform to their frequency. Operating the outer product of unitary matrices allows for the calculation of the cross-covariance between space and time. This is a direct luxury of SVD and implies generalizable to multidimensional datasets. The cross covariance is decomposed via SVD, then reconstructed as reduced rank version of the dataset. The rational and proof this is an important analysis step in the broader context of effective mode identification and information extraction is presented. This is mathematically an outer product (OP) of the $\tilde{\mathbf{U}}$ and $\tilde{\mathbf{V}}$. In a data sense, this represents the spatial and temporal patterns and their matrix product. In an abstract this is correlating the spatial and temporal patterns.

$$\tilde{A} = \tilde{U} \otimes \tilde{V}^* \tag{3.3}$$

Eliminating S effectively removes the singular value filter

3.3.6 SVD 2 - $\tilde{\mathbf{A}}$

Operating on the rank-reduced outer product of the spatial and temporal unitary matrices without consideration of the amplifier matrix elicits a spatiotemporal cross-covariance matrix. This includes all possible spatiotemporal patterns that are without consideration to the singular values.

$$\tilde{A} = \hat{U}\hat{S}\hat{V}^* \tag{3.4}$$

3.3.7 Rank-Reduce SVD 2

This purely a cleansing maneuver that maintain 99% of the outer-product of the dataset but excluding a percentage of the noise. In a signal processing sense, a cross-covariance matrix is developed. Passing the rank-reduced outer product to the SVD algorithm effectively performs a noise mitigation and that has hidden the A0 Lamb modes present.

$$\check{X} = \sum_{i=1}^{rank,r_2} \hat{u}_i \hat{v}_i \hat{s}_i \tag{3.5}$$

3.3.8 Approximate Original Dataset

An approximation of the original dataset can be made with $\tilde{A}$, this is now rank reduced where the unitary matrices U and V are only used.

$$\check{X} = \check{U}\check{S}\check{V}^* \tag{3.6}$$

3.3.9 2D FFT

Spatial and temporal amplitude behavior describes the Lamb mode that is present in space time. The S_0 and more often, A_0. This behavior has been better represented now that the original dataset is unaffected by the singular values.

$$\check{X}(x,t) - > \check{F}(\kappa, f) \tag{3.7}$$

3.3.10 Wavenumber-Frequency Spectra

Casting the 2D FFT into the wavenumber-frequency domain and looking in the upper right quadrant, this is the domain of interest. The signal has a threshold applied to extract all modes with ridges greater than some minimum number

$$\hat{S} = \frac{\check{F}\check{F}^{*}}{df * d\kappa} \tag{3.8}$$

3.3.11 Phase Velocity

Anything greater than a specified minimum amplitude in the ω v. f is kept and used in the phase velocity estimate of the plate.

$$C_p(f) = \frac{\omega}{\kappa} \tag{3.9}$$

At the conclusion of the Phase Velocity Estimation step, the analysis of the spatiotemporal data is complete. The flow chart, Figure 3.1 helps tie the written description to the step in the process.

3.4 Experimental Results

3.4.1 Overview

Two different aerospace materials were examined with the WAVSVD algorithm and the resulting wavenumber-frequency plots and estimated phase velocities for two levels of isotropy levels are presented, a subcase for the aluminum plate is included as well. The results include a traditional wavenumber-frequency analysis approach which is termed “traditional” and essentially goes from the windowed and normalized signals to the spectral domain then to the phase velocity estimate. Its just the 2D FFT approach at the core of it. The WAVSVD is presented in contrast to the Traditional method and highlights the WAVSVDs capability for enhancing the phase velocity dispersion curves for both isotropic and anisotropic materials

The isotropic case, an Aluminum 2024-T3 plate, is presented first to establish credibility and confidence in the WAVSD algorithms performance. The subcase investigates how an introduction a 12.7mm through-hole changes the dispersion relation by omitting some velocity content within the A_0 mode. This sub-case doesn’t change the material properties but introduces a potential algorithmic “tripwire”, basically indicating if the WAVSVD algorithm can handle scatter and other signal anomalies during the analysis. More importantly the damage gives us an indication on how volumetric damage influences the dispersion relationship.

The second case is the CFRP plate. The per ply material properties have been obtained from an in-situ database and used in the analytic approximation. The CFRP case is comparing the traditional and the WAVSVD approaches directly, without consideration of a through-hole.

3.4.2 Aluminum 2024-T3 Case

Wavenumber-Frequency: Traditional Approach Aluminum 2024-T3 served as the baseline, well understood, material at which the dispersion relations do not introduce any real uncertainty in the analysis. The aluminum case also serves as experimental validation with the analytic solutions and leaves no doubt that WAVSVD is functioning properly in phase velocity estimation. Presented in Figure 3.4a) is the Traditional wavenumber-frequency plot for UGW that were collected from experimentation. The wavenumber and frequencies extracted were from a hard threshold of .15*$MaxAmplitude$. all and used to calculate phase velocity.

Figure 3.4b) reveals an even stronger version of the same A_0 mode being present and having a unique frequency range between 30–200kHz and a unique wavenumber range of $10 - 125m^{-1}$.

Wavenumber-Frequency: WAVSVD Approach Now turning to the WAVSVD algorithm's estimation of wavenumber-frequency and the corresponding phase velocity plots. The WAVSVD algorithm has extended the wavenumber and frequency bandwidths, Figure 3.4.

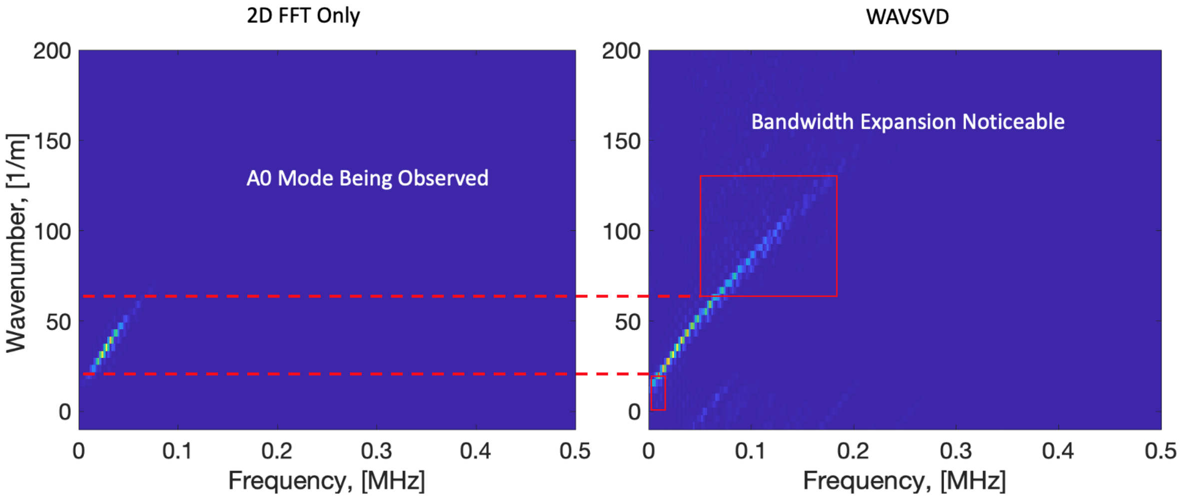

Figure 3.4: The 2D FFT vs WAVSVD and how WAVSVD reveals a bandwidth expansion in the wavenumber-frequency spectra

No other mode is present in Figure 3.4, this is expected as the A_0 flexural mode's energy is dominant relative to the S_0, longitudinal mode, that could be present in the windowed data. The same has occurred a for all other cases and will not be indicated further. The results will only focus on the A_0 mode for all cases for the remainder of the paper.

Phase Velocity: WAVSVD Approach After performing the novel WAVSVD procedure, the procedure is excellent at estimating the phase velocity with high precision and accuracy. The frequency bandwidth range is $10 - 220kHz$ while the wavenumber range is $20 - 100m^{-1}$.

WAVSVD of Aluminum Plate with Through-hole

The subcase, which investigates the same plate in a pristine state and when the plate has a 12.7mm through hole drilled out. The experimental procedure is the same for both cases. The same analytic solution is used as it does not have a shift as a result of damage. The material, within the scanning resolution, is considered pristine, i.e. any potential material property degradation surrounding the through-hole are insignificant and cause no deviation from the nominal material state. Type V impact damage is a special case of material degradation, where 100% of the material is removed. The empty space is a large impedance mismatch and mostly bounds the Lamb Waves to the A_0 and S_0.

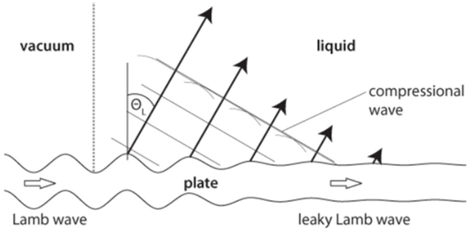

Figure 3.5: Leaky Lamb Waves as they emanate from the plate into the surrounding Air.

(Vallée, Ploix, Baqué, Cavaro, & Chaix, 2022) The only obvious degradation is the observed bandwidths and the corresponding phase velocity content measured.

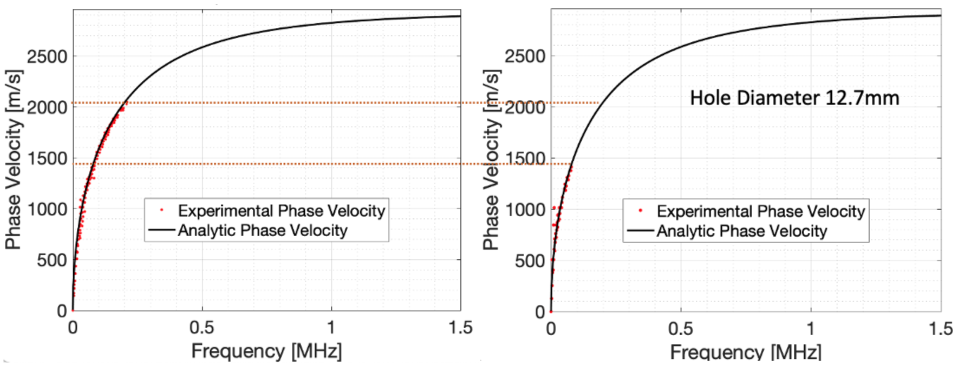

Figure 3.6: Side-by-side of 6061 Al w and w/o a 12.7mm hole with the analytic solution and WAVSVD approximation. The presence of a hole causes higher frequency phase velocity attenuation

The measured velocity decimation of the through hole is approximately 33% relative the pristine plate. This proposed technique is critical, in this case, to phase velocity calculations, but it is not unreasonable that any dataset that contains multi-dimensional information could exploit this repeated SVD approach on the outer product of the original SVD's unitary matrices. Furthermore, it is extendable as a method for inverse problems. For instance, estimation of mechanical parameters indicative of a material. This is crucial for anisotropic materials that behave as waveguides but with unknown material properties. Having precisely estimated dispersion relations will enhance the optimization scheme used for material property identification. In this case aluminum is used as a validation step. With near-term experiments being performed on anisotropic plates, like carbon fiber and fiberglass.

3.4.3 CFRP Case

Initial experimentation was performed investigating the robustness of the WAVSVD algorithm when subjected to an anisotropic material. The WAVSVD algorithm generated a phase velocity estimate of similar quality to that of the Aluminum 2024 case. The CFRP has known lamina moduli and are used to calculate the analytic solution. When comparing the experimental estimate with the analytic solution the are in reasonable agreement and suggest the extension of the WAVSVD to at least Orthotropic laminates.

Comparing the Aluminum and CFRP cases spectra, it highlights the variability of the material response to excitation.

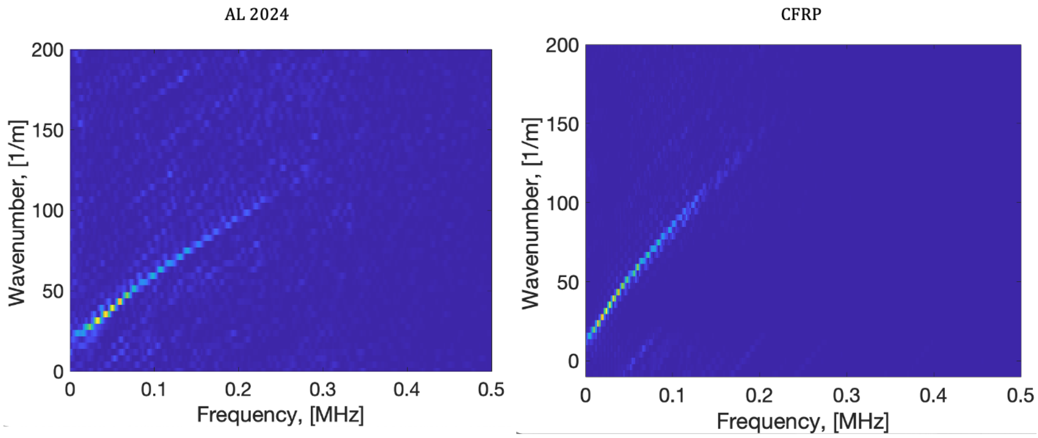

Figure 3.7: Spectral comparison between the Aluminum and CFRP cases

This indicates that CFRP and Aluminum phase velocity estimates are enhanced with the WAVSVD algorithm.

Most remarkably is the revealed bandwidth that the WAVSVD algorithm reveals. The analytic solution is currently uncertain, and the inverse solution is required to approximate the material properties of the CFRP. The inverse analytic solution is performed without optimization, which is the not conducted in this phase of research. However, the data is in a way that it would be possible to explore if the correct inverse optimization scheme can be developed.

The phase velocity estimate undoubtedly captures more of the analytic solution as opposed to the traditional estimate, Figure 3.8 clear demonstrates this bandwidth expansion in the phase velocity domain.

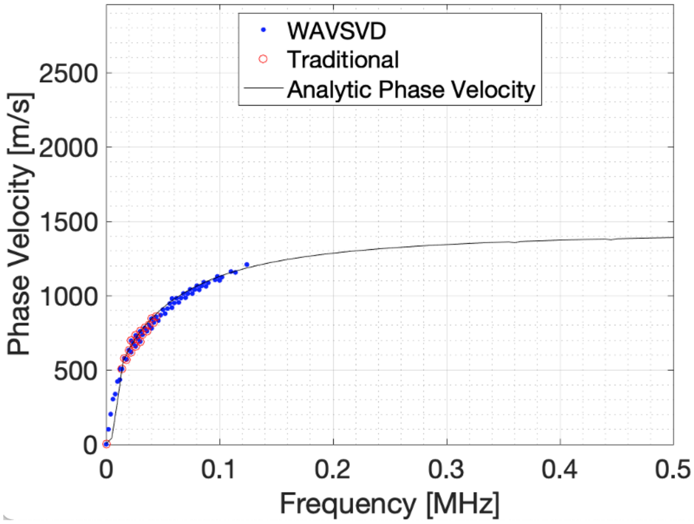

Figure 3.8: Overlay of the CFRP analytic solution, WAVSVD and Traditional estimates

3.5 Conclusion

The use of Singular Value Decomposition to reveal more spatiotemporal patterns and denoising was the mathematical ”engine under the hood”. Calculating spectra and phase velocity was straight forward once the data had been prepared via the WAVSVD algorithm. It is found that WAVSVD exhibits an expanded bandwidth in the wavenumber-frequency domain for 2024 Al relative to a traditional 2D FFT approach. The results indicate the WAVSVDs success in observing more phase velocity. The problem was then extended to 2024 Al with a through-hole to strain the algorithm. The algorithm indicated that a holes causes an attenuation of the phase velocity diserpsion, but does not deviate from the analytic healthy curve. This is an important observation as it sets up with researchers for relating impacts to holes via wavenumbers.

Since aerospace composites are common and the material that will be studied in the future, it was approriate to strain the algorithm with an anisotropic material. The anisotropy did not affect the experimental estimate of the analytic solution. After performing these validation tests, it is deemed feasible that the WAVSVD can be used to reveal hidden information.

Chapter 4

Impact Residual Strength Estimation

4.1 Abstract

In this research, a nondestrutive evaluation scheme was deployed to approximate the phase velocity of a quasi-like orthotropic carbon fiber / epoxy resin plate in different structural health states, then destructively tested to evaluate the residual strength of the specimens as a result of the varying damage states. A correlation between nondestructive results and their damage counterpart is then established.

In this research, an ideal scenario Through-hole and more real-world impact damage, are chosen as the two damage modes to evaluate. Performing the evaluation involves generating ultrasonic guided waves with an in-situ designed and built impactor. Recording the ultrasonic guided waves as the pass by the sensor are two Broadband

acoustic transducers spaced 130mm apart. The excitation as well as the sensors are broadband up to 3Mhz. Nondestructive evaluation consisted of rastering the sensor pair further and further away from the static impact excitation location. The spatiotemporal dataset records all temporal histories of wave passing within range of the sensor and along a 260mm path at increments of 1mm. Multiple data sets consisting of baseline/healthy, damaged-through hole, and damaged-impacted are considered.

Analysis of the data sets are nontrivial. The process includes pre-processing the data in preparation for the data to be passed to an in-situ algorithm termed, WAVSVD. WAVSVD ultimately calculates the phase velocity estimate from a data-driven (tailored basis) approach. in between the input and the output, the prepared data is decomposed into and reconstructed in such a way that the patterns that are physcally observed are not revealed. This algorithm then removes the singular value influence and cleanses for noise. After the mathematical operations to reveal the hidden patterns, the wavenumber-frequency spectra is calculated. Any significant amplitudes within an expected UGW mode location are preserved via thresholding and what remains is used to calculate phase velocity.

At the conclusion of the phase velocity estimate, the analytic solution should be fit to the estimate via an inverse optimization scheme, this research did not go that route. A brute force approach was used to approximate the material properties required to make the phase velocity profile true. It is the change and relationship between the phase velocity estimates and their destructively tested counterpart that drive the relationship that correlates to the NDE assessment of mechanical parameter degradation.

On the destructive side of the correlation the upfront cost is the actual damage size and strength as well as a mechanical model. The NDE signals need to correlate with the destructive data, in this case material moduli are compatible information between the NDE and destructive testing. This mechanical model requirement is rooted in fracture analysis, which relates mechanical strength, damage size, and fracture toughness. The Average Stress Criteria cases for a Through-hole and for a Crack, from (Tan, 2017), can be used to ensnare the Impact case and correlate the impacts residual strength with that of the Through-hole and correlate the impact damage size to an equivalent damage size.

4.2 Introduction

A major research thrust is quantifying material property degradation from non-destructive means. This comes in the form of different techniques as illustrated in (Achenbach, 2000), (Meyendorf, Nagy, & Rokhlin, 2013), and (Haeger et al., 2016). Some of these techniques involves neural networks while some use more traditional ultrasonics.

Most simplistically, this challenge is the experimental estimate along with an inverse-problem optimization. The analytic solution is near optimized to the data as it is performed by hand. This implies that the material properties - $E_1, E_2, E_3, G_{23}, G_{13}$, $G_{12}, \nu_{12}, \nu_{13}, \nu_{23}$,and ρ are adjusted until the optimization satisfies some requirement like minimizing error. The purpose of this research is to experimentally determine phase velocity and not prove the analytic solution to the experimental data is optimal. An open source MATLAB program, DispersionCalculator (Huber, 2018) was used to calculate the analytic solution but at this time it is not iterable.

Furthermore, the goal is to expand the bandwidth of the wavenumber-frequency spectra to provide more data points in the phase velocity calculation.

4.2.1 Structural Strength in the Presence of Discontinuity

In general a discontinuity in a structure, whether a geometric or material property, will dictate how a load path develops. For instance, a tensile coupon with a through-hole, will have a non-uniform stress field. The stress field exhibits a concentration at the tangential edge of the hole, normal to loading direction. This is the case because at the free edge of the hole. The load has to have a path and in this case, the load path navigates around the hole.

What this means is that the remotely applied stress can be less than the critical stress for the structure/material, yet the stress felt in the presence of the hole could be amplified beyond the allowable limit, potentially leading to sudden failure. Therefore it is imperative to understand the effects of a geometrical and material discontinuities present in a structure to ensure continued safe operation.

4.2.2 Through-holes

ASTM D5776 is the standard for polymer matrix composites with a hole and strength testing. It serves as the template for composites with a through-hole and a guiding template for the impacted composites.

at this energy levels, impact generates a through-hole with little damage in the immediate area surrounding the hole. The purpose of this damage case was to observe how the UGW are influenced in the presence of a hole and the challenges associated with correlating the UGW to the hole size. This is an extreme case as is indicated in Figure 4.7 with Type V being the representative case.

The main point being that material surrounding the hole is considered pristine, which challenges the NDE assessment of residual strength. Despite the lack of phase velocity shift, which is influenced by the material properties of the propagating UGW, the through hole scatters the UGW. This scatter has the potential of being correlated to damage size as a result of phase velocity muting. The following experimentation indicates this degradation has a potential correlation because the frequency range at which these dispersive waves are propagating truncates to a lower frequency level relative to the phase velocity of a baseline healthy material.

A through-hole acts as a perfect damage case congruent with Impact Type V, see Figure 4.7. This ”perfect” damage is considered to provide a connection to prior studies performed by (H. S. Kim, 2020). It also serves as a grounding mechanism for the much more complicated case of impact, which will be discussed later.

Drilled Through-Holes

Carbide tipped drill bits are used to drill through the laminate. Carbide is used because the tough nature of the fiber will quickly dull the blade. A clean through-hole is desired, i.e. no backside delamination as a result of drill bit push out or the ripping/tearing of the fibers from the laminate.

Figure 4.1 shows the drill rig with a 6.35mm carbide drill bit inserted. To increase the success of drilling, a backside plate(not shown) and less aggressive actions into the laminate is warranted. These two methods require practice before successful implementation and should be practiced on a plate.

Figure 4.1: Spring loaded drill rig

Through-holes were drilled, Figure 4.1, out of the pristine CFRP plates and a total of four different hole diameters were created, [3mm 6.35mm 12.7mm and 25.4mm]. Figure 4.3 shows an example of a though-hole in a CFRP practice plate.

A 4:1 width to hole ratio was used for this experimentation. This ratio tends to highlight the tow effects for small specimens. The specimens are 250mm long and maintain their 2.1mm thickness. An MTS Servohdraulic machine was used to test the specimens in tension at the displacement rate of 2mm/min.

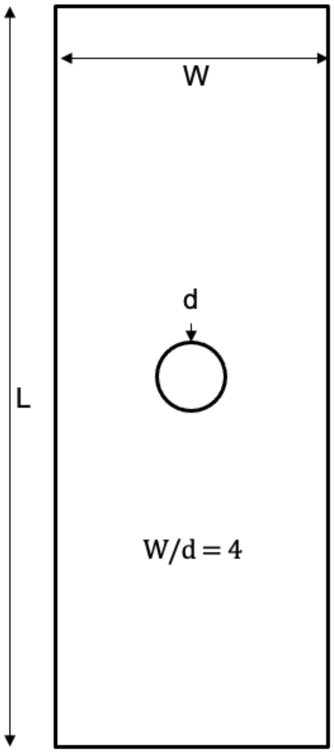

Figure 4.2: Open Hole Tension specimen design. Note that in this research $\frac{W}{d}$ ratio of 4

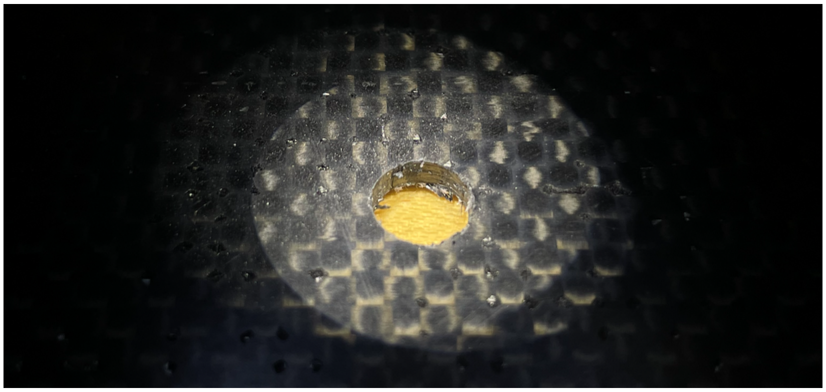

Figure 4.3: 6.35mm through-hole close up of a practice CFRP specimen. The approximate tow size is $\approx 1 - 3mm$

Pendulum Impactor Dynamics

A pendulum impactor is used to impact a CFRP specimen at a desired energy level. The dynamics of a pendulum impactor are expressed in with some simplifications (or assumptions) being made. Namely, the pendulum arm being rigid and the masses concentrated at respective centroids. Figure 4.4 indicates the geometry and mass allocation of the dynamics problem. Equation 4.1 states the kinetic energy of the system. The kinetic energy is a combination of the rotational and translational energy terms.

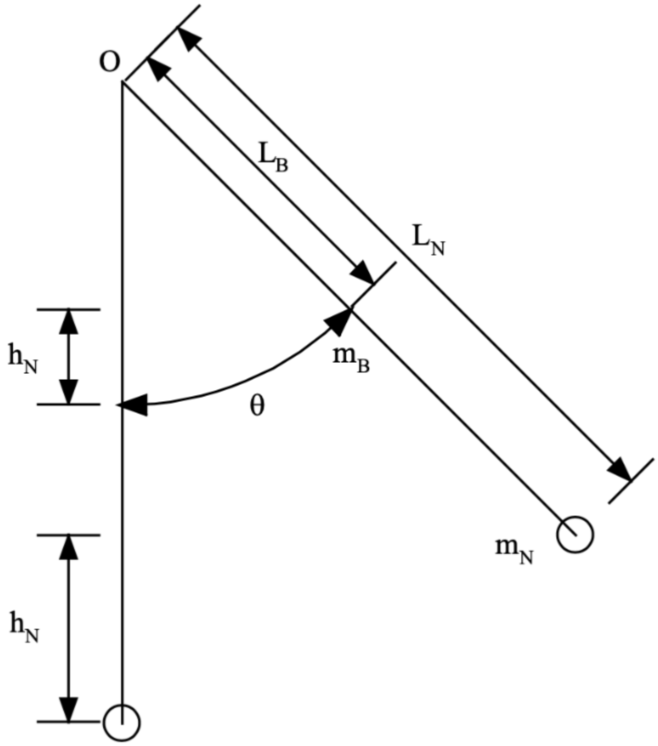

Figure 4.4: Dynamical model of a pendulum impactor

$$KE = \frac{1}{2}J\dot{\theta_B}^2 + \frac{1}{2}m_N v^2 \tag{4.1}$$

Equation 4.2 states the potential energy of the system. The potential energy is associates the heights of the respective masses above their initial starting position ($\theta = 0$).

$$PE = m_B g h_B + m_N g h_N \tag{4.2}$$

Using Equation 4.1 and Equation4.2, appropriate expression for heights and rotational inertia will be inserted.

$$h_B = L_B(1 - cos\theta) \tag{4.3}$$

$$h_N = L_N(1 - cos\theta) \tag{4.4}$$

Insertion of Equation 4.3 and Equation 4.4 into Equation 4.2 results in Equation 4.5,

$$PE = m_B g L_B(1 - cos\theta) + m_N g L_N(1 - cos\theta) \tag{4.5}$$

The rotational inertia, J_B of the bar is expressed as:

$$J_B = \frac{1}{3}m_B L_B^2 \tag{4.6}$$

$$KE = \frac{1}{6}m_B L_B^2\dot{\theta_B}^2 + \frac{1}{2}m_N L_N^2\dot{\theta_N}^2 \tag{4.7}$$

$$\dot{\theta_N} = \dot{\theta_B} = \dot{\theta} \tag{4.8}$$

recognizing that the $\dot{\theta_N}$ is equivalent to $\dot{\theta_B}$ and removing the subscript and restating Equation 4.8 to reflect this change:

$$KE = (\frac{1}{6}m_B L_B^2 + \frac{1}{2}m_N L_N^2)\dot{\theta}^2 \tag{4.9}$$

Equating KE and PE results in a perfect transfer for energy without consideration to friction or other damping mechanisms, we arrive at the energy balance that allows for the expression of the pendulum impactor velocity given an initial angle of rotation.

$$v = \sqrt{\frac{g(1 - cos\theta)(m_B L_B + m_N L_N)}{(\frac{1}{6}m_B L_B^2 + \frac{1}{2}m_N L_N^2)}} \tag{4.10}$$

Using Equation 4.9 and specifying a desired impact energy, the angle θ can be determined. Considering the idealization of the above derivation and as alluded to early, calibration of the fabricated pendulum impactor is warranted to arrive at the as-tested pendulum angle for the desired kinetic energy at impact.

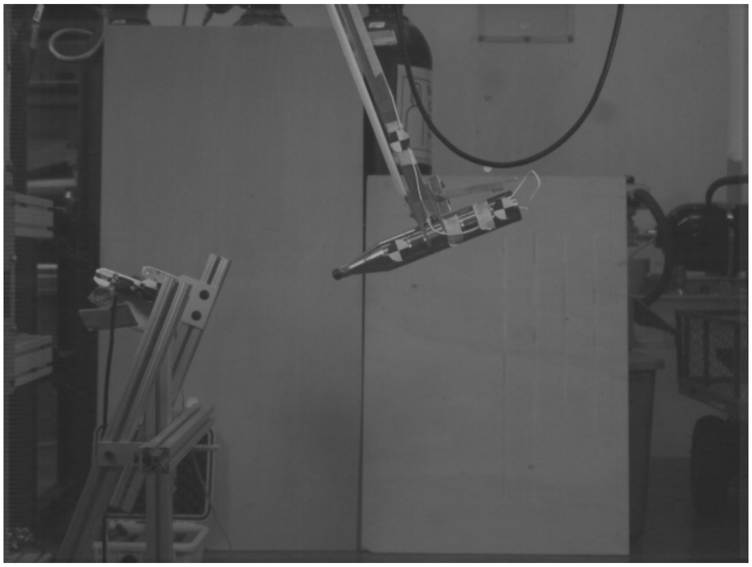

Figure 4.5: In-situ pendulum impactor during PE to KE transition

Experimental Barely Visible Impact Damages For the experimentalist knowing the velocity just prior- and post-experiment and the equivalent mass, the kinetic energy for the incoming and outgoing impact stages is capable of being known.

The impactor dynamics derivation is useful for predicting when an equivalent mass system is rotated through some angle to provide a theoretical equivalent to a physical pendulum impactor. The physical impactor has distributed mass and losses. Some of those losses come from friction in the bearing supporting the rotation of the entire pendulum system and calibrating the system to the correct angle is often required.

Experimentally, it makes more sense to have a well captured velocity approximate for an equivalent mass system. The force is being measured at the pendulum impactor tip, Figure 4.6.

The tip radius is 12.7mm.

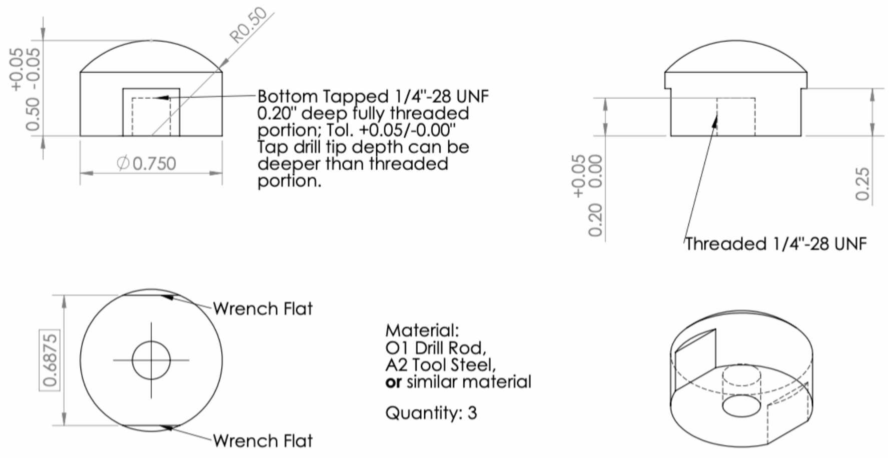

Figure 4.6: An engineering drawing of the steel impactor tip.

The force sensor is mounted on a flat face to the flat bottom face of the impactor tip and records the dynamic force as it evolves in time.

Impulse and Momentum The momentum described here is for the pendulum at the impacting velocity and is represented mathematically as:

$$P_{in} = m_{pendulum} v_{in} \tag{4.11}$$

An impulse is the integral of the force, F applied over a time, dt, see Equation 4.12.

$$I = \int_{t_1}^{t_2} F \, dt \tag{4.12}$$

4.2.3 Impact Damage Mechanisms and Severity

Impact damage is one of the most common mechanisms seen on aircraft and directly motivates this research. This can come from something as small and singular as stone impacting the structure or something as large and energetic such as Ground Service Equipment (GSE). A scale of impact damage and the energy required to cause the damage is used to generally quantify the damage severity, see Figure 4.7 (H. Kim, Welch, & Kedward, 2003) .

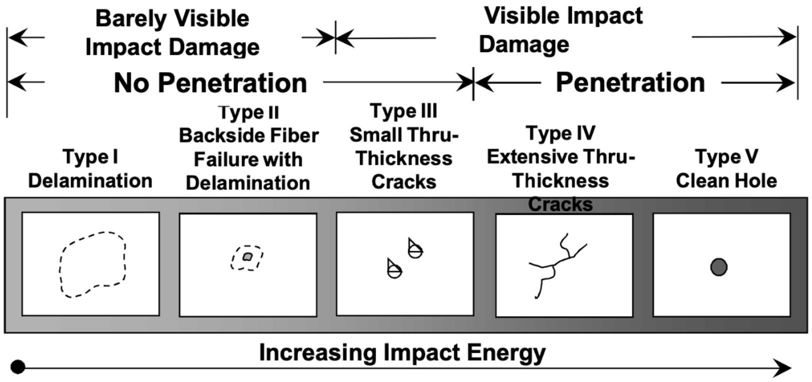

Figure 4.7: Impact damage levels and with the increasing impact energy

Barely Visible Impact Damage, BVID Damage Type I and II are often challenging to detect. Frequently these Types are barely visible, if not undetectable to a trained eye. Adding to the challenge, BVID nearly undetectable from the external side of the structure. This requires evaluation schemes that are not human-centric. For example, delamination damage is difficult to visually identify as they are often internal to the skin and detectable via nondestructive scans either through ultrasonic guided waves or or thermography.

Visible Impact Damage, VID Types III-V are easier to detect relative to Types I and II, namely because a potential exists for visual detection. Observation of VID adds a human dimension. An inspection technician is able to reliably detect most surface-adjacent cracks. The converse perspective is that VID implies that damage needs to be addressed at the next maintenance interval. The caveat being the impact damage does not compromise safe operation.

Impact Damage Prognosis Determination of the damage prognosis is of utmost importance for the continued safe operation of the vehicle or structure. Determining the prognosis of an impact site requires a few key metrics:

1. Damage geometry which relates to how a stress field could develop in the presence of a loading mechanism
2. Quantification of the material's property degradation
3. Knowledge of the baseline, comparative, material properties.

4.2.4 Phase Velocity UGW Dispersion

Phase Velocity Estimation from Experimentation

Phase velocity describes the plate wave mode propagation velocity as a function of frequency. Simplistically, the phase velocity at which the modes travel at are determined from an intermediary step in which modes amplitudes in the wavenumber-frequency domain are selected. Phase velocity is the proportion of frequency to wavenumber and plotted at that given frequency. The dispersion curves are more straightforward via experimentation with careful consideration of isolating the significant features in the wavenumber-frequency domain. The drawback is the spatial resolution. To have a fine resolution in the wavenumber domain, the spatial resolution needs to be small, i.e. on the order of a mm, and many data points need to be collected. Otherwise, it is straightforward and becomes a signal processing challenge to identify as much information as possible from the data.

Phase Velocity From Analytic Solution

Calculating the analytic solution of phase velocity is non-trivial and is a transcendental equation meaning that the solution must converge with some error metric involved. For this research, an open-source, MATLAB-centric, software program (DispersionCalculator) is used. The DispersionCalculator is validated with the for-purchase software, Disperse. Disperse is widely used in academia and industry.

Phase Velocity Both Analytic and Experimental

The DispersionCalculator software, (Huber, 2018) is implemented via a brute force approach for approximating the phase velocity curve of the experimental data. This brute force approach is not optimized and leaves room for an optimization scheme to be built into the approximation.

The brute force approach invloved generating a grid of phase velocity curves at different percentage decrements of moduli. All of the moduli were degraded equivalently, except for the Poisson's ratios, they remained the same. The brute force grid is then overlaid with the experimental estimate and refined from there.

Despite the brute force approach, the idea of using a degradation of the mechanical parameters used to calculate the analytic phase velocity curve to represent the material degradation observed in experimental data sufficiently demonstrates the procedure to obtain mechanical parameters for the estimation of residual strength.

4.2.5 Stress Concentrations Due to Geometric Anomalies

Developing an understanding about the stress (strain) distribution about a hole is not trivial. Note that strain is a viable and equivalent substitute for ideal cases like holes and cracks. Figure 4.8 a) requires an equation that is dependent upon the laminate-hole geometries and the material properties. The main reason is that in the presense of the hole, a Stress(strain) Concentration Factor can be plotted, Figure 4.8 a), for the line normal to the loading direction at the location R on the positive y axis. This will be the location of max stress or strain concentrations. Figure 4.8 b) is a semi-empirical model that relates stress (Strain) concentrations and their distribution to a failure stress (strain). They are related with an integral of the distribution along dx. The whole integral is normalized by a_o and is approximately the same for the same laminate with different size holes and widths. In this research the plate width ratio is maintained at 4:1.

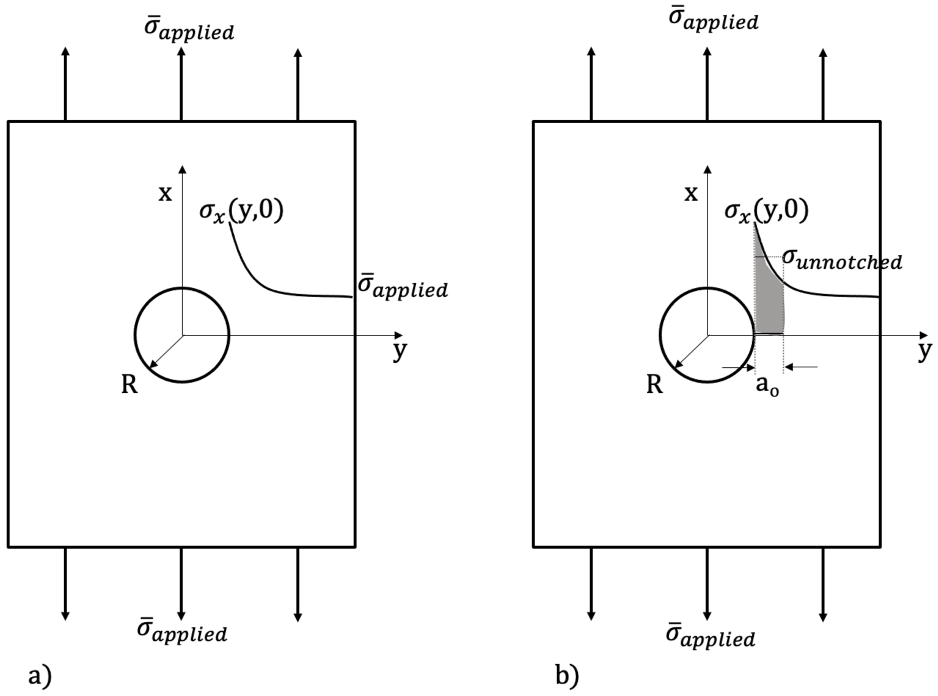

Figure 4.8: a) Stress distribution along the y-axis as a result of an applied load. b) Graphical representation fo the Average Stress Criteria. Note that the Radius, R, is the same as the Half Damage Size, a

The stress distribution is best modeled as a linear combination of an isotropic solution and an orthotropic solution (Tan, 2017), all along the axis normal to the loading direction, see Figure 4.8

$$\frac{\sigma_x(y,0)}{\bar{\sigma}_{applied}} = F_{Isotropic} + F_{Orthotropic} \tag{4.13}$$

From the complex analysis the full, normalized stress distribution is shown in Equation 4.14. The equation is broken down into the two respective solutions. The first three terms are the isotropic solution, while the last term is the orthotropic solution. This is the stressdistribution along the y-axis.

$$\begin{aligned}\frac{\sigma_x(y,0)}{\bar{\sigma}_{applied}} = 1 \quad &+ \quad \frac{1}{\sqrt{\gamma^2-1+\lambda^2}(\gamma+\sqrt{\gamma^2-1+\lambda^2})} + \frac{\lambda^2(1+\lambda)(\gamma+2\sqrt{\gamma^2-1+\lambda^2})}{(\gamma^2-1+\lambda^2)^{1.5}(\gamma+\sqrt{\gamma^2-1+\lambda^2})^2} \\ &- \quad \frac{\lambda^7}{2}(K_t - 1 - \frac{2}{\lambda})(\frac{5\gamma}{(\gamma^2-1+\lambda^2)^{3.5}} - \frac{7\lambda^2\gamma}{(\gamma^2-1+\lambda^2)^{4.5}})\end{aligned} \tag{4.14}$$

Many notations are introduced to simplify the expression. $\gamma = \frac{y}{a}$ is the width to hole aspect ratio and $\lambda = \frac{b}{a}$ is the hole x-y geometry aspect ratio, Figure 4.9.

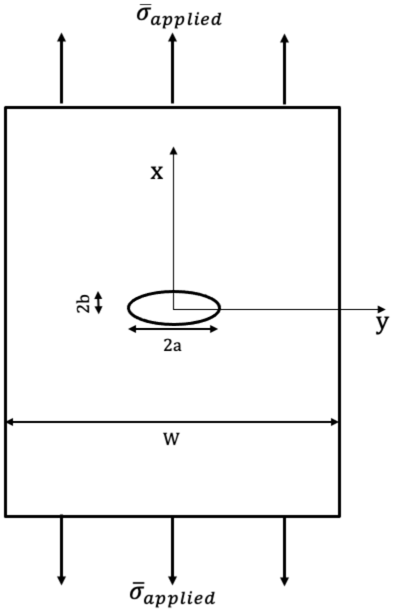

Figure 4.9: These ratios are developed from an ellipitical hole, as it can both approximate a circular hole $b = a$ or a crack when $b- > 0$. γ is measured from the edge of the ellipse, $y(a)$ to $y(W)$

This stress distribution equation is also dependent on a finite width plate stress concentration factor of the laminate, K_t. Calculating K_t begins with calculating K_∞ (Tan, 2017), which utilizes Classical Laminate Theory material parameters from the Extensional Coupling Matrix, $\mathbf{A}$.

$$K_\infty = 1 + \frac{1}{\lambda}\sqrt{\frac{2}{A_{22}}(\sqrt{A_{11}A_{22}} - A_{12} + \frac{A_{11}A_{22} - A_{12}^2}{2A_{66}})} \tag{4.15}$$

The infinite plate assumption needs to be corrected to a finite plate SCF. This is achieved using a function that relates the finite plate geomtery and infinite plate SCF (Tan, 2017). Therefore the Finite Width Correction (FWC) factor is presented and amplifies the infinite plate SCF. The *inverse* FWC for a hole is presented in Equation 4.16.

$$\frac{1}{FWC} = \frac{K_\infty}{K_t} = \frac{3(1-2a/W)}{2+(1-2a/W)^3} + \frac{1}{2}(\frac{2a}{W}M)^6(K_\infty - 3)(1-(\frac{2a}{W}M)^2) \tag{4.16}$$

Included in the FWC equation is a magnification factor (Tan, 2017), M and is expressed as:

$$M^2 = \frac{\sqrt{1 - 8(\frac{3(1-2a/W)}{2+(1-2a/W)^3} - 1)} - 1}{2(2a/W)^2} \tag{4.17}$$

Finally, the finite SCF, K, is expressed as Equation 4.18, and can be substituted into Equation 4.19.

$$K_t = K_\infty * FWC \tag{4.18}$$

Stress Concentration Distribution Equations For this research, a hole is considered with an aspect ratio, $\lambda = 1$. This simplifies Equation 4.14 and setting the applied stress to the max strength of the laminate:

$$\frac{\sigma_x(y,0)}{\bar{\sigma}_{unnotched}} = \frac{1}{2}(2+\gamma^{-2}+3\gamma^{-4}-(K_t-3)(5\gamma^{-6}-7\gamma^{-8})) \tag{4.19}$$

Equation 4.19 can now used for this research. The laminate's **A** matrix is constant for all specimens with only hole diameters being varied between 3-25.4mm to provide an estimate of the normalized stress distributions from the hole edge $y = 0$ to the edge of the laminate $y = W$ along the y-direction.

Average Stress Failure Criteria for Damaged Laminates Using the mechanical parameters determined via the DispersionCalculator is not enough to make a statement about residual strength. Laminated composites are complex. For instance, the ply angle, stiffness and max strength could differ layer to layer which all affects the global, laminate-level, stiffness and max allowable strength. The addition of damage further complicates the expected behavior of a laminate.

The Average Stress Failure Criteria is invoked, see Figure 4.8 b) to determine the strength at which a laminate with damage is expected to fail. Equation 4.20 is calculating a_o to be the distance away from the edge of the hole when the integral of the stress distribution becomes equivalent to the unnotched laminate strength.

$$\sigma_{unnotched} = \frac{1}{a_o}\int_{a}^{a+a_o} \bar{\sigma}_x(y,0)\,dy \tag{4.20}$$

Equation 4.20 implies that the failure stress of the laminate is a volumetric measurement of stress that is normalized by the characteristic distance, a_o.

The presence of a hole/crack/or ellipse...,will cause a nonlinear stress distribution over the distance, a_o, when integrated will be equivalent to the unnotched laminate strength (Tan, 2017).

$$\frac{\sigma_{unnotched}}{\sigma_{applied}} = \frac{(a^2(\frac{-a^6(K_t-3)}{(a_o+a)^7}+\frac{a^6(K_t-3)}{a^7}+\frac{a^4(K_t-3)}{(a_o+a)^5}-\frac{a^4(K_t-3)}{a^5}-\frac{a^2}{(a_o+a)^3}+\frac{a^2}{a^3}-\frac{1}{(a_o+a)^7}+\frac{1}{a})+2b)}{2b} \tag{4.21}$$

Equation4.21 is the simplified average stress integral normalized by the laminate's unnotched strength and is the strength reduction ratio, SRR. From Equation 4.21, a_o can be measured as the physically true length from the edge of the damage until the distance a_o is reached which is when the area under the curve from R to $R + a_o$ is equivalent to the unnotched laminate strength, see Figure 4.10.

A simplified (Daniel et al., 2006) version of Equation 4.21 becomes:

$$SRR_{hole} = \frac{2}{(1-\gamma)[2+\gamma^2+(K_t-3)\gamma^6]} \tag{4.22}$$

recall $\gamma = \frac{y}{a}$

In this dissertation the Equation 4.22 is used when calculating a_o.

Ideal Cracks Recalling Figure 4.8, which is the Through-hole Case, the circular hole can be substituted with a Crack case and undergoes the same treatment just mentioned, Figure 4.10 to develop the SRR_{crack}

$$SRR_{crack} = \sqrt{\frac{a}{a+a_o}} \tag{4.23}$$

Figure 4.10a) is a general sketch for the stress distribution adjacent to the crack a) The stress distribution develops as a result of a sharp discontinuity that forces the load paths to navigate around the damage. We can measure the stress field along the y-axis and us it in the analysis to help determine at what location away from the edge of the crack does the integral of that stress distribution become equivalent to the unnotched strength of the laminate, this is what Figure 4.10 b) is highlighting.

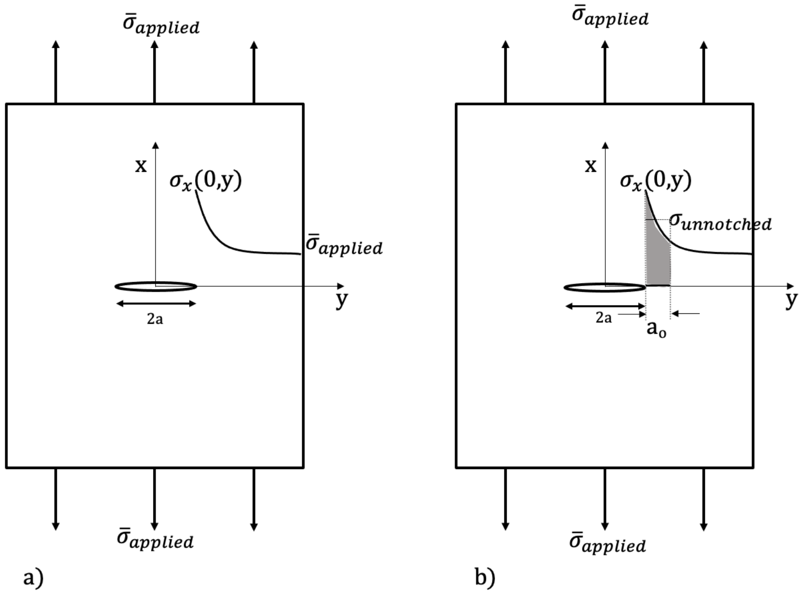

Figure 4.10: a) Stress (or a strain) distribution along the y-axis as a result of an applied load. b) Graphical representation fof the Average Stress Criteria for a crack. Note that for the crack the crack length is 2a, in the through-hole case, the damage size was given as Radius, R. For transparency, $R = a$

Variable Damage Mode and Size This research asserts that the characteristic damage size a_o will exist for any damage and can be related to the Through-hole and Ideal Crack Cases. This assumption implies that the Variable Damage Mode and Size falls between the extremes, Through-hole and Crack.

In this case, the stress and/or strain field(s) can be best measured using Digital Image Correlation and assuming plane stress. The stress distribution, Figure 4.11, from the edge of the damage to the edge of the plate can be measured. From this distribution, a function can be fit to the data and integrated in the Average Stress Equation, Equation 4.20. From this integral, a_o can be estimated.

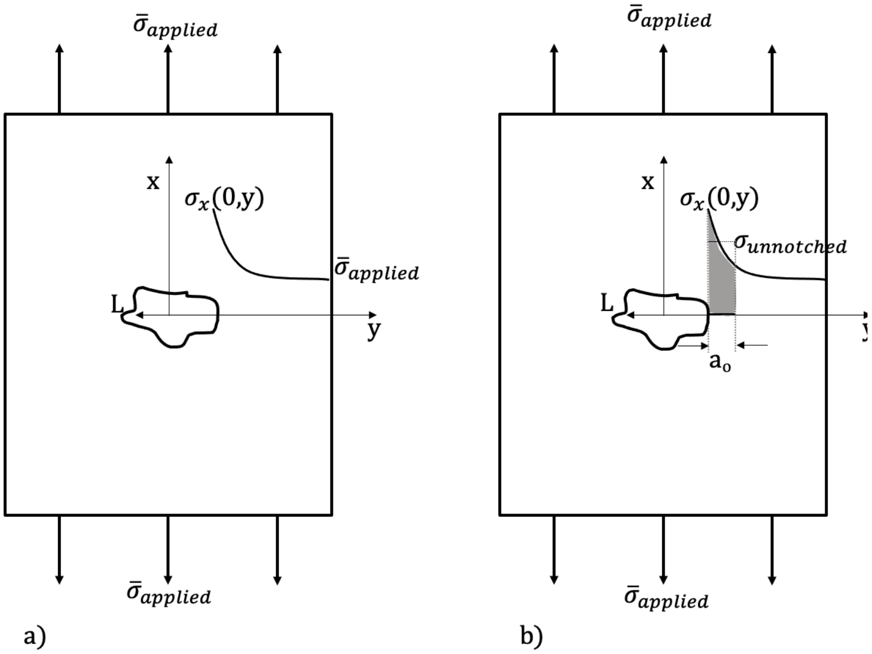

Figure 4.11: a) Stress distribution along the y-axis as a result of an applied load. An representative gross damage size is represented as L. Other geometric dimensions can also be included. For instance, if the damage shape is hexagonal, the representative geometric features of the hexagon can be used. b) Graphical representation fo the Average Stress Criteria for any shape

Maintaining Big Picture Just to stay on track, the goal is to measure residual structural strength from nondestructive means, the Average Stress Criteria requires destructive testing. The results from the destructive testin regime serves as a validation scheme.

4.2.6 NDE and Impact Residual Strength Relation Goal

The analysis goal is multi-faceted with the ultimate goal of predicting residual strength of a damaged component or a structure. The analysis goal is to take advantage of the assumptions to unlock tools in the Average Stress Criteria Model. Recall, this model can neatly relate and overlay a crack and a circular hole residual strengths. Equation 4.19.

In this dissertation it is asserted that the impact damage is somewhere between a crack and a hole and thus allows for an adaptation to an existing frame work to estimate an residual strength from their respective NDE scan data.

Identifying a characteristic damage length is thus possible and can be used to relate the impact damage to the a hole or a crack. The assumptions being:

1. Impacts generate nonlinear behavior in an otherwise linear elastic behavior
2. Material Degradation exists on a spectrum. Volumetric Impact Damage (e.g. matrix cracking, delamination, minute fiber breakage...) falls on the Material Degradation Spectrum
3. Ideal Cracks/Holes exist on the spectrum and is a special case by being the lower limit (Healthy is the the upper).

4. The Impact case lies somewhere between a Material Degradation type (Type V and I Impact Damage) and an Ideal Crack (Type III-VI Impact Damage).
5. The sum of impact damages are effectively modeled as a weighted mixture of the Average Stress Criteria's Through-hole and Ideal Crack cases. This mixture allows for the correlation to Average Stress residual strength and damage size.

Assumption 2 parallels nicely with the Impact Damage Type, see Figure 4.7. For instance, delamination (Assumption 4) as indicated by the C-scans, are the Hole Case. The loading direction (1-direction) is parallel to the laminae and spans an area. Theoretically, the delamianted region will be bound by the strength of the representative volume element's fiber when the matrix properties are degraded. This volumetric degradation introduces a stress/strain concentration but one that is not as "extreme" as a crack.

Assumption 5 unlocks the capability of the full Average Stress Criteria equation set. In this analysis, all of the impact CFRP specimens have front side crushing damage and backside fiber breakage, along with internal delaminations . The fiber breakage the Ideal Crack Model while the crushing damage and delaminations are the Though-hole Case.

Correlating Phase Velocity and Physical Damage

Correlation of residual strengths are possible. By assuming the Material Degradation Spectrum Figure 4.12, the Average Stress Failure Criteria mathematical models are now an accessible tool set to frame residual strength of impacts.

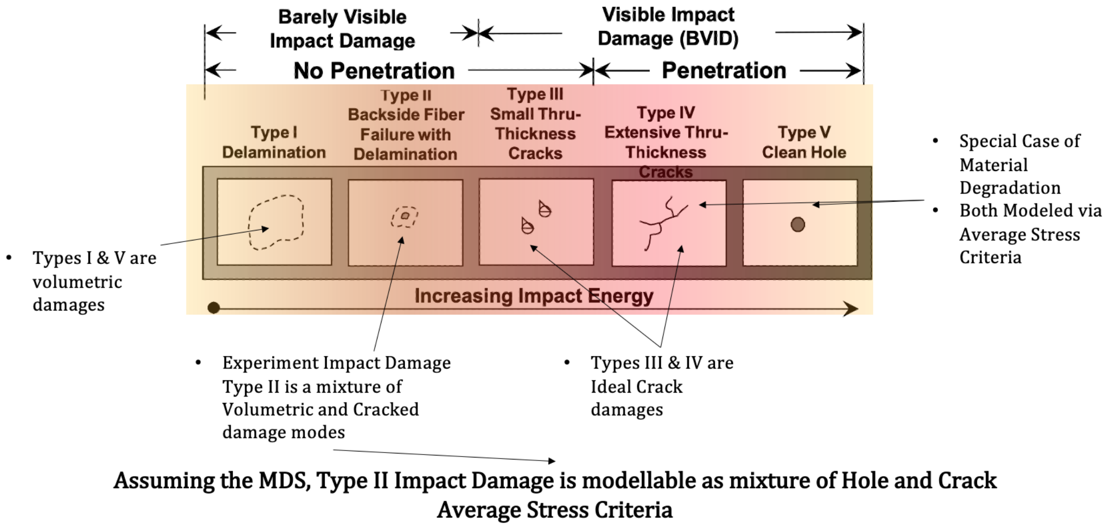

Figure 4.12: Experimentally determined residual strengths for the through-hole and impact specimens with their predicted residual strengths.

The assumption being that if impact damage is present then residual strength can be modeled as a weighted mixture of the stress (strain) distributions for holes and ideal cracks, Equation 4.24. Then the impact too should be correlated with the other hole and crack residual strengths. This graphically represented with Figure 4.12, where the color gradient highlights the relationship between the two different Average Stress (Material Degradation and Crack). Type II and III fall between the pure crack and pure material degrdation, so it is framed by their respective stress distribution profiles. These are the stress (or strain) distributions from edge of the damage to the edge of the plate.

$$\sigma_x(y,0)_{Impact} = w_1\sigma_x(y,0)_{Hole} + w_2\sigma_x(y,0)_{Crack} \tag{4.24}$$

Notice weights, w_1 and w_2, these are representative of how much of the impact is like a through-hole and much the impact is like a crack. The weights always sum to 1.

The current goal is to appropriately insert knowledge into the Average Stress Criteria in ways that correlates the residual strength of an impact with a hole and thus a crack. This approach comes from observation of phase velocity diagrams which is the next topic, Characteristic Damage Wavelength.

Characteristic Damage Wavelength, a_κ

Using the WAVSVD algorithm to extract the phase velocities and associated damaged wavenumber provides a characteristic damage length that will be inserted in place of a_o.

Observing prior studies used in the WAVSVD Chapter, the A_0 phase velocity curve that is measured from an aluminum plate with a 12.7mm through-hole and scanned via the SISDO approach shows that the corresponding phase velocity and frequency truncate. This is a measure of damage that is a characteristic damage wavelength. This characteristic damage wavelength is measured from phase velocity is a_κ.

Obtaining the characteristic wavelength,a_κ, is straightforward:

1. Measure the C_p vs. f of the specimen
2. Observe specimen C_p vs.f relative to a known baseline healthy
3. Select Cp_{max} and $2\pi f_{max}$ from damaged phase velocity estimate.
4. Calculate wavenumber, $\kappa = \frac{2\pi f_{max}}{Cp_{max}}$.

5. Calculate characteristic wavelength $a_\kappa = \frac{1}{\kappa}$.

Relating with Through-hole

Being a volumetric mixture of the materiel degradation and cracks and having a characteristic damage size, a_κ, that is influenced by damage severity. The damage severity is recognized as the attenuated high frequency content which is in experimental agreement with a Through-hole case, Figure 4.13.

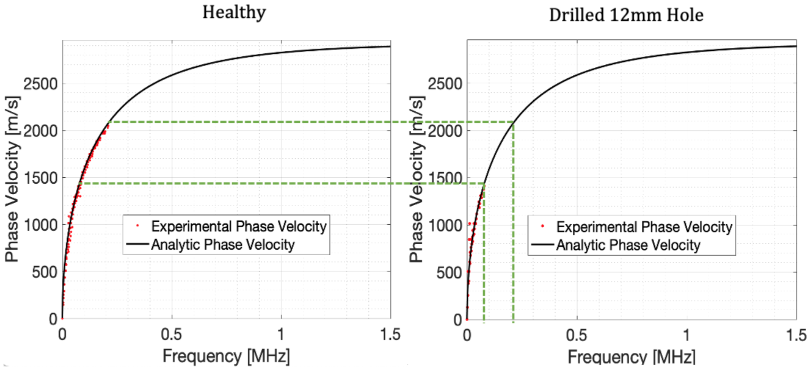

Figure 4.13: Attenuation of C_p and f due to a 12.7mm diameter hole

It is now possible to estimate the residual strength relative to the through hole case.

6. Replace a_o with a_κ in Equation 4.30 along with the known K_{IC} and a. ± is indicates direction to take the characteristic wavelength. If dominated by Crack, use $-$. If a hole dominated, use $+$.

7. Solve for the estimate of the residual strength, $\sigma_{Damaged}$.

$$\sigma_{Damaged} = \frac{K_{IC}}{\sqrt{\pi(a \pm a_{\kappa})}} \tag{4.25}$$

8. Normalize the impacted strength estimate, $\sigma_{Damaged}$, by the ultimate strength, σ_{ult}, of the laminate, resulting in the residual strength estimate, $\sigma_{r,\kappa}$.

$$\sigma_{r,\kappa} = \frac{\sigma_{Damaged}}{\sigma_{ult}} \tag{4.26}$$

Therefore the Through-hole Average Stress equation correlates the impact damage to the Average Stress model via characteristic length, a_{κ}.

This is not enough though because the holes and impacts are only correlated to the residual strength level, not damage size. Therefore it is necessary to establish an equivalent crack size for an impacted specimen.

Correlating with the Ideal Crack

Therefore an additional relation needs establishing to bring the Impact Residual Strength into an equivalent stature as the Through-hole Residual Strength. Correlating to a characteristic crack length seems most desirable, therefore using the Equation 4.20 for the Crack case is used. Figure 4.14 highlights the contributions from each case in establishing an equivalent crack length, a_s.

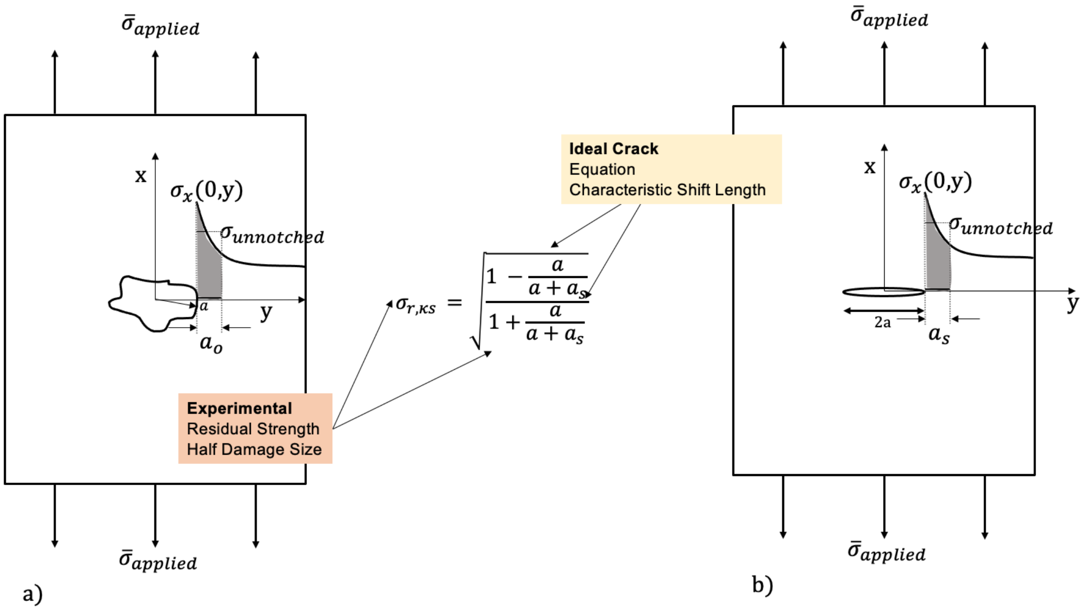

Figure 4.14: Identifying an equivalent crack for the given experimental impact size and residual strength and analytic model

The equivalent length, a_s, is not the length of the equivalent crack. a_s is used, along with a_κ, to correct the impact half damage size, a back to an equivalent crack.

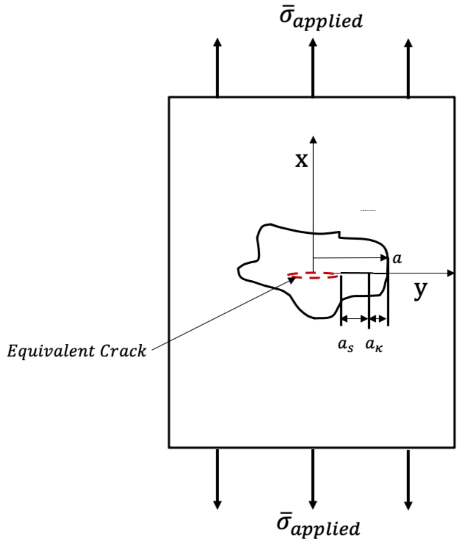

Figure 4.15: Identifying an equivalent crack for the given experimental impact size and residual strength and analytic model

9. Use dominant Average Stress Criteria case: Through-hole or **Crack**?
10. Insert the Residual strength $\sigma_{r,exp}$ and half damage size perpendicular to loading direction, a into Equations 4.27 and 4.28.

$$\sigma_{r,exp} = \sqrt{\frac{1-\zeta}{1+\zeta}} \tag{4.27}$$

$$where, \qquad \zeta = \frac{a}{a+a_s} \tag{4.28}$$

11. Solve for Equation 4.27 for a_s

12. Adjust the 4.25 to account for the equivalent crack shift.

$$\sigma_{r,\kappa s} = \frac{K_{IC}}{\sqrt{\pi(a \pm a_\kappa - a_s)}} \tag{4.29}$$

This is striking. The characteristic correction length, a_s is computed by the Ideal Crack case mathematics, provides the desired correction length correlating residual strengths of the impact to that of the through-hole. Furthermore, it quantifies an equivalent crack size for an Impact case when framed

In this dissertation the dominant mode was cracking. Therefore using it is possible to determine the correction factor from the Ideal Crack Solution used to determine a_o.

4.3 Experimental Backbone Setup

Engineering is a multifaceted field that demands multiple perspective, often disjointed, to come together to understand a phenomena. The methodology at which we connect the topics is crucial for a quality outcome. This methodology is rooted in three major abstractions. 1) We must know how to represent an aerospace structures/components concept in the real world, i.e, manufacturing or fabricating. 2) Comprehension of damage modes relative to the aerospace structures domain. 3) We must know how to ask the structure relevant questions to obtain a response that is translatable into engineering. 4) Modeling of the scenario can help provide insights that are not readily observable in experimentation. In layman's terms, understanding how to make, break, sense, and model the scenario is important for comprehending the complexities associated with a process.

4.3.1 Carbon Fiber/Epoxy Plate Manufacturing

The plates used in experimentation are representative of an aerospace skin are manufactured from Hexcel 282 3K Plain carbon fiber fabric. The laminate has a layup sequence of $[0/45/0/-45/0]_s$, which is not a true orthotropic laminate but the plain nature of the fabric balances the ply angles and results in an orthotropic plate. The plate was manufactured using the Vacuum Assisted Resin Transfer Molding (VARTM) technique, Figure 4.16. This infusion technique requires a low viscosity resin to infuse the dry fabric as it is being drawn towards the exit vacuum port. Once the fabric stack has been impregnated, the laminate is left to cure for 24hrs. A second post-cure heat cycle is used to maximize the material properties of the laminate. Ultimately, this manufacturing method produces a near uniform plate, in terms of thickness and material properties. These composite laminate mechanical properties of the as manufactured plate constitutes the material properties of a healthy specimen.

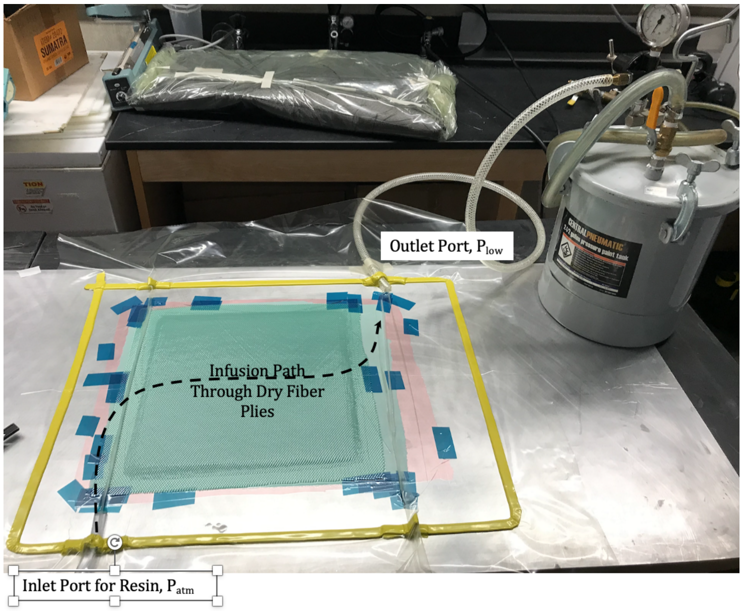

Figure 4.16: Example of VARTM Method being applied to practice laminate

At the conclusion of the VARTM process two plates, both identical layups, were manufacttured. The VARTM process creates uniform laminates. The average thickness for both plates is 2.1mm. The thickness varied by ±mm across the entire area. Defining an individual plate's area is the length of 1.0m and width of 0.75m. From this stock of two platesl, the Through-hole, impact, baseline and NDE specimens were all acquired.

4.3.2 Mini-impactor Selection

An excitation source is required. A Mini-impactor was selected based upon prior studies to serve as the source. The nominal thickness of the CFRP laminate is 2.1mm, the nearest suggested Mini-impactor is the 8ply-88mm. As indicated in prior studies, this Mini-impactor generates a significant excitation relative to the average excitation.

The superior excitation exhibited by the 8ply-88mm impactor for a CFRP plate this size strongly excites the A_0 and S_0 plate wave modes.

4.3.3 Single Impact, Dual Sliding Output

The single input, sliding dual output (SISDO) technique was deployed to observe the plate under impact excitation and it's response. The number of locations scanned are predicated by the resolution desired in the wavenumber domain. In this case, the spatial resolution is 1mm. Figure 4.17 highlights the SISDO system. The Broadband Acoustic Transducers (BAT) are rastered as a pair away from the excitation location, which remains constant. The BATs were also arranged in a pair to reduce the amount of time required to collect data by half.

The spacing of BAT 1 from the excitation source in the initial location is 100mm, this is mostly due to equipment and access to the MI shim for removal. The BAT sensor pair is separated by 130mm, which equates to 260 data points interrogated. This length was chosen because of the constraints on the specimen geometry. It is possible to have different lengths for these to cases, the only warning is that the sensors must raster ahead of and behind the damage sufficiently.

A similar experiment is a pitch/catch test, SISDO is a rastering pitch/catch measuring ultrasonic guided waves as the are sensed with broadband acoustic transducers.

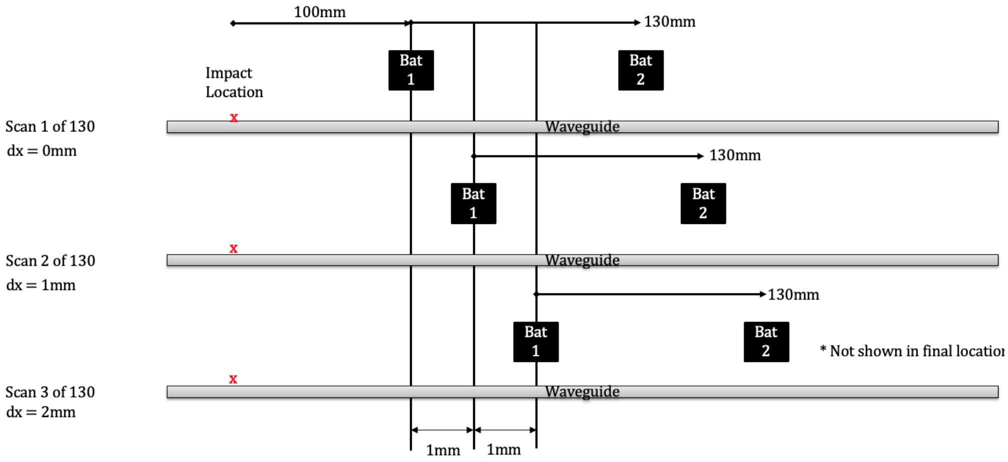

Figure 4.17: General Concept of SISDO

Sensor-Mounted Linear Stage Translator

The nature of generating wavenumber-frequency diagrams, experimentally, can be time consuming. The reason it can be time consuming is the spatial sampling. To have sufficient wavenumber resolution one must sample in space finely. For this research, an in-house built linear stage translator was used to increment the sensors in space at a resolution of 1mm. The fabricated linear stage translator (LST) was instrumented with a digital caliper, Figure 4.18 Side View, to monitor the translation. The LST has an option to set the BATs at any angle desired. The angle can be exactly selected for this material via Snell's Law for Refraction. In this case, the sensor angle was calculated to be 13 deg. This comes from the speed of sound of the two materials the wave will be propagating in, air and CFRP, the angle of the plate.

It is to be noted that slack does exist in the linear stage translator and minute UGW scan errors are noticeable but not influential. '

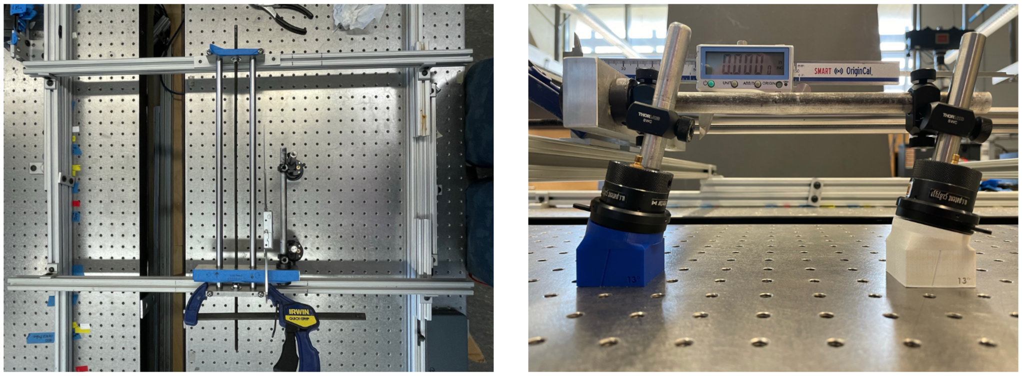

Top View

Side View

Figure 4.18: Linear Stage Translator top and side views

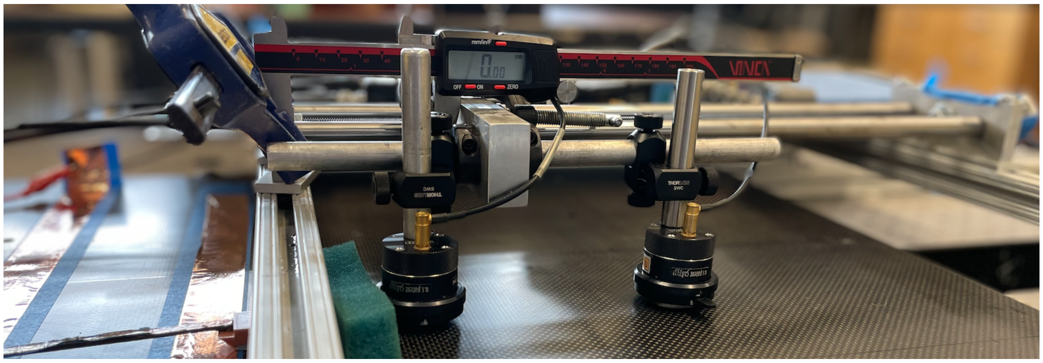

Figure 4.19: Fabricated Linear Stage Translator at the Origin. A digital caliper is used to precisely locate the broadband acoustic transducers along the scan path. Note the 8ply-88mm impactor to the left

Spatiotemporal Data and Arrangement

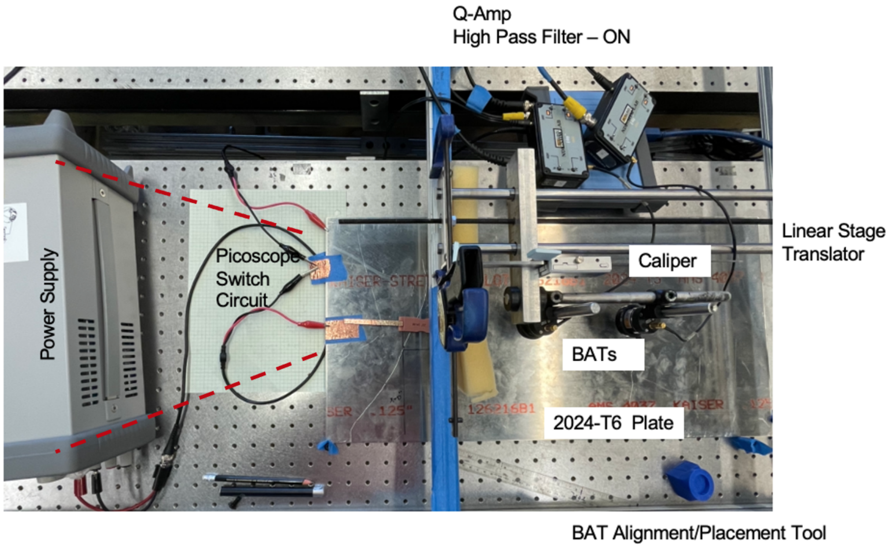

Figure 4.20: Simple switch circuit schematic

The raw data collected is voltage excitation time histories from the BATs at each scanned location. Using the SISDO technique reduced the experimental time in half. Using Figure 4.21 a) to visualize the data storage scheme, where every row is a scan with the rows sorted in descending order. The columns are a time instance in the experiment. Filling the cells are the amplitudes measured from the BATs. If you then substitute in the data Figure 4.21 b) becomses more digestable. Starting at the bottom of 4.21 b), the yellow box exemplifies all the wave content associated with Scan 1. The scans go on populating the data storage scheme with spatiotemoral UGW data. Figure 4.21 shows 260 scans, but only 130 scans were performed. The numbering scheme maintains congruence with the spatial location measured. So Scan 1 is at the 1mm location with BAT 1. If we are at Scan 131, this is BAT 2 at 131mm.

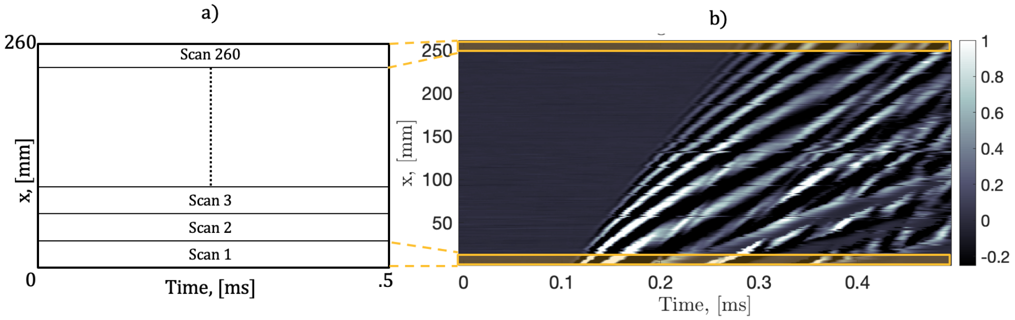

Figure 4.21: Every scan is arranged into a spatiotemporal representation. a) Shows how each scan is arranged from bottom to top and b) it's correspondence to the spatiotemporal data

WAVSVD

The WAVSVD algorithm, prior mentioned in Chapter 3.1, is used for the bulk of the analysis. For all cases the windows, thresholds and limits were held constant as seen fit by the researcher, this a source of bias.

WAVSVD Windows and Thresholds Commentary The analysis is sensitive to the windowing and thresholds. A non-optimized, but carefully scrutinized process was used to determine the window type, width, and the best thresholds. Regardless of the optimatlity of the window and the thresholds, the goal is to develop a data-driven tailored basis that encodes significant spatiotemporal patterning. An analogous perspective is the Fourier domain being a generic basis for which to observe the temporal or spatial patterns, refer to Figure 1.6 and the WAVSVD Chapter 3.1.

The reason the data-driven, tailored basis is preferred is that via the WAVSVD algorithm the bandwidth observed in the wavenumber-frequency domain is expanded.

4.3.4 Ultrasonic C-Scans for Gross Damage Morphology

The dynamic impact causes damage and having a clear understanding of the damage morphology is important. Relating the damage morphology to residual laminate strength is the purpose for conducting this analysis.

The impacted specimens are immersed in water tank, located centrally and perfectly perpendicular to the scan plane (x-y), finally, the laminate is minimally supported along one edge. An immersion Pulse/Echo C-Scan (UTWin UPK-T36) was performed to bound the impact damage zone with that of the healthy surroundings. Having the hardware and software to conduct a scan of this type is not capable without an data organizing system. This immersion system has a dedicated computer, UTWin Software, Pulser/Receiver, MHz level Transducers, Stepper motor that organizes all of this information and produces a couple of graphics of the scanned specimen in near real time.

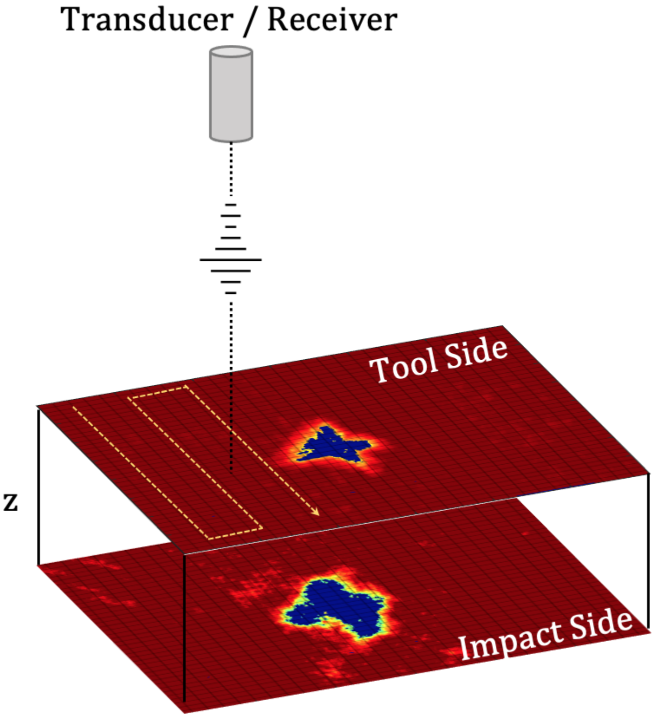

Figure 4.22: A simple schematic of the Pulse/Echo C-scan. The top surface (tool side) is the back surface in perspective of the impact event. The bottom surface is the impact side

A 5MHz transducer to propagate an ultrasonic wave packet to the laminate, Figure 4.22. Four gates are used to pick the peak signal over the range of a gate. The signal has four gates set to capture the through-thickness measurement of the laminate. The gates measure four different time-of-flights (TOF) for a single scan point. So the front, back, through-thickness and partial through-thickness TOFs are all scanned at a given point. The full collection of TOFS will construct an image. the image can be altered to reflect the four TOFs just prior selected. The C-scan data is the TOF history for each point in the immediate vicinity of the damage. This are contains a mix of healthy and damage laminate. A lack of any amplitude implies that zero signal was echoed back. Damage either scattered or allowed for complete passage of the pulsed wavepacket and thus not interrupted by the plate.

Observing Figure 4.22, the transducer/receiver will raster in the x-y plane at a resolution of $0.15mm$. The received signal is then channeled to the data acquisition system for evaluation. Evaluating each scanned point, certain thresholds have to be exceeded in order for the amplitude to be considered. In this research, a 2% threshold was selected to capture all amplitude changes for the top tool and impact surfaces. This means that any signal on the tool and impact surfaces greater than 2% of the reference voltage would trigger the data acquisition system and record the max amplitudes at their respective locations.

Scanning from the tool side towards the impact side allows for a ”shadow” of the damage to be seen. This outline of the TOF deviation from background defines the damage morphology. Perhaps a 10MHz transudcer can be used and obtain a finer through thickness resolution.

4.3.5 Estimating Fracture Toughness

Via Average Stress Through-hole Failure Criteria

Estimation of the Fracture Toughness, K_{IC}, of the laminates in question is possible from the Average Stress Failure Criteria approach. In this research we are using the Through-hole case to extract a characteristic damage size. Estimating the residual strength begins with extracting a characteristic damage length,a_o, from the roots of 4.20 for a Hole. Additionally, knowing the diameter of the hole, failure strength, and ultimate strength of a healthy laminate makes possible the quantification a Fracture Toughness, K_{IC}.

$$K_{IC} = \sigma\sqrt{\pi(a + a_o)} \tag{4.30}$$

Graphically, the residual strength curves from holes and cracks, when framed by the Average Stress Criteria, trend tightly together along a single residual strength curve as shown in (Tan, 2017) and (Daniel et al., 2006). This means that the Average Stress Criteria can relate holes and cracks via the respective case's a_o. The characteristic lengths a_o are not the same value, $a_o^{hole} \neq a_o^{crack}$. However, these characteristic lengths are adjustment terms that align an equivalent crack to a hole for a given residual strength.

The laminates are under plane stress and have varying Fracture Toughness as a result of the amount fiber tows adjacent to the damage. For instance, the OHT specimen with a 3.1mm hole, there were only 3 tows from the edge of the hole to the edge of the plate. Conversely, the 25.4mm hole specimen has 15-18 tow bundles. To address this, it is useful to have experimentally determined Fracture Toughness. Having this will help better correlate the impact case for an equivalent size.

4.4 Results

The results presented are for the impact event, raw data perspectives, wavenumber-frequency spectra, phase velocity, and residual strength.

4.4.1 Impact Event

A suite of impact damage levels are used to study the effects of mechanical parameter degradation. Thus different impact energies are required to achieve this goal. Referencing 4.7, this research aimed to generate Type II damage in the carbon fiber laminate specimens, thus setting an upper limit of allowable kinetic energy at impact. Upon practice, the impact energy levels to achieve Type II in the laminates are 10J, 20J, and 30J, with all energies causing backside fiber breakage but to varying degrees and minimal impact-side denting or discoloration. The 10J impacts generated the truest BVID of the energies. Table 4.1 highlights key metric regarding the impact. Table 4.2 highlights first failure of the laminate and the peak impact force.

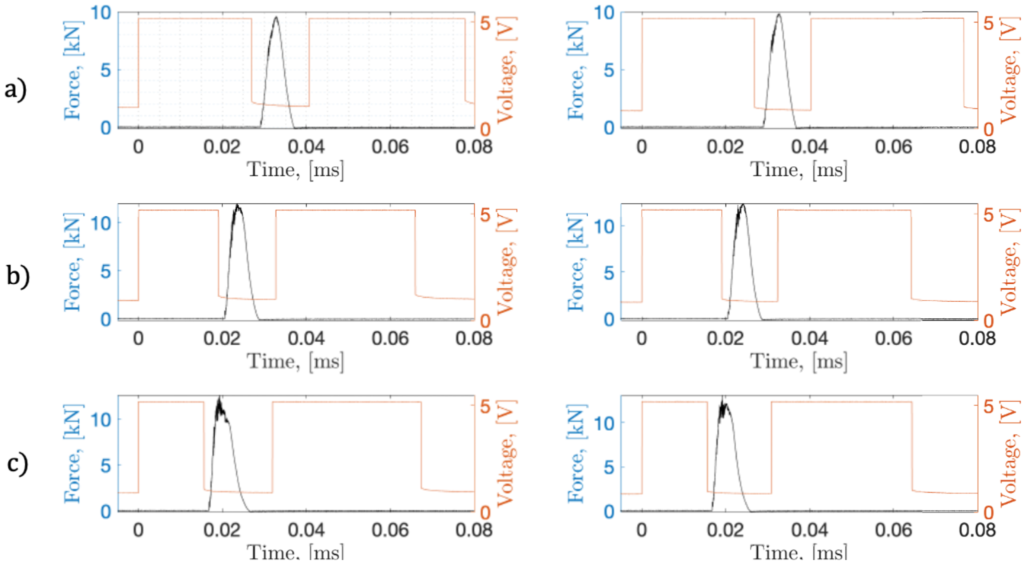

Figure 4.23: Summary of the impact $F(t)$ and incoming and outgoing times, Δt of the pendulum impactor. a) Type II damage, longest impulse at 10J b) Type II damage at 20J and c) Type II damage at 30J, shortest impulse

The incoming and outgoing impactor causes a laser gate to trip as the bar passes by, the interruption times in 4.23 indicating the bar was interrupting the laser.

$$\delta v = \frac{\delta s}{\delta t} \tag{4.31}$$

$$m_{eq} = \frac{1}{3} m_B \frac{L_B^2}{L_N^2} + m_N \tag{4.32}$$

$$KE = \frac{1}{2} m_{eq} v^2 \tag{4.33}$$

The velocity and energy is quickly determined from Equation 4.33 from the interruption times (δt), bar width dimension w, and equivalent mass of pendulum impactor, m_{eq}.

Table 4.1: Summary of Impact Event Dynamics

$\mathbf{KE_{in}}$, [J]	$\mathbf{KE_{out}}$, [J]	$\mathbf{KE_{absorbed}}$, [J]	$\mathbf{v_{in}}$, $[\frac{\mathbf{m}}{\mathbf{s}}]$	$\mathbf{v_{out}}$, $[\frac{\mathbf{m}}{\mathbf{s}}]$	**I**, $[\mathbf{N} * \mathbf{s}]$
10.2	5.4	4.8	2.06	1.49	368.9
10.3	5.6	4.7	2.07	1.52	383.8
20.4	6.7	13.7	2.92	1.67	459.0
20.5	7.3	13.2	2.92	1.74	499.2
30.5	5.9	24.6	3.56	1.57	537.6
30.6	6.7	23.9	3.57	1.66	551.6

As a result of increasing impact energies, the levels of damage caused to the specimen increases as well. Observing Figure 4.24 and comparing row a) with row c), a noticeably chaotic peak region exists for the higher impact energies. Furthermore, in the both impacts at 30J, the $F(t)$ plots show troughs and steps that can be assumed to correlate with the gross backside damage. The 30 J impacts have a signature quadrant failure. See Figure4.25 for better visualization oft the damages.

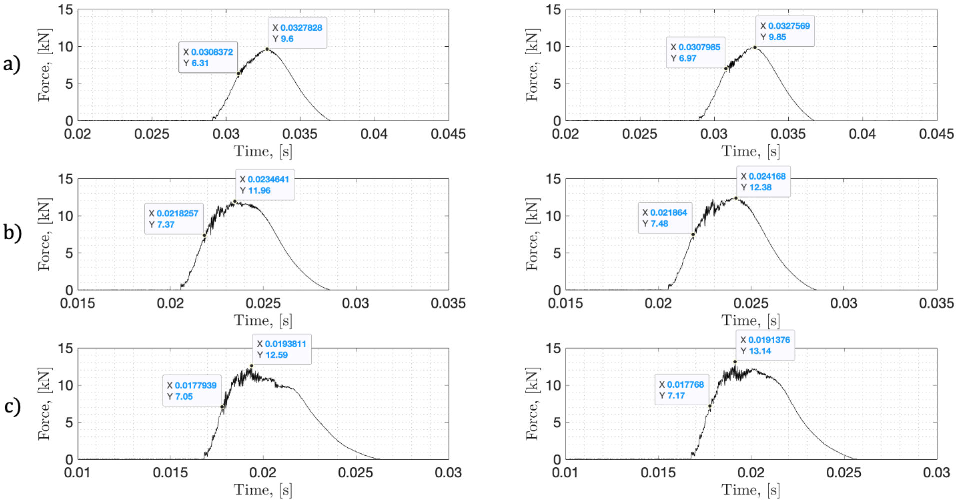

Figure 4.24: Summary of the impact force at first failure and peak force. a) Type II damage at 10J b) Type II damage at 20J and c) Type II damage at 30J. Note that the time axis is shifted to center the impact event

Table 4.2 summarizes the impact forces. Upon observing the impact data, it is apparent that each energy level has introduced a Type II failure which is indicated by $F_{1^{st}Fail}$ and with an average being $7.05 \pm .414\ kN$.

Table 4.2: Summary of Impact Forces

$\mathbf{KE_{in}}$, [J]	$\mathbf{F_{1^{st}Fail}}$, [kN]	$\mathbf{F_{Max}}$, [kN]
10.2	6.31	9.60
10.3	6.97	9.85
20.4	7.37	11.96
20.5	7.48	12.38
30.5	7.05	12.59
30.6	7.17	13.14

The onset of first failure along with increasing peak applied force generated the Types II impact damage that are desired to study mechanical parameter degradation severity via the NDE.

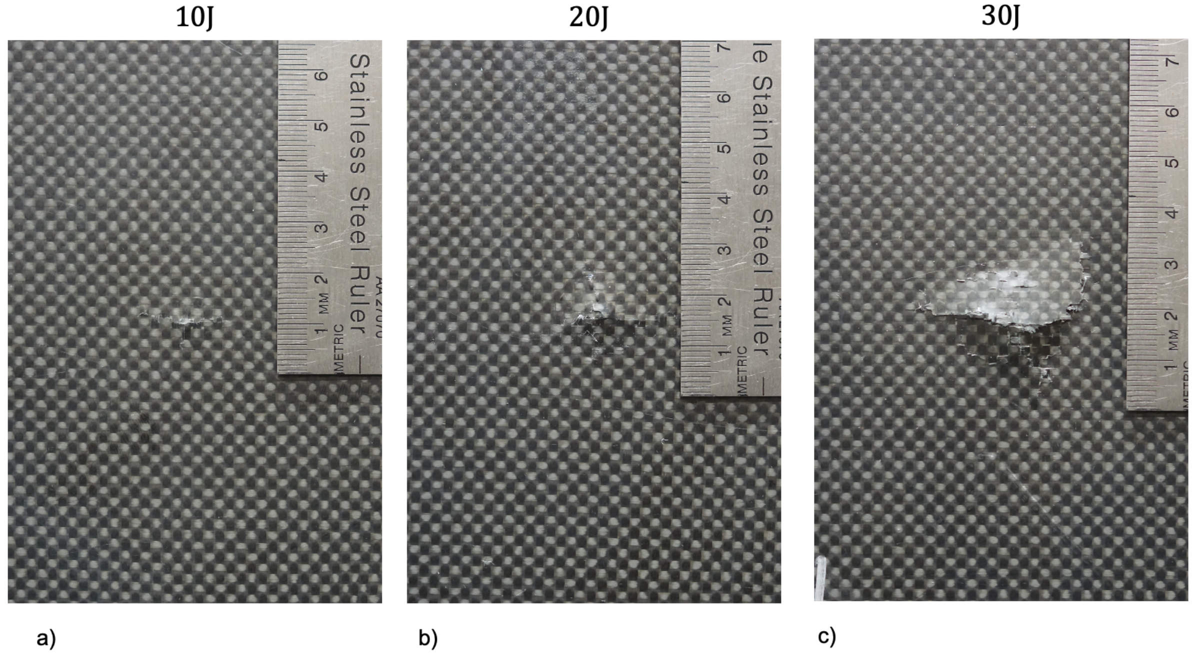

Figure 4.25: Side-by-side comparison of the backside damage generated by 10J, 20J, and 30J impacts. a,b and c) Type II damage is identified with backside fiber breakage but not through cracks or penetration. All of these are BVID if observed from the impact side. The impact side

4.4.2 Damage Quantification via Ultrasonic C-Scan

Utilizing the C-scan hardware, pulse-echo scans the resulting C-Scans indicate a non-symmetric damage region for all impacts. This is most likely attributed to the impactor rotating through a small angle during the impact, stressing one region slightly more than another.

The scan resolution is 0.15mm with the grid overlay at a 2x1mm resolution in the x and y directions, respectively. The z-resolution limits are adjusted for all cases to highlight the attenuation of the received signal relative to their healthy surroundings, highlighting the boundary extent of the damage morphology.

The C-Scans presented, e.g., Figure 4.26 show the max signal amplitude at the given scan point and is scaled by the colorbar. The only post processing that occurred prior to analysis was casting the scan data into a logarithmic perspective.

One of two impact energy sets are presented both as an image and in Table 4.3 and Figure 4.25. The second set of damage extrema results are presented solely in Table 4.3.

10J Impact Specimen C-Scan

The 10J impacts caused damage, which are confirmed visually, as well as with the force-displacement curves measured during impact. The amplitude reduction as a result of damage was localized and required a tight amplitude limit range to identify the damage morphology relative to the surrounding healthy material.

The 10J impact scans of the show clear non-damage symmetry but the extent of damage are the the most symmetric in terms at max extrema. The extrema of damage indicated in Figure 4.26 are taken at the outermost points of damage in the warp and fill directions. The extent of damage is 9.7mm in the warp direction, while 9.9mm in the fill direction. For any future tensile loadings, the load is applied parallel to the Warp direction.

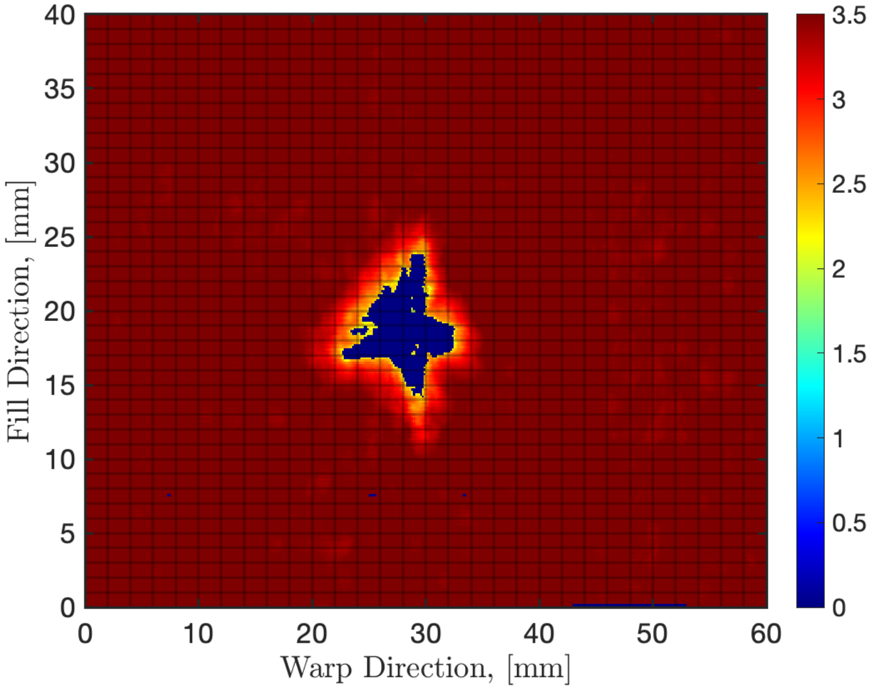

Figure 4.26: C-Scan of 10J impact specimen from the tool-side surface. From the perspective of the impactor, this is the backside. From the perspective of the ultrasonic transducer, this is the front surface

Measuring the amplitude attenuation as a result of damage from the back wall, which casts a shadow of damage when measured at the transducer, the extent of damage is $13.3mm$ in the warp direction, while $15.3mm$ in the fill direction.

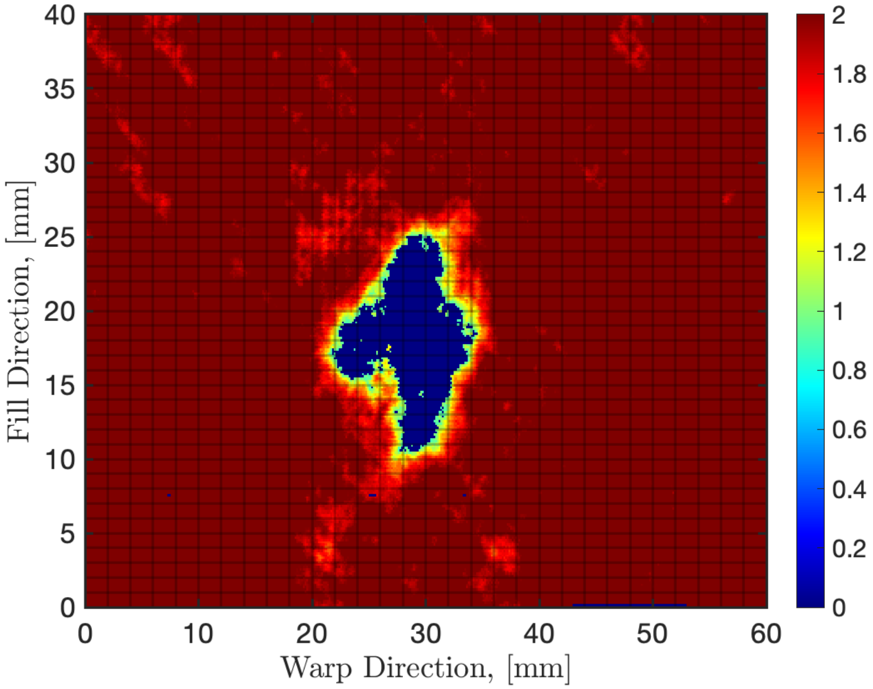

Figure 4.27: C-Scan of 10J impact specimen from the release fabric surface. From the perspective of the impactor, this is the impact side. From the perspective of the ultrasonic transducer this is the back surface

The difference between the front and back scans is $3.4mm$ and $5.6mm$ in the warp and fill direction, respectively. This indicates the sensitivity of the C-Scans to damage severity when measuring front and back surfaces.

For the 10J impact, the predominant failures occurred the warp-fill directions, which are in the same direction as the 0^o and 90^o fiber tows. A single damage direction is also along the $\pm 45^o$ fiber tows, pointing towards the upper left corner of Figure 4.26.

20J Impact Specimen C-Scan The 20J impact scans are the the most symmetric of the damages with clear fracture in the warp and fill directions with a central circular damage, see Figure 4.28. The extrema of damage indicated in Figure 4.28 are taken at the outermost points of damage in the warp and fill directions. The extent of damage is 18.2mm in the warp direction, while 27.1mm in the fill direction.

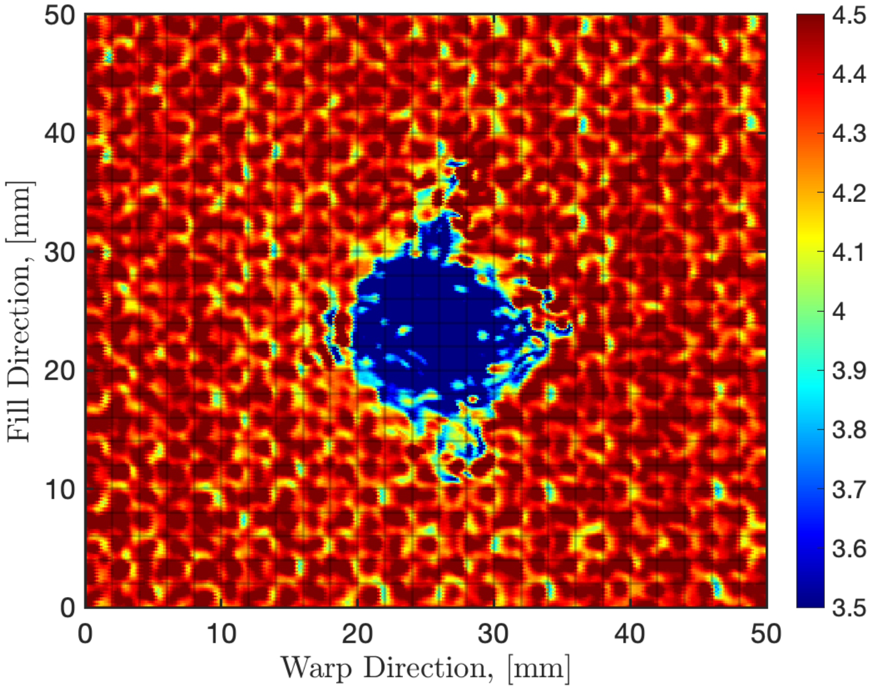

Figure 4.28: C-Scan of 20J impact specimen from the tool-side surface. From the perspective of the impactor, this is the backside. From the perspective of the ultrasonic transducer this is the front surface

Converesly, lookng at Figure 4.29, which is the measuring the TOF at the backwall (impact side), the impact damage is hexaganol-like and indicative of a broader damage region.

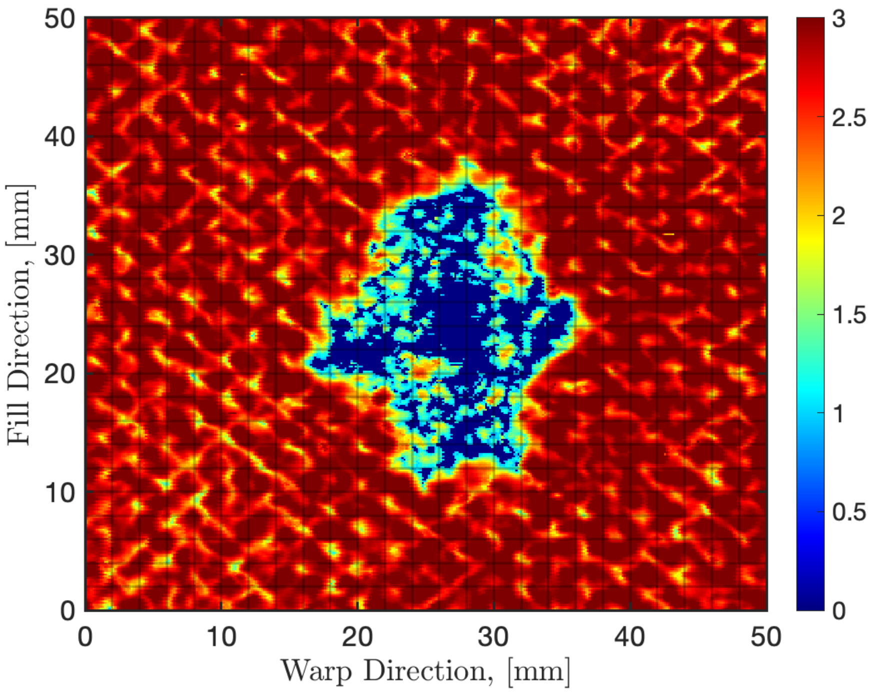

Figure 4.29: C-Scan of 20J impact specimen from the release fabric surface. From the perspective of the impactor, this is the front surface. From the perspective of the ultrasonic transducer, this is the back surface

The hexaganol-like extrema of Figure 4.29 are taken similar to Figure 4.28. The extent of damage is $20.4mm$ in the warp direction, while $27.9mm$ in the fill direction.

The difference between the front and back scans are $2.2mm$ and $.8mm$ in the warp and fill direction, respectively.

For the 20J impact, failure boundaries occurred along all ply orientation angles and along fiber tows. Figure 4.29 indicates that the pentagonal shape is pointed along the fill direction, while the points in the midsection of the pentagon are oriented along the warp direction. The lower points of the pentagon are peaked and indicate an influence of $\pm 45^o$ fiber tows constraining the propagation of damage.

30J Impact Specimen C-Scan The 30J impact scans indicate the transition from healthy TOF to damaged TOF follows the ply angles with the damage perimeter following different tow bundles, Figure 4.30. The extrema of damage indicated in Figure 4.30 are taken at the outermost points of damage in the warp and fill directions. The extent of damage in the warp direction is $27.4mm$, while $33.8mm$ in the fill direction.

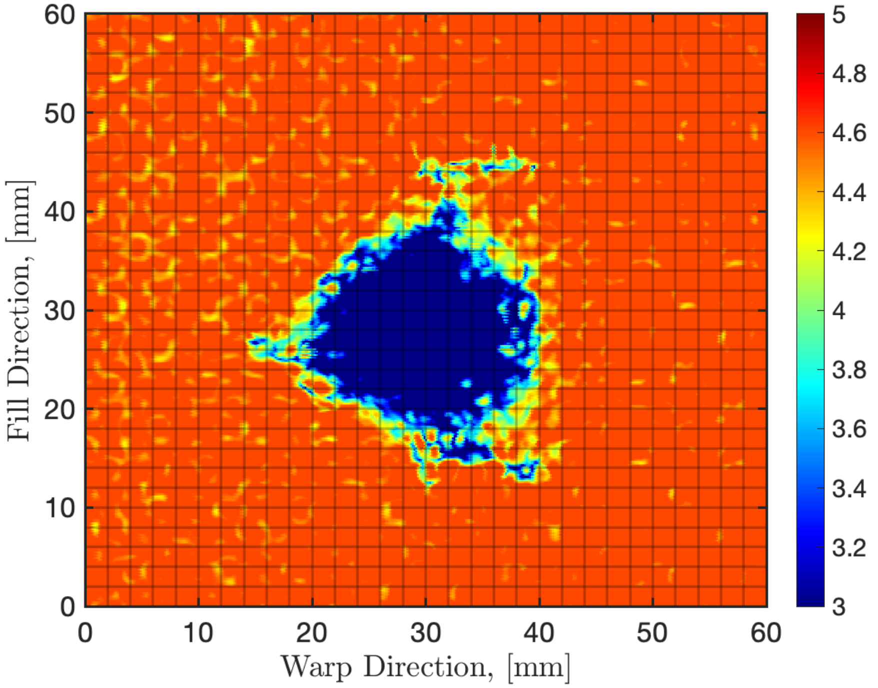

Figure 4.30: C-Scan of 30J impact specimen from the tool-side surface. From the perspective of the impactor, this is the backside. From the perspective of the ultrasonic transducer this is the front surface

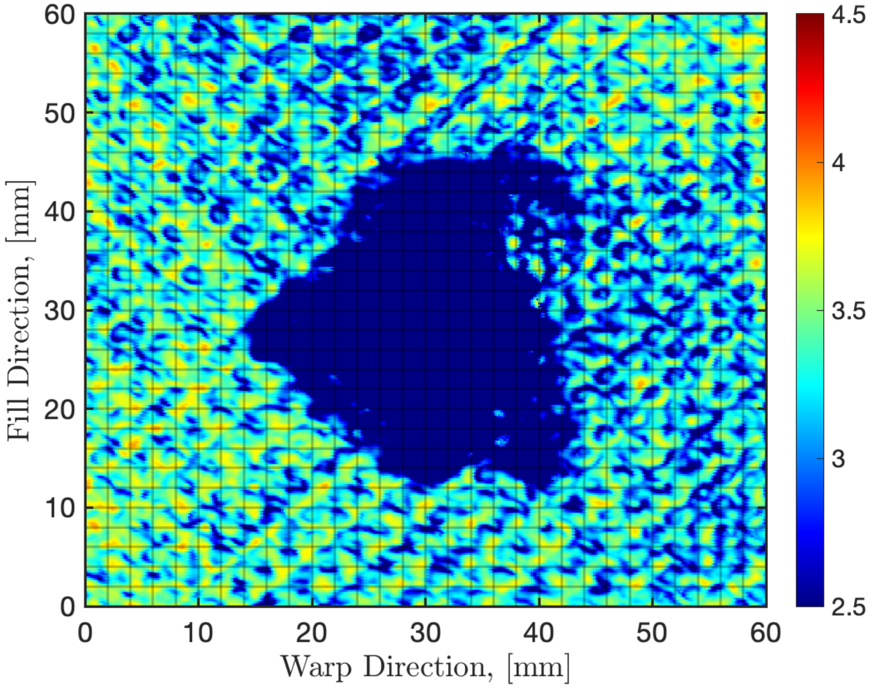

Figure 4.31: C-Scan of 30J impact specimen from the release fabric surface. From the perspective of the impactor, this is the front surface. From the perspective of the ultrasonic transducer, this is the back surface

For the 30J impact, the predominant failures occurred the warp-fill directions, which are in the same direction as the0^o and 90^o fiber tows. The orientation of the pentagonal shape is directed along the Warp direction and bounded by the $\pm45^o$ tows. The damage zone along the $\pm45^o$ terminates and converts to a damage line traveling along the $0^o/90^o$ tows. Figure 4.31 highlights the pentagonal shape pointing to the LHS of the figure.

General Observations Observing the damage for all specimens and abstracting to what might be considered an ”ideal damage morphology”, the general morphology is a pentagon with various rotation angles from the warp-fill (x-y) orientation. This is likely due to the quasi-like orthotropic nature of the laminate. It is possible to idealize the damage morphology and study the stress concentration around the damage as during loading.

Table 4.3: Impact energy and respective damage extrema in the Warp and Fill directions. Recall that tensile loading will be normal to the Fill direction.

ID, I_n	KE_{in}, J	$Warp, mm$	$Fill, mm$	$Test Width, mm$	$\frac{Width}{Fill}$
I_1	10.2	10.9	16.4	65.6	4
I_2	10.3	13.3	16.3	65.2	4
I_3	20.4	32.6	26.7	106.8	4
I_4	20.5	20.4	27.9	106.8	3.82
I_5	30.6	35.6	33.3	127.0	3.8
I_6	30.6	30.2	31.2	127.0	4.1

Maintaining destructive testing with consideration of fiber tow effects, the impact strength test are also best kept to width-to-damage ratio of 4:1.

4.4.3 Accentuation of Symmetric and Anti-Symmetric Modes, Raw Data

The WAVSVD initiates on the spatiotemporal data collected via the SISDO scan method. The data consists of all observations in the test domain: 0-259mm and 0-.500ms. As a result of the exciting energy imparted to the plate via the mini-impactor and converted into propagating energy and refracting into different Lamb modes, the spatiotemporal data is best observed with two different limits, see Figure 4.32.

The limits are on the magnitude of the Lamb mode in question. Antisymmetric can have large amplitudes do to the out-of-plane flexure of the plate as the UGW goes by. The symmetric modes are less energetic in this perspective because the out-of-plane motion is less with these Lamb modes, making them difficult to detect when occulded by their more energtic counterpart. The antisymmetric Zone hightlights all large amplitude antisymmetric waves that may be present. The Symmetric Zone captures the more subtle Symmetric modes that precedes antisymmetric first arrival.

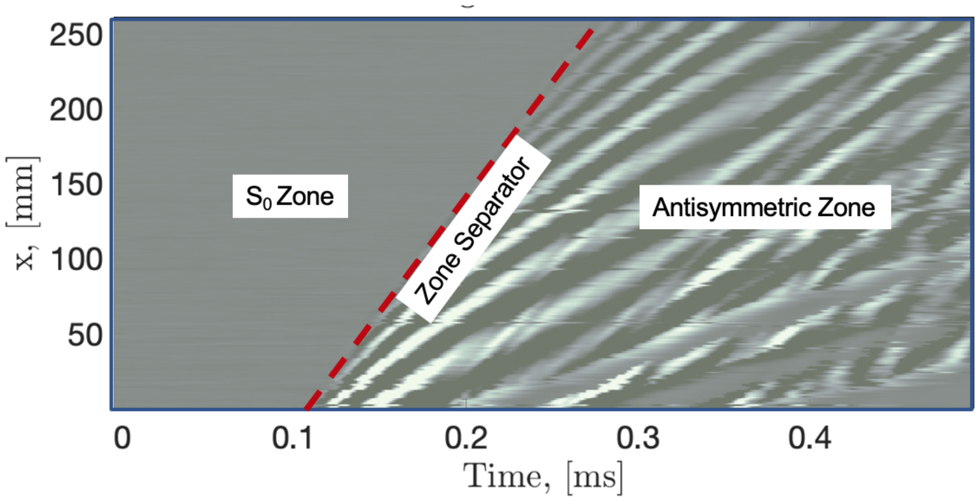

Figure 4.32: Example of separating a data set into two zones

Observing the mode-accentuated spatiotemporal data highlights features directly obvious from raw data. The logical place to begin is with the baseline, healthy, data. This serves as ground truth and is shown in Figure 4.33. What is observed in the A_0 accentuated region is propagation of A_0 mode along with additional antisymmetric modes. For transparency, the slack in the LST is apparent at approximately 60mm and 190mm. This does not compromise the analysis and will not be mentioned further.

The S_0 region is accentuated in the bottom of Figure 4.33 and shows no discernible symmetric Lamb mode propagating in space nor time. This region, for this case, is considered to be noisy as no waves have arrived prior to the A_0 wave front. This is a critical counterpoint to specimens that have a through-hole or impact site because they do exhibit S_0 mode conversion.

The A_0 region is accentuated in the top of Figure 4.33 and shows significant antisymmetric Lamb mode propagating in space and time. The majority of the information that reveals itself, is the A_0 Lamb mode and is demarked by the "zone separator" in Figure 4.32. Observing two Figures, it is difficult to discern any differences that may exist as a result of damage and really drives the need for zones to exhaustively search for modes.

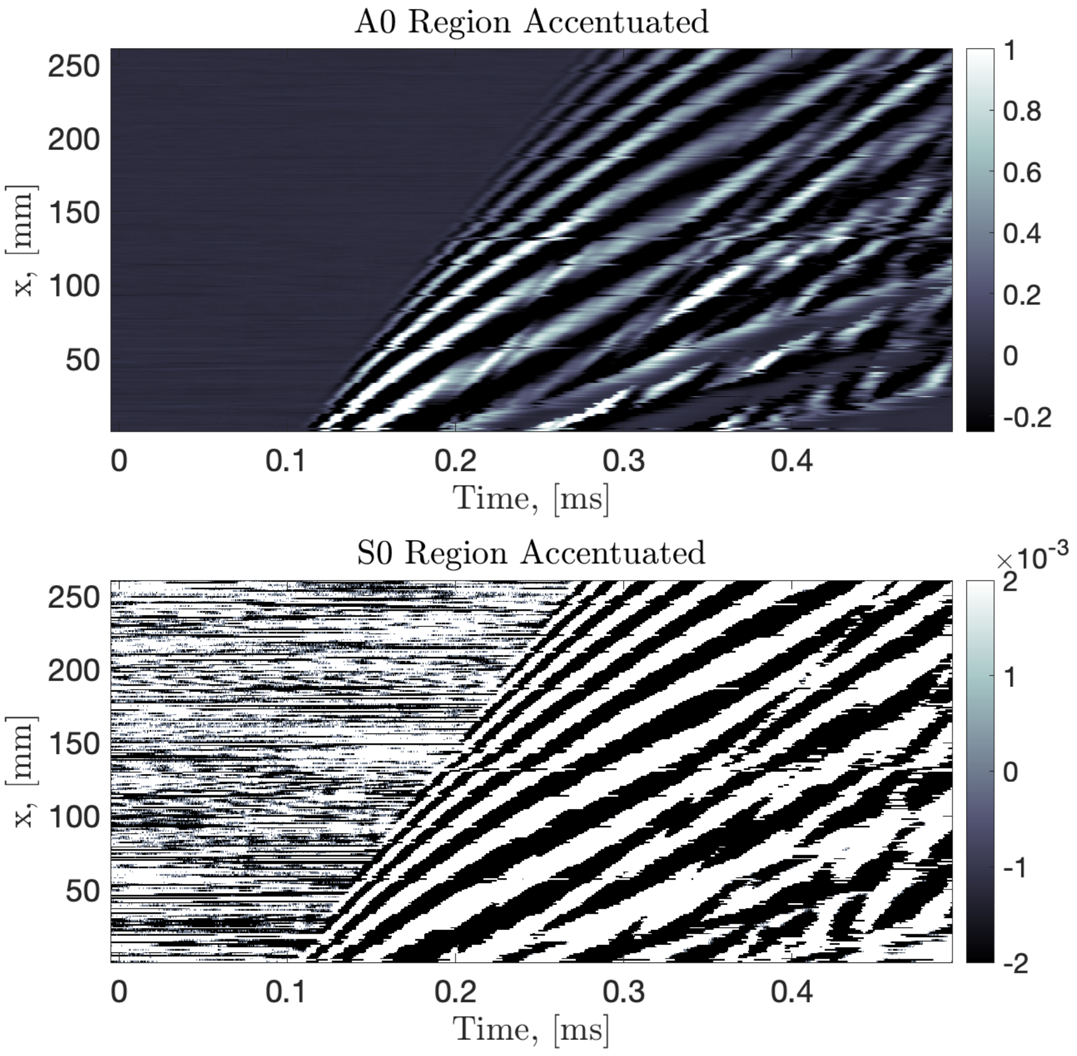

Figure 4.33: Baseline Healthy Laminate with S_0 and A_0 zones accentuated

10J Impact

The CFRP baseline versus 10J impact spatiotemporal datasets are observed. In Figures,4.33 and 4.34. This is a prime case where casting the space-time data in the frequency domain to reveal any pattern development.

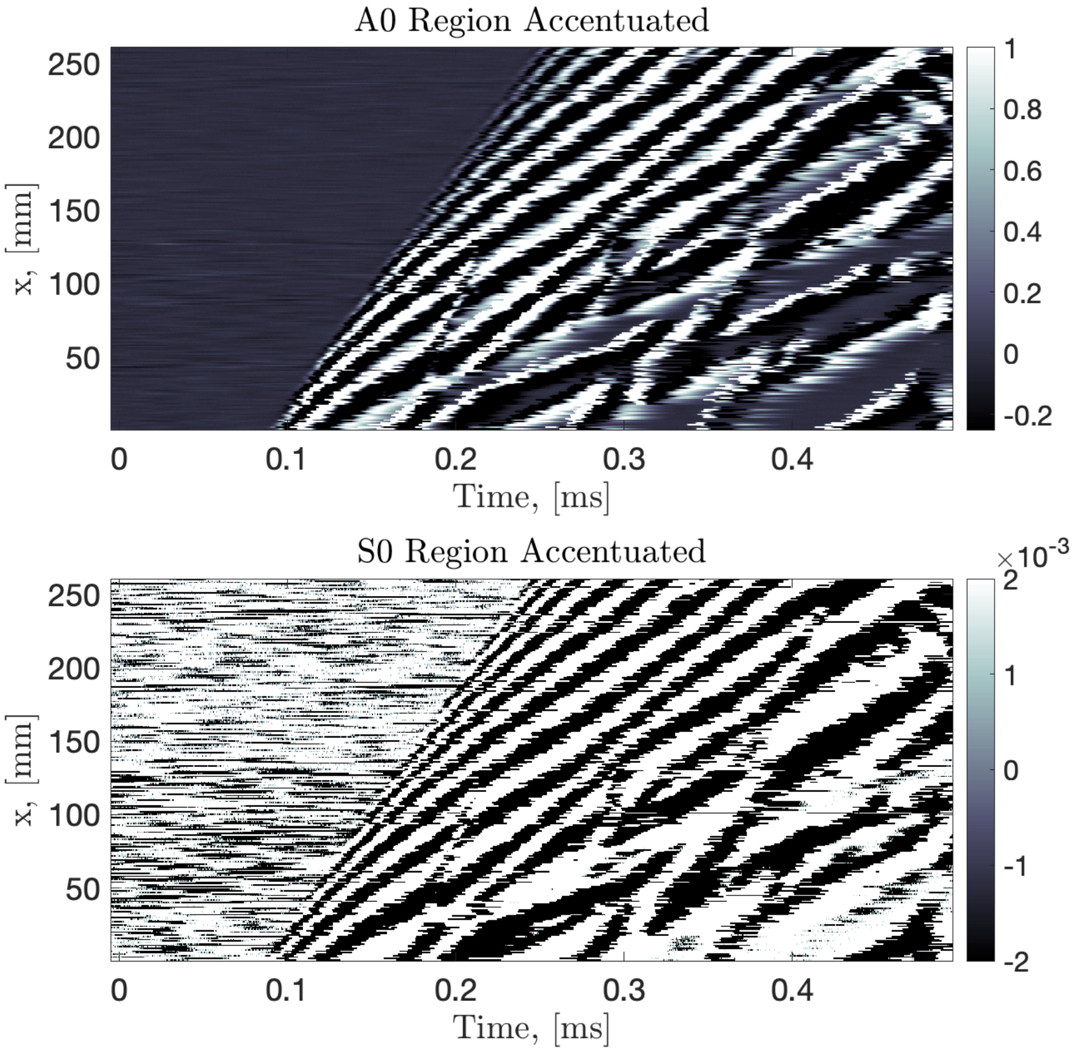

Figure 4.34: 10J impact energy with BATs at 13^o. Note that the only difference in the reflections propagating at later times and have no effect of this analysis

20J Impact

The appearance of an S_0 mode is seen in the 20J case, see bottom of Figure 4.35. This was first observed during experimentation and prompted the limits to be developed so that the data can be observed in two perspectives. The interesting thing about the mode conversion is that post-damage, the A_0 mode becomes attenuated, see top of Figure 4.35. A small shift also occurs as the UGW have to navigate the damage. These two subtle departures from nominal begins at x = 130mm.

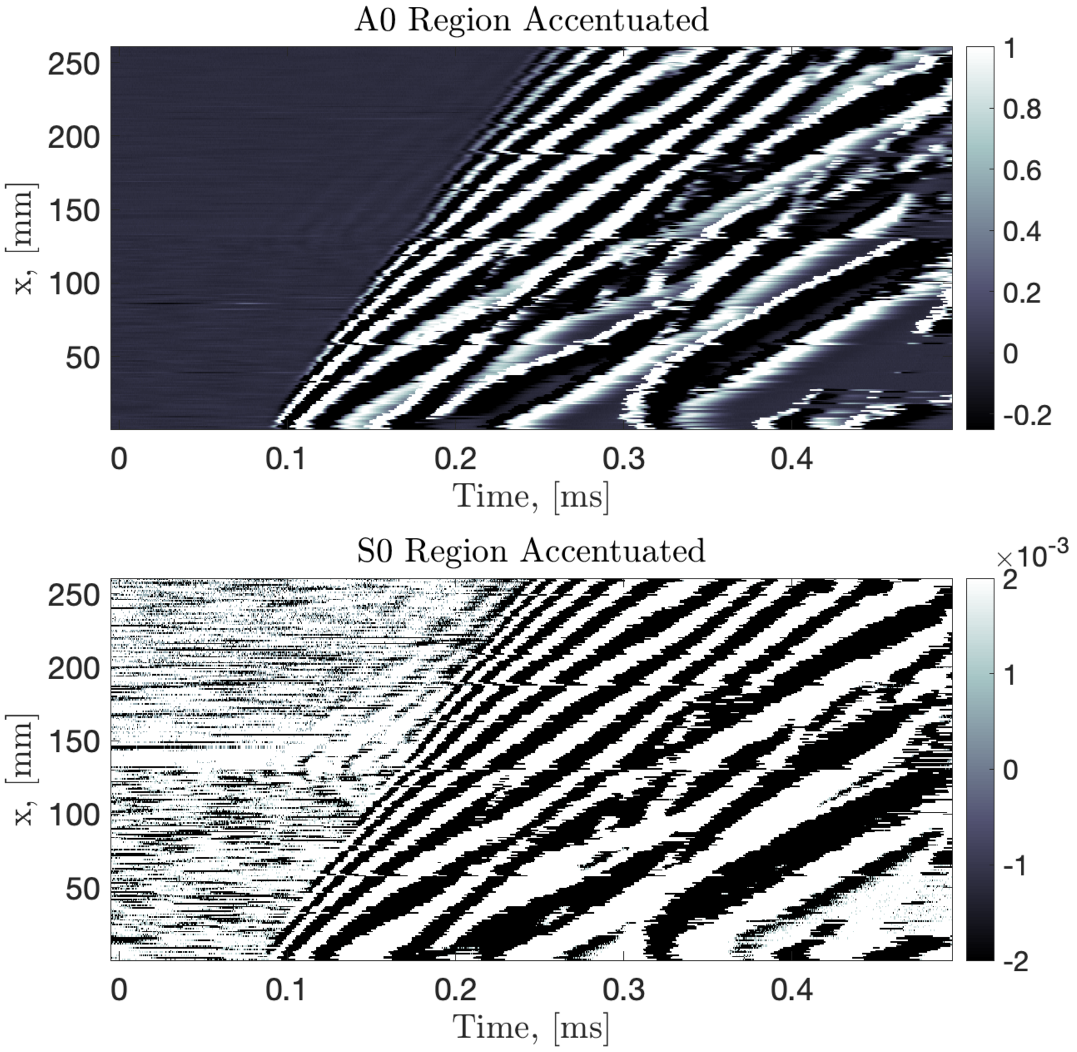

Figure 4.35: 20J impact energy with BATs at 13^o. Observe the S_0 mode conversion at approximately x(130) and clearly highlighted in the S_0 zone graph

30J Impact

Observing the 30J impact spatiotemporal accentuated data, Figure 4.36, the increased impact energy generates a stronger mode conversion for the S_0 viewpoint.

With careful inspection the S_0 mode was energetic enough to appear in the A_0 accentuation at the top of 4.36.

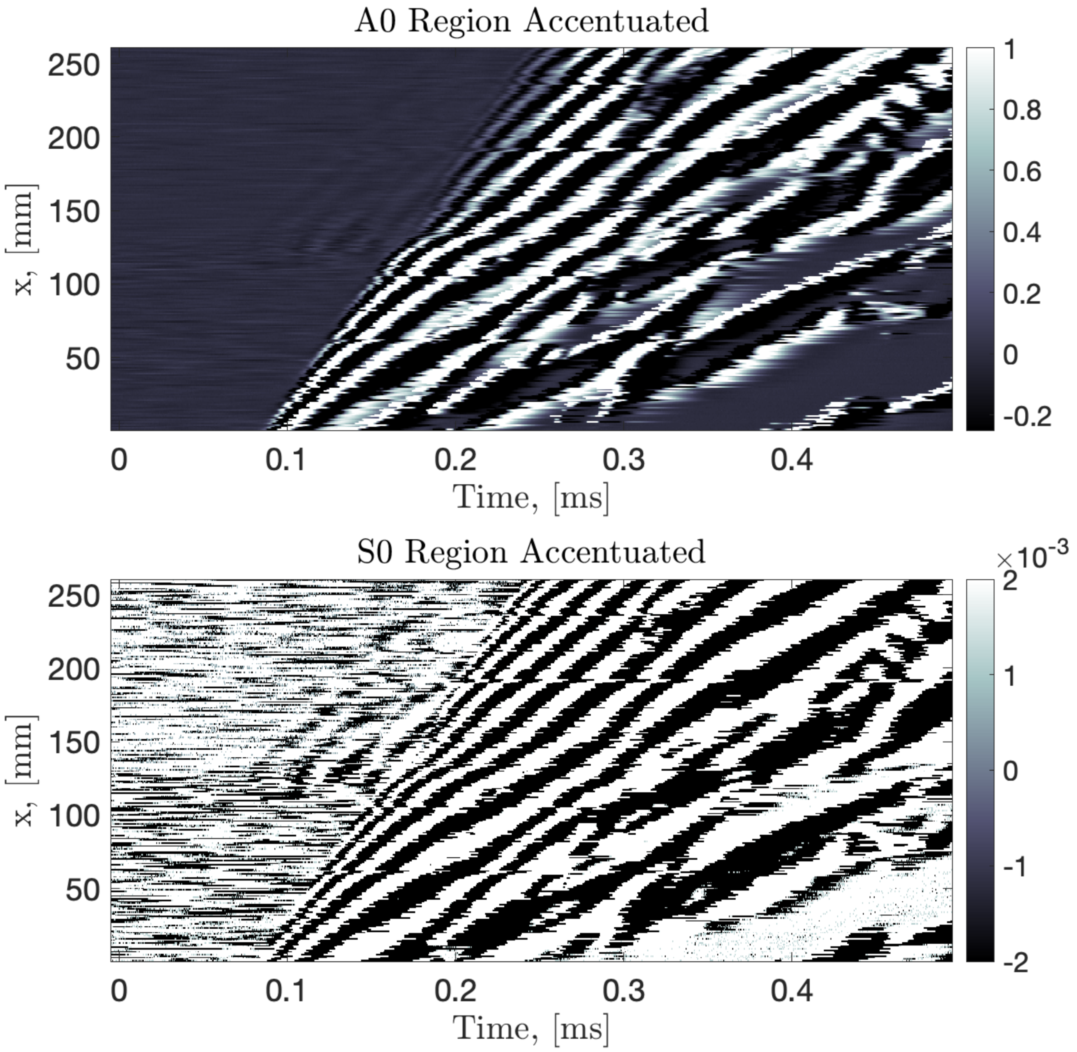

Figure 4.36: 30J impact energy with BATs at 13^o

After interrogating the impacted specimens, four major features are apparent as a result of impact damage and build upon the observations from Section 4.4.3.

1. S_0 mode appears in space prior to the known impact location
2. Shadowing of the first arrival of the A_0 mode occurs at and after the impact location
3. A shift in A_0 mode as a result of damage
4. the first arrival of the A_0 modes can be used to effectively window the data set

It is possible that these Lamb mode conversions are scatter/reflections and any future work should investigate this.

4.4.4 Phase Velocities of Baseline, Open-hole, and Impact Specimens

Progressing from the spatiotemporal data into the spectral domain to estimate phase velocities of healthy, through-hole, and impacted specimens, a series of steps haveto take place, this is the WAVSVD algorithm and the majority of the data within the algorithm could be useful but isnt explored. Only present are the phase is presented next. To do so, the WAVSVD algorithm has been used to reveal the phase velocity dispersion relations. The phase velocity analytic solution comes from lamina level testing historical data and an open source MATLAB program called DispersionCalculator. The analytic and experimental data are in strong agreement and will presented on all phase velocity dispersion diagrams. Be aware that they are constant from one figure to the next.

Phase Velocities of Open-hole Specimens

The challenge presented with an Open-hole is the strong acoustic impedance mismatch between the air and the void in the laminate. This stark material moduli difference, along with the UGW assumptions, this prevents any significant UGW from propagating through the void and re-entering the laminate on the opposite side at an amplitude as if the UGW never passed through air. An equivalent perspective being the material properties in the volume of the hole are essentially zero relative to the laminate.

Despite this extreme difference of material properties along the scan direction, this hole serves as a scatterer of propagating energy. Experimentation indicates a hole will shrink the bandwidth in the wavenumber-frequency domain and thus in phase velocity domain, as well.

3mm Hole The WAVSVD phase velocity dispersion estimate of a 3mm hole indicates an attenuation of phase velocity and frequency. Figure 4.37 highlights this attenuation of phase velocity content relative to the baseline state. Quantitatively, this is a content decrease of 24%.

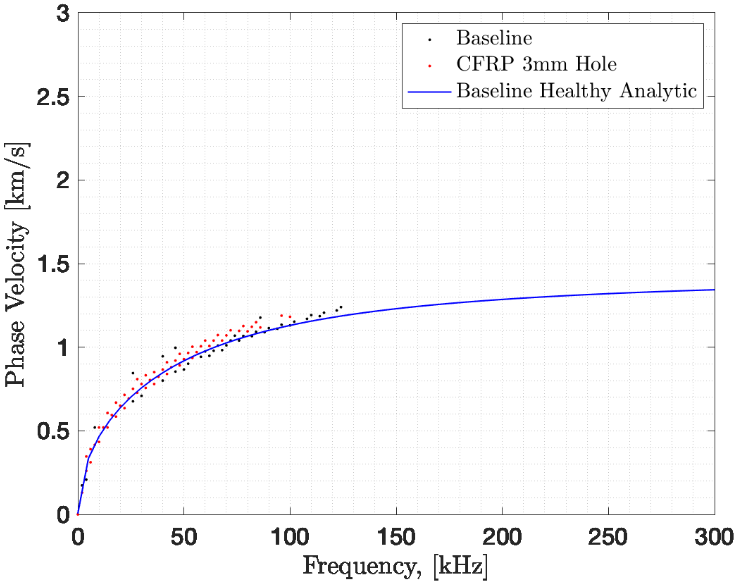

Figure 4.37: Phase velocities from the baseline, healthy, scan overlaid with the phase velocity of laminate wth a 3mm through hole and the analytic solution for a healthy specimen

6.35mm Hole The suggested phase velocity estimate for the 6.35mm, Figure 4.38 hole has a noticeable upward shift starting at 30kHz. There is a mixture of phase velocity content that propagates along the analytic solution and a proportion that is translated vertically, indicating a sudden increase in shear stiffness within the hole. This does not make sense physically and this translation is attributed to experimental error. The error most likely came in the form of a misalignment the specimen as the experiments was being conducted.

The experimental phase velocity data for the 6.35mm case shows the signal attenuating from 125 kHz to 83kHz, or 33.6%.

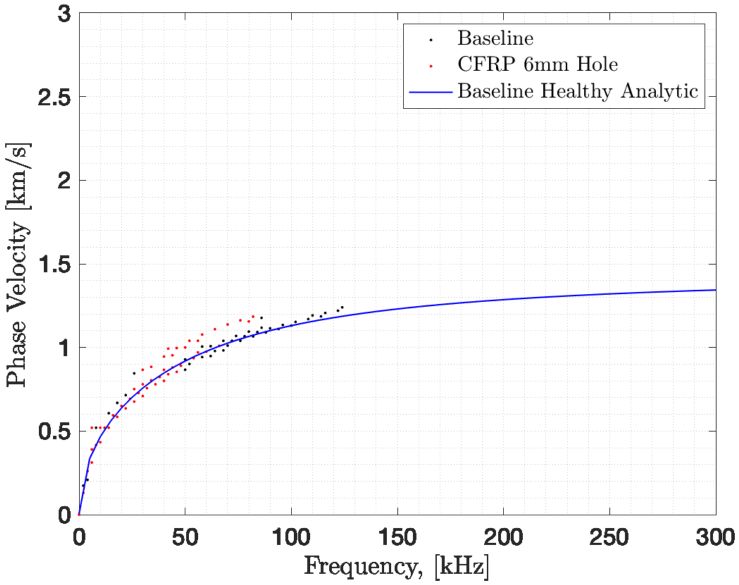

Figure 4.38: Phase velocities from the baseline, healthy, scan overlaid with the phase velocity of laminate wth a 6.35mm through hole and the analytic solution for a healthy specimen

12.7mm Hole For the 12.7mm diameter hole, the attenuated signal exhibits less attenuation than its smaller diameter neighbor. The attenuation in phase velocity content is only 16%. A possible explanation is the misalignment of the MI-sensor-hole in space.

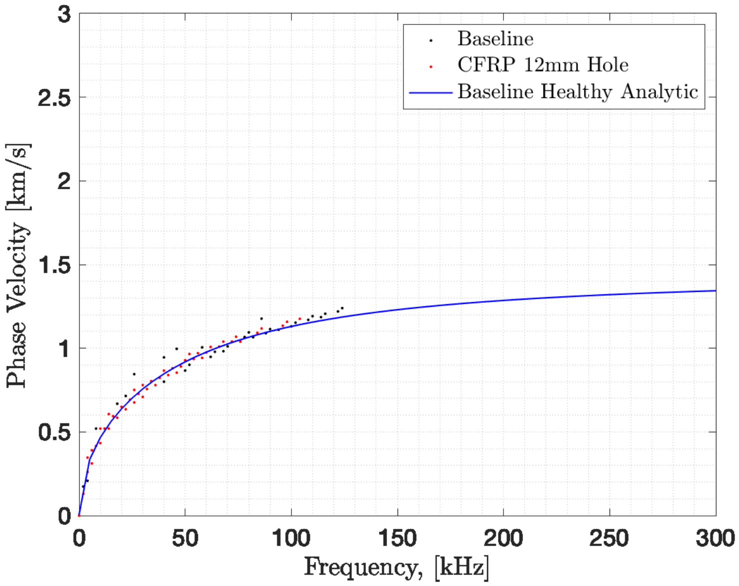

Figure 4.39: Phase velocities from the baseline, healthy, scan overlaid with the phase velocity of laminate wth a 12.7mm through hole and the analytic solution for a healthy specimen

25.4mm Hole Catching backup with the increasing attenuation trend, the 25.4mm diameter hole specimen exhibited a phase velocity content attenuation of 40%. With none of the data deviating signficantly from the healthy analytic solution.

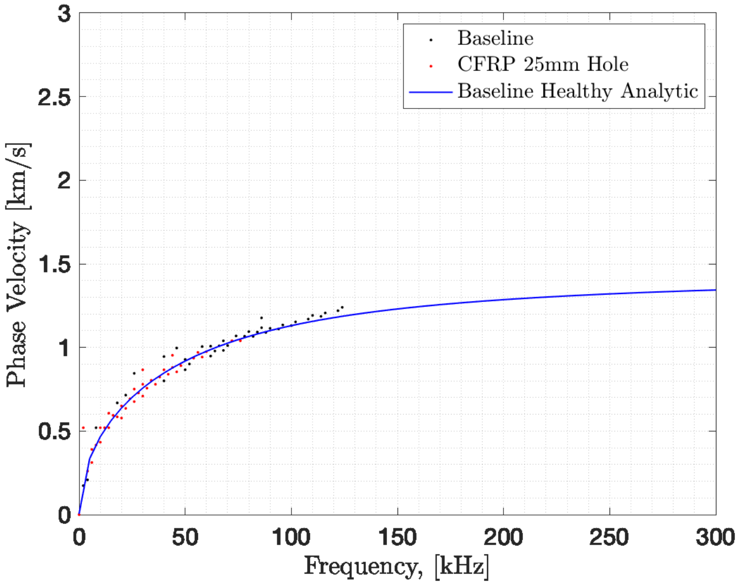

Figure 4.40: Phase velocities from the baseline, healthy, scan overlaid with the phase velocity of laminate wth a 25.4mm through hole and the analytic solution for a healthy specimen

An overall trend emerges about the behavior of phase velocity in the presence of ever increasing hole sizes. The trend is that the max frequency seen will become less and less as the hole size increases. This makes sense, as hole size (or damage size) increases, the sound waves above a certain frequency are scattered.

Phase Velocities of Impacted Specimens

The impacted specimens are generally the same size as the Through-holes, but do tend to be on the larger end of the damage size axis. This is convenient for use of Average Stress approximated Fracture Toughness. Besides this, visual inspecting Figures 4.34,4.35, and 4.36, striking features developed that are potentially indication of material degradation. The apparent reallocation of signal to a damaged value is observed all the while the attenuation is being exhibited along the healthy curve. The line scan through the impact zone reinforces this concept of impacts being a mixture of material degradation and cracks. There is a lot to unpack in this version of the data and by no means has the mining of this data been exhaustive and leaves one with questions line ”perhaps the damaged experimental phase velocity estimate has applicability to cracks?” and ”what is the relationship of impact energy and reallocation of phase velocity’s healthy energy to damaged energy.

10J with BATs at 13° The phase velocity estimates from the WAVSVD algorithm of the impacted 10J specimen are encouraging and follow the initial hypothesis of observing a downward shift in the phase velocity diagram. The downawrd shift equates to approxiamtely a 60% decimation of the material moduli with some minor tweeks (not an optimizable process in this case) to align the analytic with damaged data points.

For this 10J impact, which is 16.1mm in total damage length normal to the loading direction, has an attenuation of 25% and is determined from the **Max Damaged Experimental**. The appearance of the second phase velocity estimate and the analytic fit to it is also a brute force approach. Only four data points exist along the damaged phase velocity, but as the impact energy grows, so does the data that falls on the damaged analytic solution.

Notice that the majority of the damage is attributed to Material Degradation.

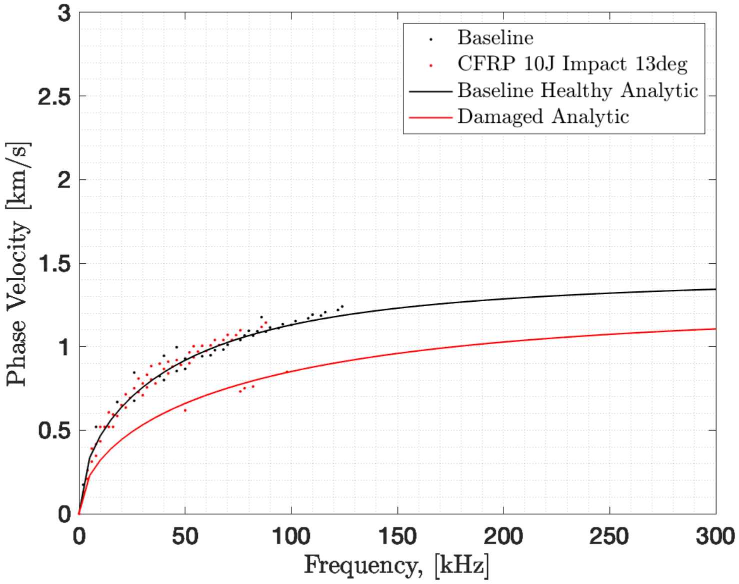

Figure 4.41: Phase velocities from the baseline scan overlaid with the phase velocity of a laminate with a 10J impact energy, and the analytic solutions for both healthy and degraded states. Note that the max attenuated phase velocity and frequency are taken from the damaged red data/analytic

20J with BATs at 13° In congruence with the hypothesis their is a degraded phase velocity dispersion information embedded within the spatiotemporal data, however, relative to the the 10J case the damaged phase velocity experimental data points are along the same damaged dispersion curve. This is curious as it is incongruent with the hypothesis, where at inceasing impact energies, the greater the degradation.

The attenuation exhibited for the 20J case is 23% with a max observed damaged content being at 97kHz.

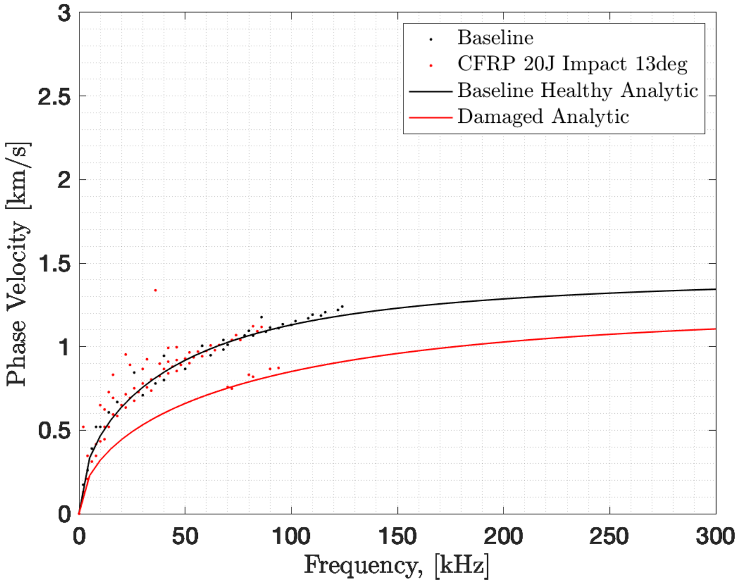

Figure 4.42: Phase velocities from the baseline scan overlaid with the phase velocity of a laminate with a 20J impact energy, and the analytic solutions for both healthy and degraded states

The amount of energy that is transferred in the impact process to generate damage seems to be linked to the conversion of damaged, but along the healthy analytic curve, to damaged and is along the damaged curve.

30J with BATs at 13° The 30J impacts causes significant damage and is the largest of all damages between the through-holes and the impact specimens. The impact caused the an increased shift of energy from the healthy to damaged and is attenuated at 83kHz. Interesting to note that in the low frequency range, <50kHz, the damaged estimate has increased scatter. This is also reflected in the 20J cases as well.

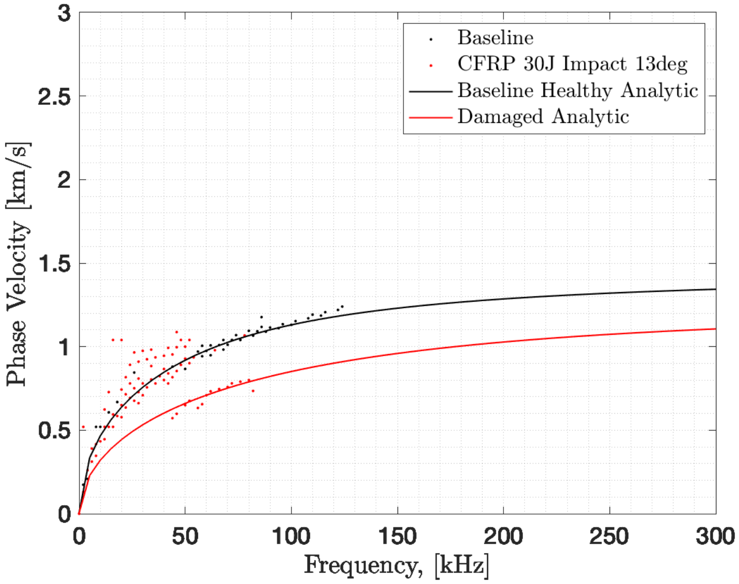

Figure 4.43: Phase velocities from the baseline scan overlaid with the phase velocity of a laminate with a 30J impact energy, and the analytic solutions for both healthy and degraded states

The initial hypothesis was that as the impact energy increases the damaged phase velocity would decimation would also increase (in some incremental fashion), instead the reallocated data is for all energy levels is constant. So some damage threshold was breached and is now considered the damage floor. The increasing amounts of data that gets reallocated to the damage dispersion curve as the impact energy increases was also unexpected.

4.4.5 Destructive Evaluations

Tension tests were performed on the Open-hole, Impacted specimen, and Healthy Specimens.

Open-Hole Tension

Open-hole tension, in congruence with ASTM 5776, are presented. The goal of OHT was to obtain the residual strength of the laminate as a function of the hole radius. Two methods were implemented to observe the strain development as a result of the incremental displacement applied to the clamped specimen.

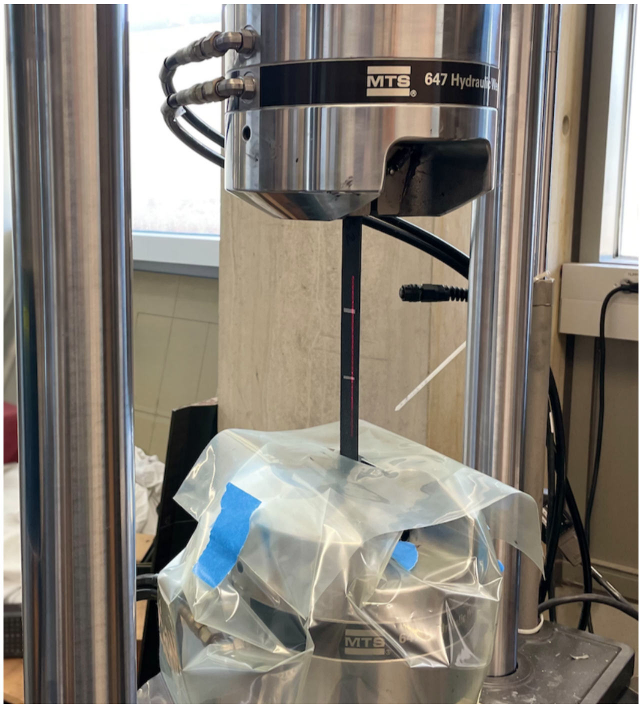

Figure 4.44: The baseline healthy specimen inserted in the MTS apparatus with visible reflective tape to capture the laser extensometer. The red line is located on the CFRP specimen

The laser extensometer serves as ground truth for the mean strain across the span of the reflective tape, which is 80mm. The experiments were conducted with Digital Image Correlation (DIC) as well. Having the full-field strains gives a richer version of the time history of strain development within the plate.

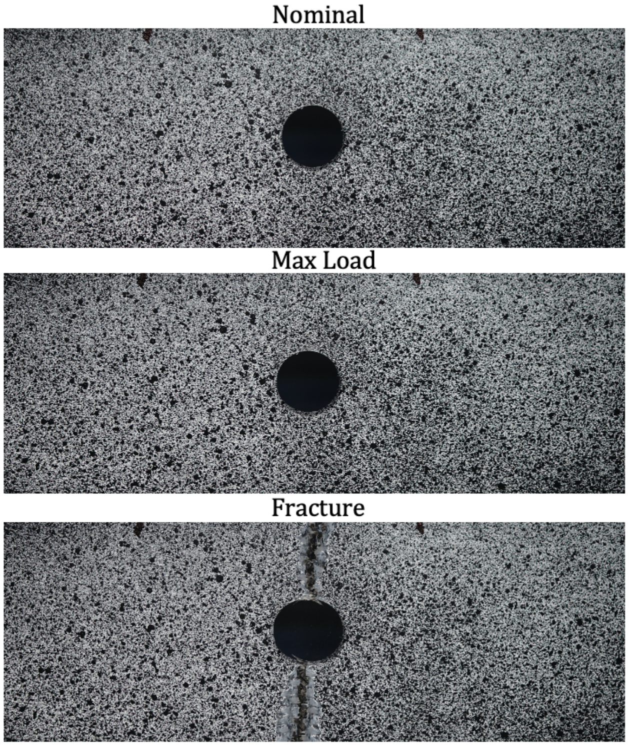

Figure 4.45: The top to bottom sequence is at rest, max stress, and post-fracture event

Stress-Strain The OHT stress and strain are experimentally determined and are graphically summarized in FIgure 4.46. Six baseline specimens were used to develop a mean baseline healthy strength. The general trend is that as the hole diameter increases, while keeping the width of the plate to the diameter of the hole, 4:1, the strength is reduced to lower levels as the size of hole increases.

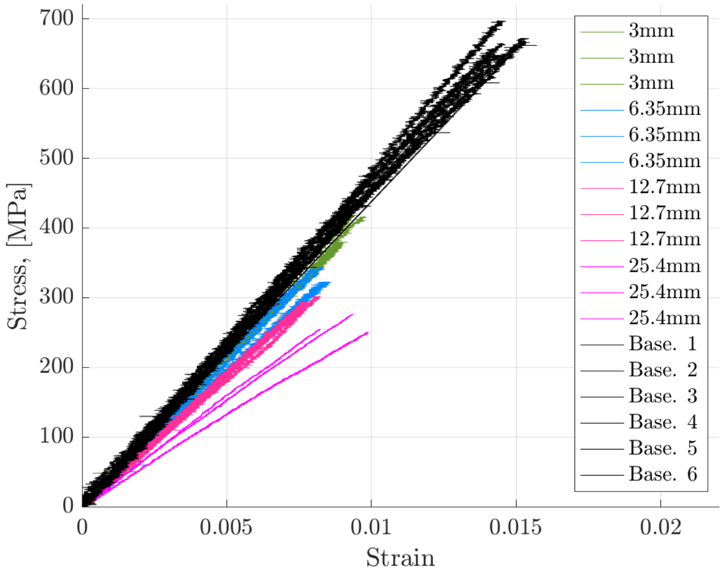

Figure 4.46: Stress-Strain for CFRP OHT Specimens. The strain is measured as the average strain across the span of the extensometer, this is also confirmed with DIC but not shown

Residual Strength OHT The residual strength of the OHT specimens are normalized by the mean healthy strength and are plotted with 95% confidence bounds. The variability in the dataat 1.5mm radius is likely attributed to misalignement of hole to specimen center. This can cause an imbalance in supporting tows.

Regardless, the residual strengths quickly drop off from a max value of 1 to 60% of the original strength with only a 3.1mm diameter hole. The curve bottoms out at .35 (bottom of confidence prediction).

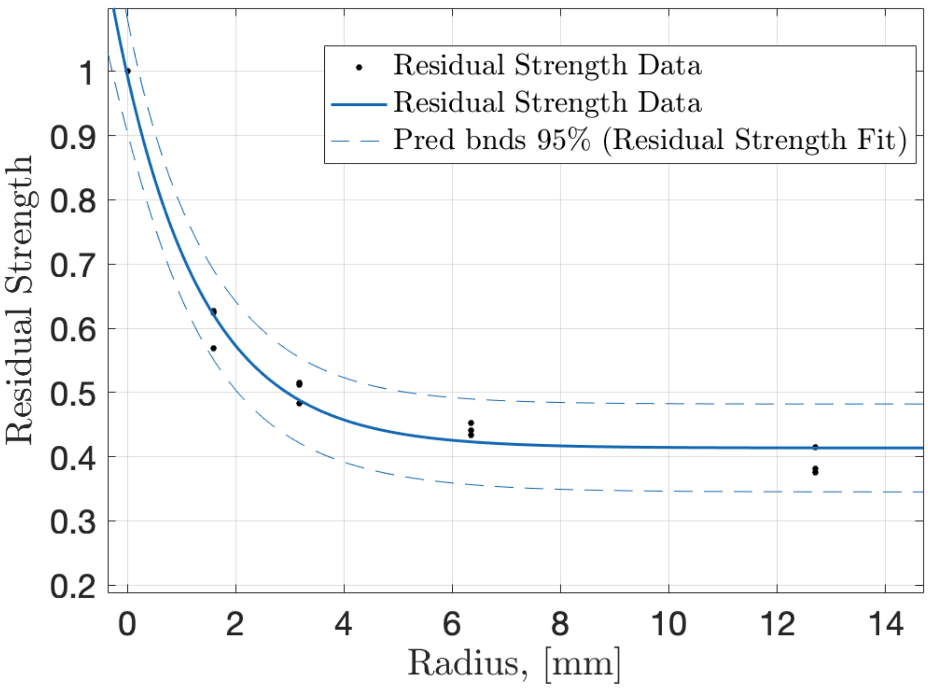

Figure 4.47: Residual strength relative to hole radius. The stress is bounded by 95% Prediction (Confidence) Bounds

Impact Specimen Tensile Tests

Open-hole tension residual strength data has been presented. The goal of OHT was to obtain the residual strength of the laminate as a function of the hole radius and we wish to mimic this experience with impacted specimens replacing holes.

There are two curves per impact energy leve, see Figure 4.48l. Similar to the OHT 3mm diameter specimen exhibiting variability in the OHT strength, so does the damage that is 16.1mm in size.

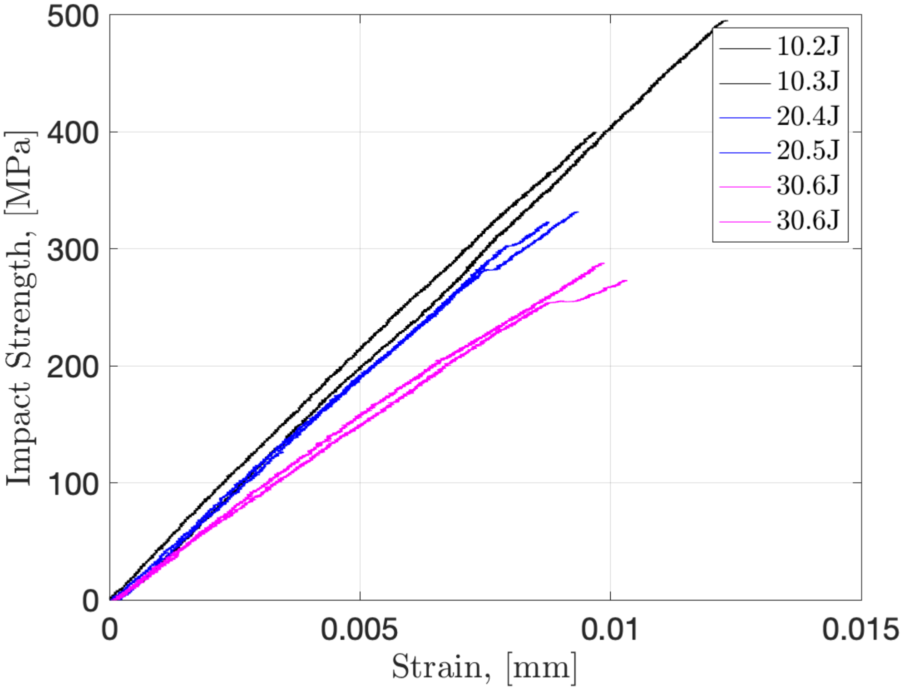

Figure 4.48: Residual Strength relative to hole radius

The impact residual strength data, Figure 4.49is normalized by the max healthy laminate strength, 667 MPa. The impact residual strengths exhibit a softer drop-off relative to the OHT case despite the damage floor being roughly .42, which is slightly elevated relative to the OHT floor of .39. This is encouraging that for similar sized volumetric damage on the larger side has nearly the same floor.

The residual strength was fit with a power curve along with 95% Confidence Bounds.

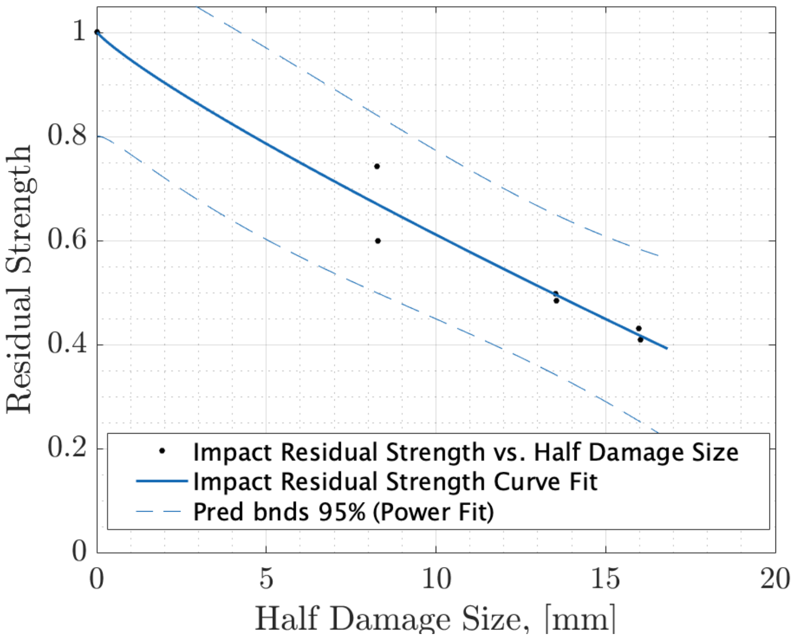

Figure 4.49: Residual impact strength relative to half damage size

Impact and Through-hole Side-by-Side

The resulting Through-hole and Impact experimental residual strengths are given vs their half damage size. For a similar residual strength to a hole, the impact can sustain a large damage size at failure Figure 4.50.

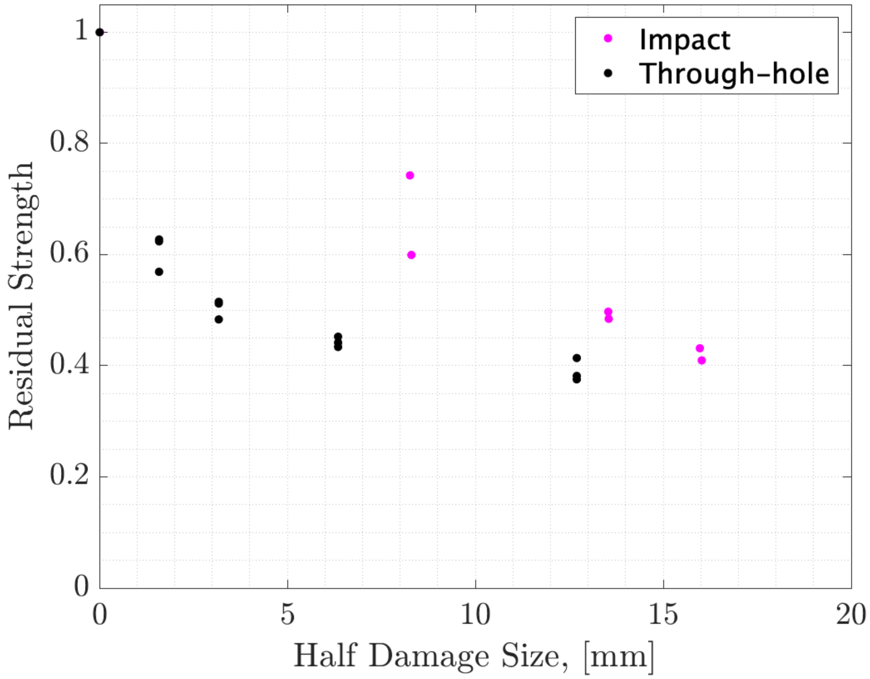

Figure 4.50: Residual Strength relative to hole radius is Black and with the impact Magenta

The impact zone is sensitive to the quantity of backside fiber breakage to that of the material degradation. Considering the desire to correlate residual strengths, it is time to analyze this data in the context of Average Stress Analysis.

4.5 Analysis

It is desirous to effectively measure the impact residual strength from NDE information and relate it to a well-studied fracture process for holes or cracks. After investigating the physical relationship between ultrasonic guided waves from data collected at the conclusion of the WAVSVD algorithm and residual strength of damaged laminates, has shown sufficient evidence that it is possible to estimate residual strength for different Impact Types ($I - V$).

4.5.1 Affected Phase Velocity Curves

Similar to the the WAVSVD Through-hole vs Healthy Aluminum verification test, which showed attenuation of the high frequency and phase velocity dispersion content, so does the CFRP Through-hole and Impact specimen, Figure 4.51. The dashed lines in FIgure 4.51 b,c, and d help delineate the attenuation from the baseline state.

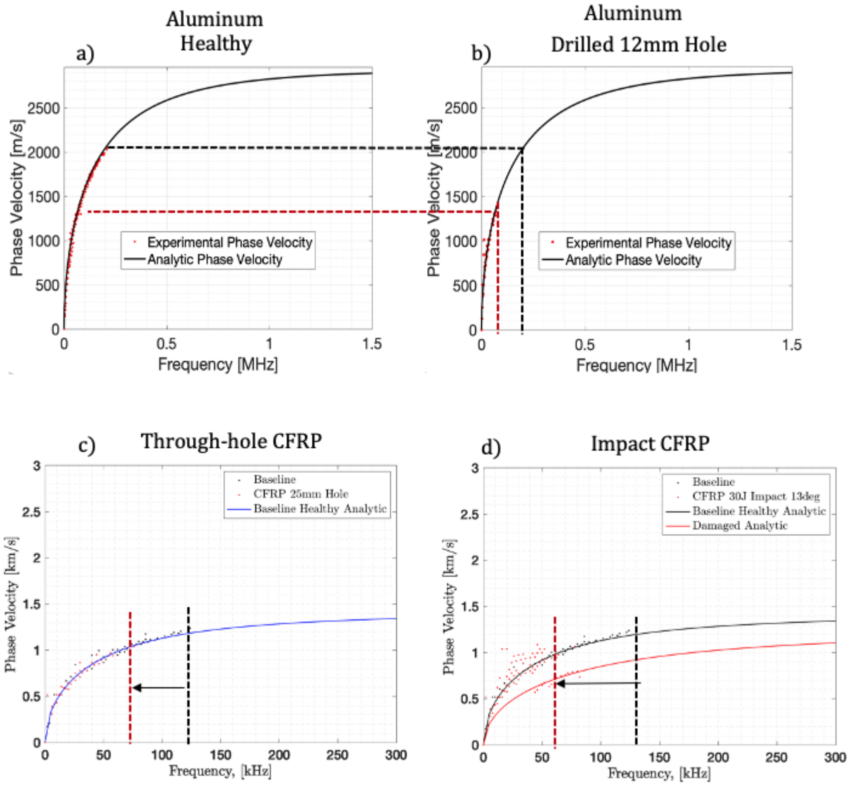

Figure 4.51: Highlighting the attenuation affect volumetric damage has on the UGW signa. a) Healthy Aluminum, b) Aluminum with Drilled Hole, c) CFRP with Drilled Hole, d) Impacted CFRP

This is the first requisite, to find a similar experimental feature in the impact data with the Through-hole data that correlates to residual strength.

4.5.2 Material Damage Spectrum, MDS

Framing the impact SCF_ϵ distribution measured by DIC a weighted mixture of the Ideal Crack $w_1 = .8$ and Through-hole$w_2 = .2$. The key region is to match the strain drop-off to the strain floor. In this case it is possible to frame the general strain distribution field for all the impact. The strains measured from the strain field are only as good as the DIC resolution and selection of the locations to measure. This is can be remedied in the next phase of research. Another consideration to explore, is for the same damage size and needing to fit the two analytic distributions to the experimental data, a change in the Stress Concentration Factor must be adapted. Roughly this is the Average of max strains concentrations in the distribution plot divided the weighting ratio $w_{Hole} = .2$ that helps allocate preference for Average Stress mode, $(\frac{K_t^{exp.}}{.2} \approx 15 = K_t^{equivalent})$.

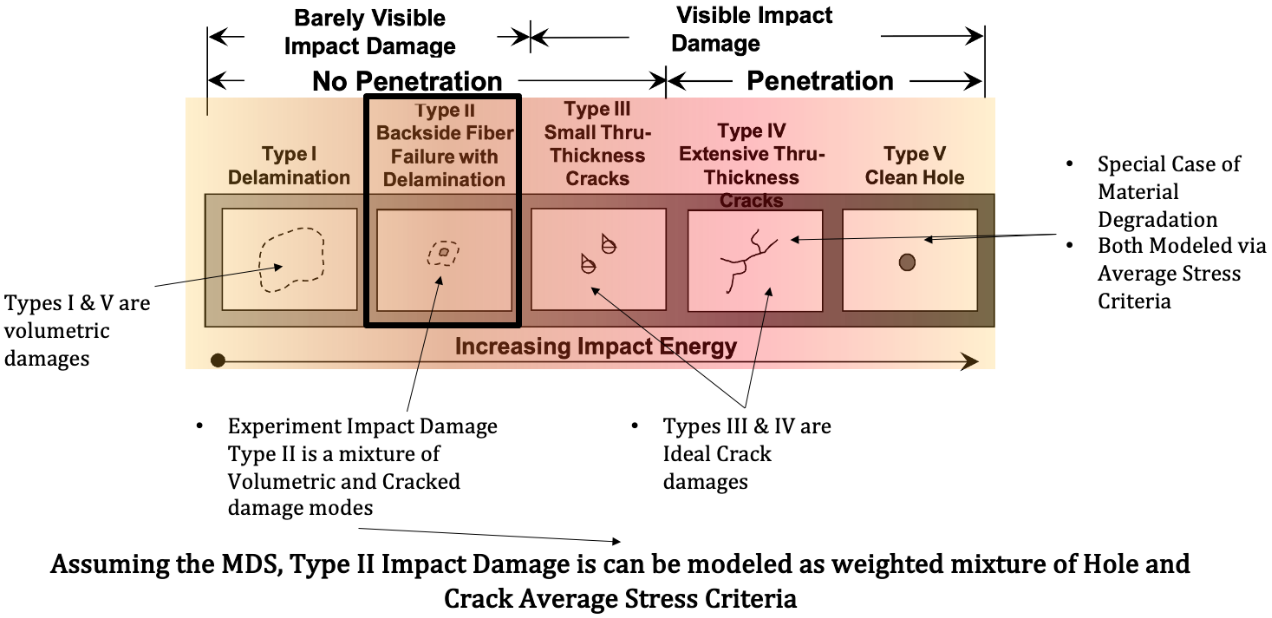

Figure 4.52: Experimentally determined residual strengths for the through-hole and impact specimens with their predicted residual strengths.

4.5.3 Strain Concentration Factor for Hole and Impact Specimens

The Through-hole case neatly follows the Average Stress Criteria model.

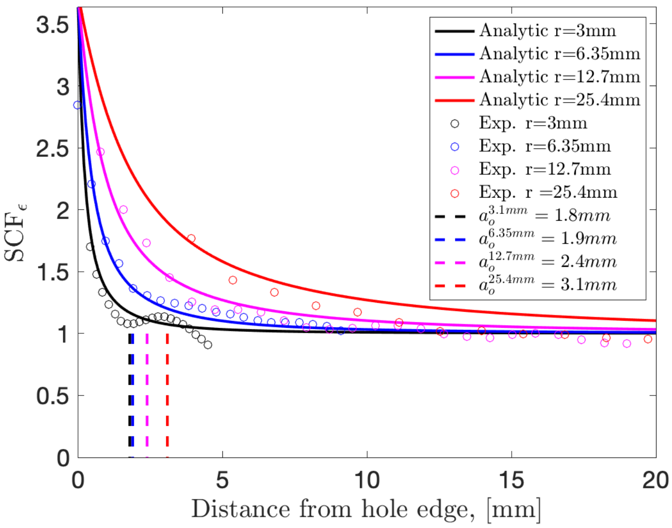

Figure 4.53: Analytic strain distribution with the OHT experimental strains overlaid

Estimating the $SCF_\epsilon = SCF_\sigma$ distribution from the edge of the damage to the edge of the plate was achieved but under the assumption that the impact damage is a mixture of a material degradation and cracking. Experimentally measuring the strain distribution adjacent to the hole was conducted via Digital Image Correlation (DIC) (Correlated Solutions - VIC2D), see Figure 4.54. DIC is a full-field image correlation program and can visualze dispalcements and strains around a discontinuity,(Khechai, Tati, Guerira, Guettala, & Mohite, 2018)

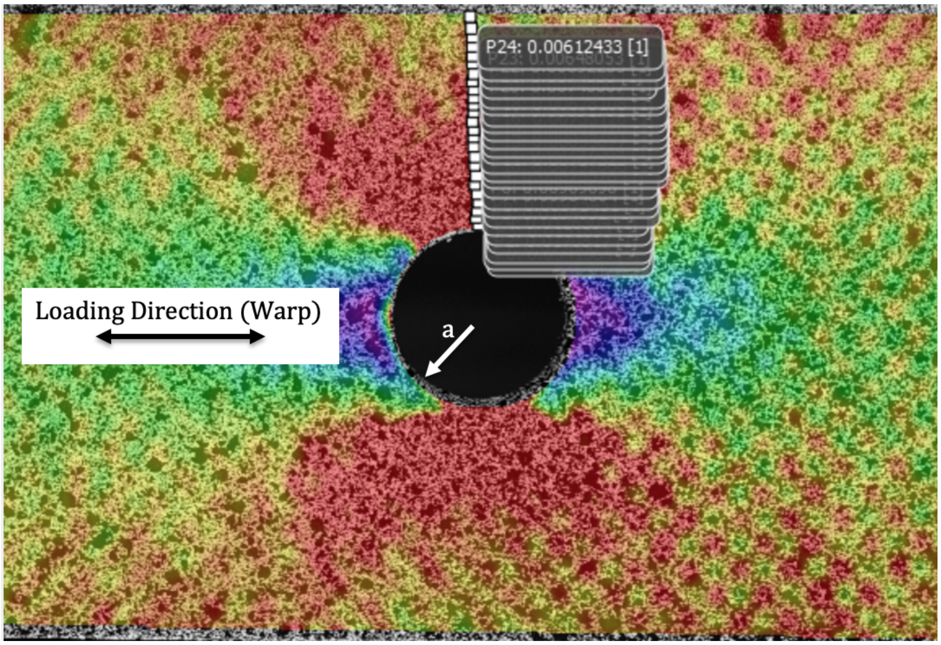

Figure 4.54: Full-field ϵ_{xx} strain distribution for the 12.7mm diameter through hole specimens. The distribution spans the edge of the impact damage to the edge of the plate

The experimental strain distribution was extracted at multiple points along the y axis. There is no sound method for perfectly extracting at a given increments, so the average spatial distribution is used to locate the strain points. All of the impact strains distributions are plotted in Figure 4.55.

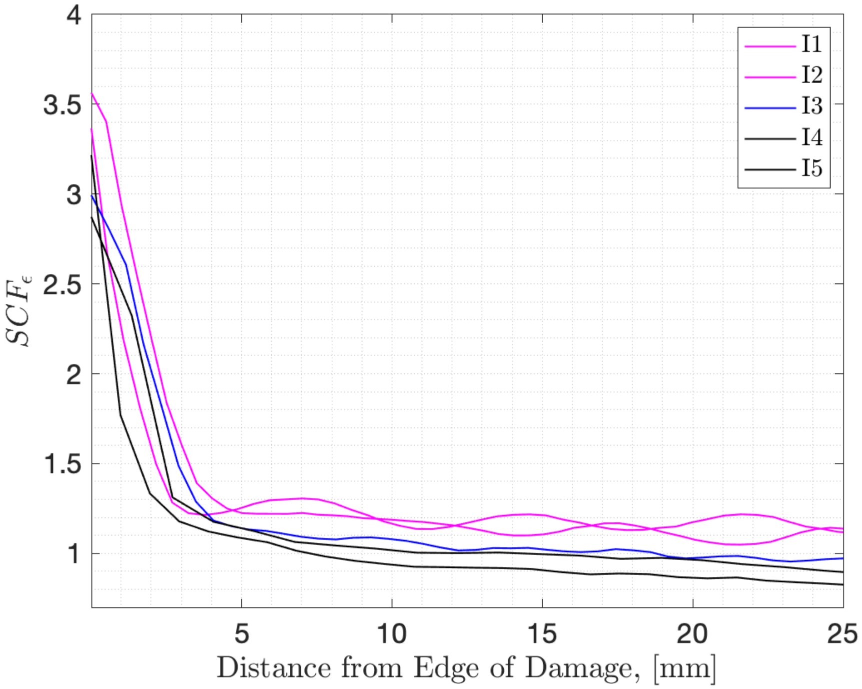

Figure 4.55: Strain distribution for the impacted specimens. The distribution spans the edge of the impact damage to the edge of the plate

The MDS assumes that impacts are a mixture of cracks and material degradation and can be modeled by a combination of crack and hole strain distributions. Figure 4.56.

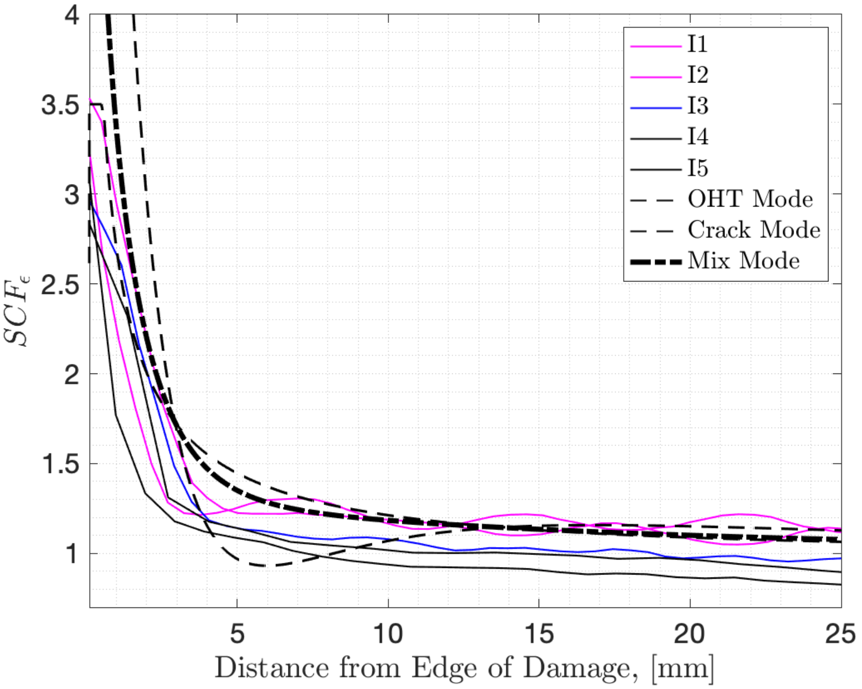

Figure 4.56: Indicating Through-hole and Crack Strain Distribution Modeling

4.5.4 Characteristic Wavelength, a_κ

Calculating the impact or through-hole residual strengths from phase dispersion curves involves extraction of the characteristic damage length, a_κ from the phase velocity. Calculating a_κ requires extracting the max frequency and phase velocity at the attenuated level and substituting in for a_o in Equation 4.30, results in Equation 4.25.

The idea is that the smallest possible wavelength that is not affected by the hole is a strong indicator of a characteristic damage size.

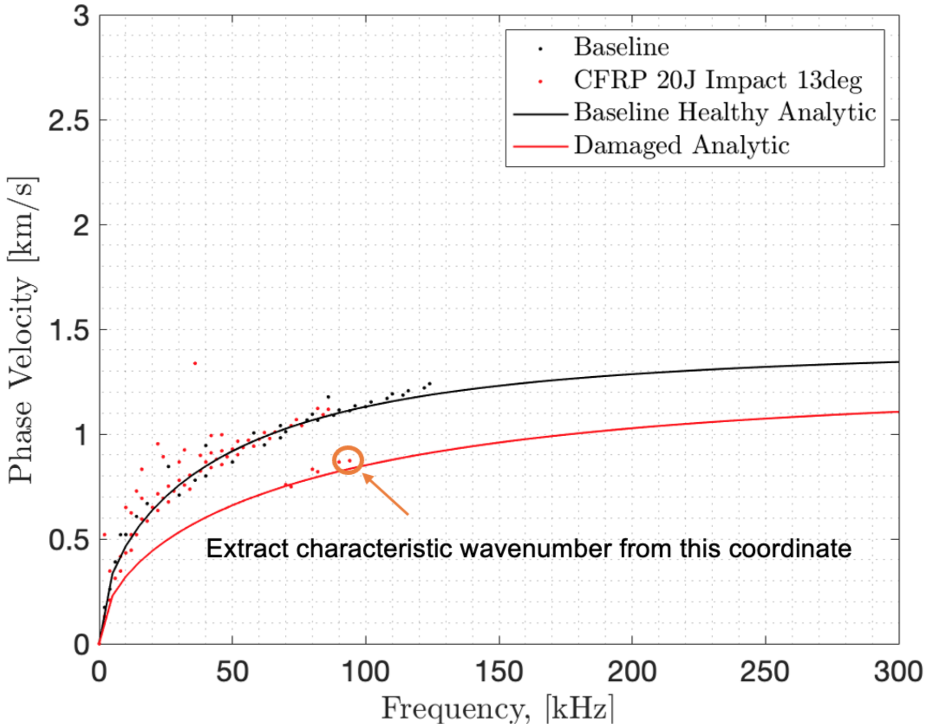

Figure 4.57: Experimentally determined residual strengths for the through-hole and impact specimens with their predicted residual strengths.

This method works for SISDO scanned through-holes, as well as, for SISDO scanned impacts. The residual strength estimate's tendency is towards the conservative.

For the open hole CFRP an estimate of the characteristic wavelength, a_κ is measured and substituted in for a_o. The resulting residual strength estimate is found to be in good agreement with the experimental data, Figure 4.58.

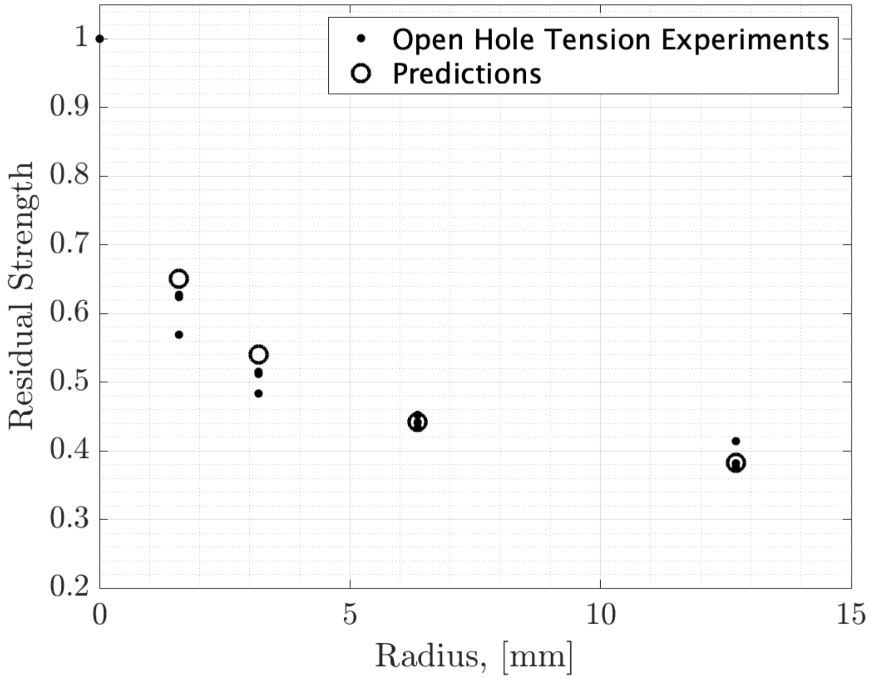

Figure 4.58: Showing the use of characteristic wavelength, a_κ in the Average Stress Criteria SIF equation

4.5.5 Estimation of Fracture Toughness

The analysis goal is multi-faceted with the ultimate goal of predicting residual strength of a damaged component or structure. The analysis begins with extracting a characteristic damage length, a_o and a_κ from the Average Stress Criterion for both OHT and Impact Strength models, respectively. In this case, the well established Through-hole case provides the Fracture Toughness, K_{IC} for the respective damage size. These K_{IC} results are used in Equations 4.25 or 4.30.

Fracture Toughness is a material property and this must be known apriori for deployment of this research to real-life application of this research. In this case, the plane stress created non constant fracture toughness.

4.5.6 Correlating Impact Damage

Observing the phase velocity attenuation in the presence of holes and volumetric impact regions and the observation that the characteristic length, a_o, and characteristic wavelength, a_κ, are near similar. The similarity inspires a substitution of a_o with a_κ for the hole does not affect the residual strength estimate.

The Average Stress Hole Criteria was used to correlate the impact residual strength with the open hole residual strength. The other known is that the Through-hole case is relatable to a Crack. The impact has also generated damage with the assumption being that they crate greater stress concentrations but they are softened by the volumetric material degraded region, since it is already redirecting load paths.

The influence of a crack and the hole-crack relation, means it is possible to relate the impact residual strength to the equivalent damage size with a correction .

Correlating with an Open-hole

The success of the a_κ for the hole case allowed for the generalization to impacts. The procedure is the exact same, just impacted specimens. The goal is to identify the max impact characteristic wavelength from the impacted laminate phase velocity graph.

The main point is that the use of the Average Stress Hole model along with an a_κ substitution generates good estimates of respective cases residual strengths. If the both cases are used the same laminate, then the Fracture Toughness are the same. This assists in the correlation of the impact and hole residual strengths.

The degraded max frequency and phase velocity that corresponds to through-holes or impact damages, as observed in experiment. Therefore the characteristic damage size, a_κ can be measured using characteristic wavelengths indicative of the damage. Substituting a_κ for a_o allows the researchers to predict the residual strength of the Type II and V damage mode By extension, Type II and IV could be estimated.

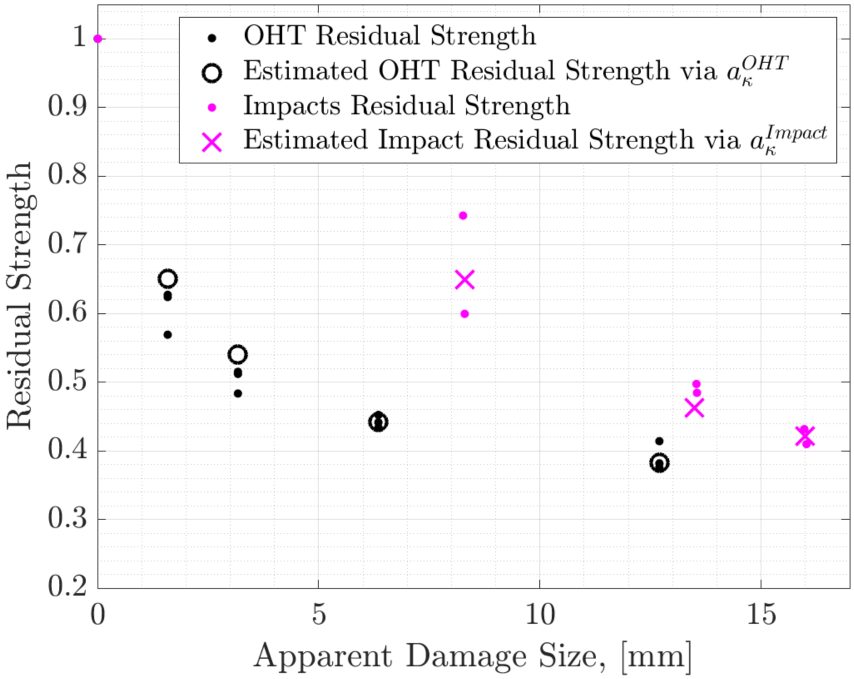

Figure 4.59: Experimentally determined residual strengths for the through-hole and impact specimens with their predicted residual strengths.

The impact residual strengths and open-hole residual strengths from experimentation and NDE approximation via a_κ, are in reasonable agreement. This residual strength correlation can stand alone for use in handbooks.

Two requirements are needed to make full use of this residual strength estimate. They are 1) knowing Fracture Toughness for different damage sizes to compare to impact size and 2) knowing the physical damage geometry in the x-y plane. For either of these they should either be known for the laminate of interest or measurable via an A-scan to locate damage extrema.

Correlating with an Ideal Crack

The full correlation of the Impact case to the Average Stress Model will require the Ideal Crack case to be used. The impact residual strength is only partially correlated at this point. It is correlated in residual strength amplitude but not crack size. This step relates the Impact experiments to the Average Stress Crack Failure Criteria via an equivalent crack, this equivalent crack is actually the size of the shift, root of Equation 4.27 needed to obtain correlation with the impact/hole residual strength correlation.

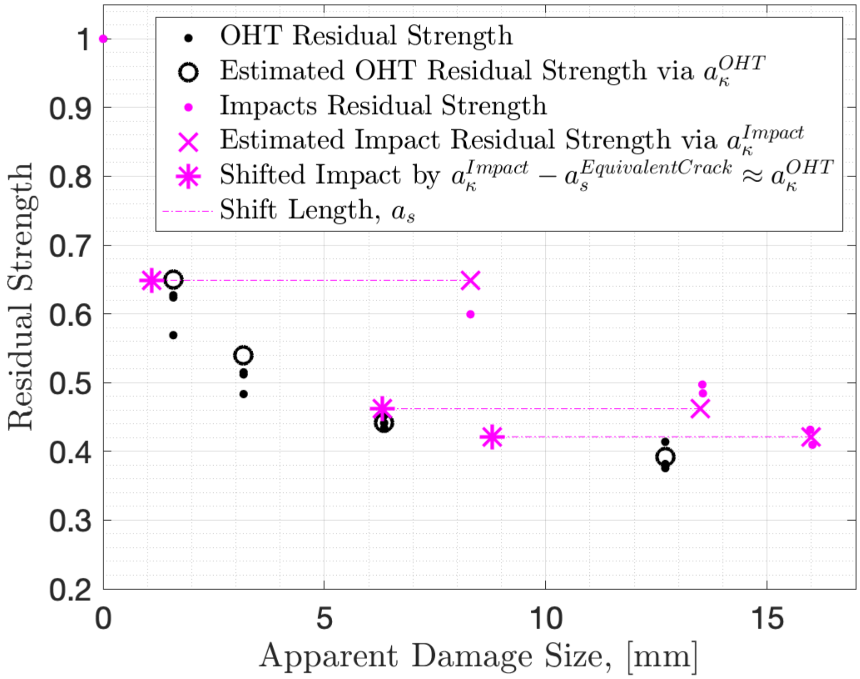

Figure 4.60: Inspection of the impact residual strengths and using an equivalent crack approximate, it was identified that the crack characteristic damage size, a_o^{crack} provides the crack correction length, a_s

Correlated Impact Residual Strength and Featured Damage Size

After finding equivalent residual strengths and equivalent damage sizes, the impacts are reasonably correlated with open holes and cracks. Following the before, during, and post- shift of Figures 4.59, 4.60, and 4.61 highlights ideal crack correlation of the already residual strength correlated impact.

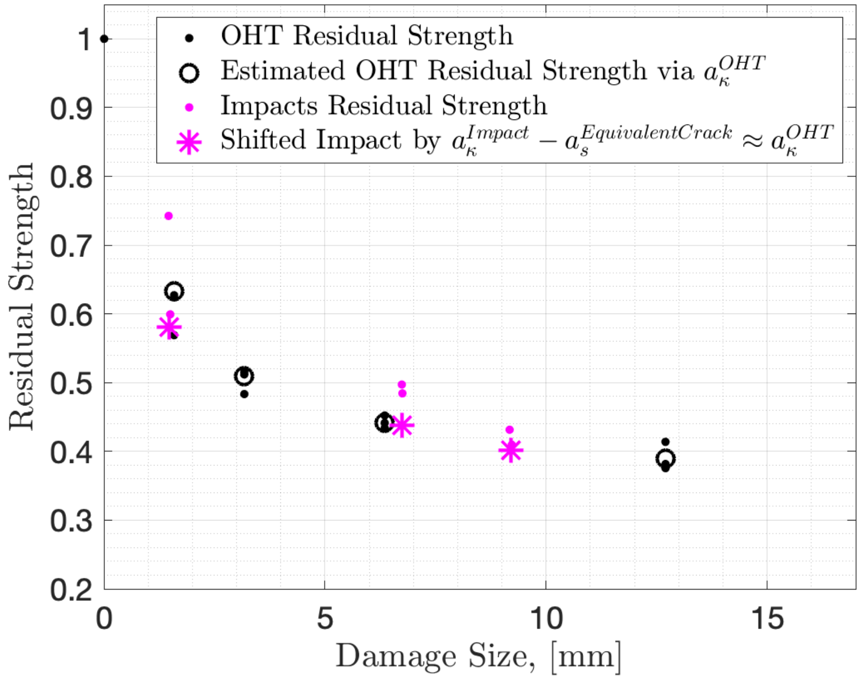

Figure 4.61: Experimentally determined residual strengths for the through-hole and impact specimens with their respective predicted residual strengths and all related to a through hole case.

This exhibits the correlation between impact damaged specimens and the Average Stress Criteria and has applicability to with Equivalent cracks or hole scenarios.

Takeaway Both the Through-hole and Crack Average Stress Models can reasonably correlate with Impact cases. Where the impact residual strength is correlated with the OHT strength via the Average Stress Through-hole criteria. In this correlation where the characteristic wavenumber extracted at the conclusion of the WAVSVD Chapter 3 and is representative of max phase velocity and frequency of the damage and is excited using a specified MI from Chapter 2. It is nice to relate the damage to an equivalent crack size for comparisons between other known geometries, like ellipses or holes, can be made without extensive testing. From this perspective it is also possible and is demonstrated using the Average Stress Ideal Crack criteria and impact residual strength and damage size.

Estimating Impact Residual Strength and Equivalent Crack

1. Collect spatiotemporal data
2. Preprocess the data
3. Generate phase velocity diagrams
4. Extract max frequency and velocity for the damaged case
5. Calculate the characteristic wavelength, a_κ
6. Substitute in a_κ for a_o in the Fracture Toughness equations
7. Calculate correlate impact residual strength with known Fracture Toughness, damage lengths a and a_κ with Equation 4.25
8. Using the damage size and residual strength in the Ideal Crack, calculate the correction length, a_s with Equation 4.27.

Chapter 5

Dissertation Conclusions and Future Work

5.1 Dissertation Conclusions

This dissertation explored and provided a methodology to the question: *How do we estimate the residual strength of a damaged structure with method(s) being straight-forward, field deployable, data-driven, and from noninvasive sources?*

This research navigates the complexities associated with generating high frequency content > 50kHz in aerospace plate structures. A major reason for exciting a plate's high-frequency content is the potential to excite content indicative of damage. This was resolved with the the mini-impactor and suggested applications, a novel modal hammer.

The mini-impactor strikes flat upon the plate with an 1100 Al tip and couple that with the lightweight construction, this tool outperforms traditional impact hammers. A total of 72 plate material-thickness-MI permutations were explored. The data collected was analyzed with two independent techniques: 1) Normalized Residual Energy and 2) Principal Component Analysis. The sought to identify the significant permutations from experimentation that are suggested deployments to pertinent applications. The deployments are either Universal or Plate Material-Thickness. Knowing how to best excite a aerospace structure into the hundreds of kHz range now possible, but a major hurdle still exists. This is the sensitivity of UGW generated by a MI to environmental and operational conditions. All the experiments are conducted in a laboratory setting, which is climate controlled. A modified NRE was deployed and takes consideration of the wavepacket arrival but in this case not concerned with temperature effects. Instead of the phase preserving Hilbert enveloping scheme, a Hanning window was used to isolate the wave packet of interest. The goal was to look at the energy content contained within a single wave packet of interest relative to the baseline average wave packet energy content for either the universal or plate thickness-material deployment perspectives. To enhance the suggested MI deployments, it is suggested that a study be performed to evaluate the influence of aerospace plate material at elevated temperatures and see the suitable range at which the MI can be deployed for the permutation specified when at temperature.

The suggested deployment highlights are contributions to science provided by the Mini-impactor Parameterization study. The major contributions are:

1. Universal Mini-impactor The Universal MI is MI #1, the 4ply x 38mm. This impactor is the physically smallest of all the MIs and seems to be sufficiently

lightweight to extract more energetic frequency content out of structures, refer to 2.16.

2. Material-Thickness Impactor Table

   Table 2.3 was populated from the analyses and suggest the best MI for the plate material-thickness permutation. This would be used if knowledge exists prior to deploying the MI. Where the Universal MI is better used if you do not have knowledge of material and/or thickness.

knowing the data for this research would be ultrasonic guided waves, the WAVSVD algorithm was built to reveal more frequency content in the wavenumber-frequency domain and thus more data points to estimate the phase velocity of a plate. The algorithm uses the Singular Value Decomposition to decompose the prepared data into three matrices, USV^*. Matrices U andV^* are the decomposed signal's perspective patterns resolved into space and time. The singular values matrix S was eliminated from the reconstruction of the dataset eliminating singular values that hid or amplified certain patterns thus presenting an opportunity to mine more information the spatiotemporal data. The end of this version of the algorithm provides a phase velocity dispersion versus frequency curve. The algorithm was validated on 2024 Al, then extended to a 2024 Al with a hole, and then to a CFRP orthotropic plate. During the WAVSVD testing, it was observed in the aluminum plate with and without a hole causes attenuation of the damaged phase velocity estimate is attenuated along the healthy curve, it was observed that impacts behave similarly and this became major revelation in later Chapter 4.

The WAVSVD Chapter contribution to science is the WAVSVD algorithm with these main attributes:

3. A data-driven technique for revealing more phase velocity content
4. The SISDO method records a mixture of healthy and damaged phase velocity content which is mineable

The algorithm is shown to work for all cases and is verified by the analytic solution.

A standing challenge that needs to be addressed to effectively deploy the WAVSVD algorithm is its effectiveness in the face of environmental and operational variability. Optimal baseline subtraction was not explicitly performed in this analysis, but a comparative analysis still exists when observing the phase velocity content of a healthy vs damaged specimen. OBS was not performed during experimentation, namely due to the laboratory setting, and investigations into the affects the environment variability plays in the phase velocity estimate and its resulting influence on the estimation of residual strength.

Looking forward to the next phase of research, it will require the build-up of a baseline datasets in different environmental and operation states to enhance the estimate of residual strength. The question regarding the accurate assessment from NDE signals the residual strength this will start to vary for the same damage size because of altered material moduli and physical geometry of the specimen due to the environmental.

Interestingly, it is shown that the SISDO approach to impacted laminates already provides a the comparative states, see overlay between black and red markers in

4.43. This is a major advantage over traditional scans, but the shortcoming here is the attenuation of the phase velocity content along the healthy dispersion curve. Traditional scans typically encode either damage or healthy, not necessarily at once. SISDO avoids this by scanning ahead, through and behind of the damage, which mixes the baseline state with the damaged state. It is still suggested that an appropriate baseline state be used for OBS to elicit damage features hidden within the data.

Returning to the question of residual strength estimation, an experiment was designed to collect ultrasonic guided wave data generated by a mini-impactor and analyzed by the WAVSVD to provide phase velocity estimates of orthotropic CFRP with varying degrees of material degradation (Prisitine, Hole, or Impact). The nondestructive-destructive correlation required finding a physical metric that relates both phase velocity and strength. The data was generated using MI #8 as the primary excitation source and was selected from Table 2.3 and the WAVSVD algorithm to analyze estimate phase velocity. From the nondestructive side, a characteristic wavelength a_κ was extracted from the max attenuated damage phase velocity content along with damage geometry.

On the destructive side are strength, flaw, and fracture toughness and were all determined in-situ. The damage mode was caused by either drilling or impacting the plate and the strength was tested for under quasi-static displacement control. Fracture Toughness was extracted as a bonus from the next step. Already measuring OHT residual strength for this research, it was possible to estimate fracture toughness from the damage size and failure strength.

The binding framework is the Average Stress Criteria framework and specifically focused on term a_o, and the assertion that damage is a mixture of material degradation and crack, which are the two main components of Average Stress Criteria. This observation prompted the path to finally locating impact residual strength relative to a hole and a crack. DIC was used to extract a near maximum strain data distribution that is normal to the loading direction and starts at the extreme of the damage and terminates at the edge of the plate. It is verified that all of the impact strain distributions are suitable for the Average Stress Criterion because the ideal distributions are able to frame the impact strain distribution in a way that is reflected as a weighted linear combination of the distributions.

As a result of this work, the major contributions to science are related to the correlation of impacts to the Average Stress Criteria:

5. Correlation of Impact and Through-hole Residual Strength.

   The correlation between the impact residual strength and the hole's residual strength, was performed using the experimental data and the Average Stress Criteria for a Through-hole.

6. Correlation of Impact Damage Size and an Ideal Crack

   The correlation between the impact damage size normal to and ideal crack results in the crack correction factor, a_s and is calculated from impact data and the Average Stress Criteria for Ideal Cracks.

7. Average Stress Criteria Correlation to Impacts

   When the two correlations are combined, because they are both only partially describe the total correlation, they bring the impact residual strength into

into agreement with the residual strength and flaw size curves for the original Average Stress models (hole and crack).

5.2 Future Work

The path forward is feasible, but will require some aspects of this dissertation to be studied. They are outlined below:

1. Expand dataset to include environmental and operational variability
2. Automate this NDE system and automate it
3. Optimize the WAVSVD Algorithm for Window Type and Thresholds
4. Update this method to include an inverse optimization scheme that checks the error in estimating material moduli.
5. Explore the impact phase velocity curves nature to allocate phase velocity information to the damage analytic solution from the healthy estimate
6. Expand on test cases that relate impacts to the Average Stress Criteria.
7. Explore the physical relationship between a_κ and a_o.

References

Achenbach, J. D. (2000). Quantitative nondestructive evaluation. *International Journal of Solids and Structures*, *37*(1-2), 13–27.

Bendat, J. S., & Piersol, A. G. (2011). *Random data: analysis and measurement procedures.* John Wiley & Sons.

Blaschke, P., Schneider, S., Kamenzky, R., & Alarcón, D. J. (2017). Non-linearity identification of composite materials by scalable impact modal testing. In *Sensors and instrumentation, volume 5* (pp. 7–14). Springer.

Brunton, S. L., & Kutz, J. N. (2022). *Data-driven science and engineering: Machine learning, dynamical systems, and control.* Cambridge University Press.

Cao, X., Zeng, L., & Lin, J. (2021). Lamb wave mode decomposition and reconstruction based on the viscoelastic propagation model. *Structural Health Monitoring*, *20*(1), 25–45.

Capriotti, M. (2019). *Elastic and thermal wave propagation based techniques for structural integrity assessment.* University of California, San Diego.

Capriotti, M., & Lanza di Scalea, F. (2020). Robust non-destructive inspection of composite aerospace structures by extraction of ultrasonic guided-wave transfer function in single-input dual-output scanning systems. *Journal of Intelligent Material Systems and Structures*, *31*(5), 651–664.

Chen, L., Li, H.-X., & Yang, H.-D. (2020). Spatiotemporal modeling for distributed parameter system under sparse sensing. *Industrial & Engineering Chemistry Research*, *59*(37), 16321–16329.

Chen, Q., Xu, K., & Ta, D. (2021). High-resolution lamb waves dispersion curves estimation and elastic property inversion. *Ultrasonics*, *115*, 106427.

Cui, R. (2021). *Ultrasound based nde/shm techniques for critical components in aerospace and transportation structures.* University of California, San Diego.

Cui, X., Wang, Z., Kang, Y., Pu, H., & Deng, Z. (2018). A robust indicator based on singular value decomposition for flaw feature detection from noisy ultrasonic signals. *Measurement Science and Technology*, *29*(5), 055009.

Daniel, I. M., Ishai, O., Daniel, I. M., & Daniel, I. (2006). *Engineering mechanics of composite materials* (Vol. 1994). Oxford university press New York.

Demené, C., Deffieux, T., Pernot, M., Osmanski, B.-F., Biran, V., Gennisson, J.-L., … others (2015). Spatiotemporal clutter filtering of ultrafast ultrasound data highly increases doppler and fultrasound sensitivity. *IEEE transactions on medical imaging*, *34*(11), 2271–2285.

Farrar, C. R., & Worden, K. (2012). *Structural health monitoring: a machine learning perspective.* John Wiley & Sons.

Flynn, E. B., Todd, M. D., Wilcox, P. D., Drinkwater, B. W., & Croxford, A. J. (2011). Maximum-likelihood estimation of damage location in guided-wave structural health monitoring. *Proceedings of the Royal Society A: Mathematical,* *Physical and Engineering Sciences*, *467*(2133), 2575–2596.

Gardner, C., Ko, Y., Koutoumbas, M., Flynn, E., Cummings, I., & Cornwell, P. (2022). Delamination detection in fiber metal laminates using ultrasonic wavefield imaging. In *Rotating machinery, optical methods & scanning ldv methods, volume 6: Proceedings of the 39th imac, a conference and exposition on structural dynamics 2021* (pp. 59–72).

Gu, J.-F., & Wei, P. (2007). Joint svd of two cross-correlation matrices to achieve automatic pairing in 2-d angle estimation problems. *IEEE Antennas and Wireless Propagation Letters*, *6*, 553–556.

Haeger, A., Schoen, G., Lissek, F., Meinhard, D., Kaufeld, M., Schneider, G., … Knoblauch, V. (2016). Non-destructive detection of drilling-induced delamination in cfrp and its effect on mechanical properties. *Procedia Engineering*, *149*, 130–142.

Halvorsen, W. G., Brown, D. L., et al. (1977). Impulse technique for structural frequency response testing. *Sound and Vibration*, *11*(11), 8–21.

Harner, R. N. (1990). Singular value decomposition—a general linear model for analysis of multivariate structure in the electroencephalogram. *Brain topography*, *3*, 43–47.

Haynes, C. M. (2014). *Effective health monitoring strategies for complex structures.* University of California, San Diego.

He, J., & Yuan, F.-G. (2016). Lamb wave-based subwavelength damage imaging using the dort-music technique in metallic plates. *Structural Health Monitoring*, *15*(1), 65–80.

He, T., Xie, Y., Shan, Y., & Liu, X. (2018). Localizing two acoustic emission sources simultaneously using beamforming and singular value decomposition. *Ultrasonics*, *85*, 3–22.

Henningsson, R., & Fontes, M. (2019). Smssvd: submatrix selection singular value decomposition. *Bioinformatics*, *35*(3), 478–486.

Huber, A. (2018). Robotergestützte zfp mittels luftgekoppeltem ultraschall.

Ida, N., & Meyendorf, N. (2019). *Handbook of advanced nondestructive evaluation*. Springer International Publishing Cham, Switzerland.

Jacobson, E. M., Cummings, I. T., Fickenwirth, P. H., Flynn, E. B., & Wachtor, A. J. (2022). Using steady-state ultrasonic direct-part measurements for defect detection in additively manufactured metal parts. In *Special topics in structural dynamics & experimental techniques, volume 5: Proceedings of the 39th imac, a conference and exposition on structural dynamics 2021* (pp. 59–73).

James, R., Mei, H., & Giurgiutiu, V. (2020). Sh-mode guided-wave impact damage detection in thick quasi-isotropic composites. In *Health monitoring of structural and biological systems xiv* (Vol. 11381, pp. 84–101).

Khechai, A., Tati, A., Guerira, B., Guettala, A., & Mohite, P. (2018). Strength degradation and stress analysis of composite plates with circular, square and rectangular notches using digital image correlation. *Composite structures*, *185*, 699–715.

Kim, H., Welch, D. A., & Kedward, K. T. (2003). Experimental investigation of high velocity ice impacts on woven carbon/epoxy composite panels. *Composites Part A: applied science and manufacturing*, *34*(1), 25–41.

Kim, H. S. (2020). *Ultrasonic guided waves test method for blunt impact damage assessment on composite aircraft structures*. University of California, San Diego.

Kim, J., Hwang, G., Rho, S., & Yoon, S. (2020). Singular value decomposition and 2d crosscorrelation based localization of gas vesicles for super-resolution ultrasound imaging. In *2020 ieee international ultrasonics symposium (ius)* (pp. 1–4).

Kralovec, C., & Schagerl, M. (2020). Review of structural health monitoring methods regarding a multi-sensor approach for damage assessment of metal and composite structures. *Sensors*, *20*(3), 826.

Krzanowski, W. J., & Krzanowski, W. (2000). *Principles of multivariate analysis*. Oxford University Press.

Liu, C., Harley, J. B., Bergés, M., Greve, D. W., & Oppenheim, I. J. (2015). Robust ultrasonic damage detection under complex environmental conditions using singular value decomposition. *Ultrasonics*, *58*, 75–86.

Liu, C., Zang, C., Li, F., & Petrov, E. (2020). High frequency modal testing of the multiblade packets using a noncontact measurement and excitation system. *Shock and Vibration*, *2020*.

Mack, C. A. (2015). More systematic errors in the measurement of power spectral density. *Journal of Micro/Nanolithography, MEMS, and MOEMS*, *14*(3), 033502–033502.

Maierhofer, J., Mahmoudi, A. E., & Rixen, D. J. (2020). Development of a low cost automatic modal hammer for applications in substructuring. In *Dynamic substructures, volume 4* (pp. 77–86). Springer.

Mariani, S., & Cawley, P. (2021). Change detection using the generalized likelihood ratio method to improve the sensitivity of guided wave structural health monitoring systems. *Structural Health Monitoring*, *20*(6), 3201–3226.

McDonough, R. N., & Whalen, A. D. (1995). *Detection of signals in noise.* Academic Press.

Meyendorf, N. G., Nagy, P. B., & Rokhlin, S. I. (2013). *Nondestructive materials characterization: With applications to aerospace materials* (Vol. 67). Springer Science & Business Media.

Mhajna, M., Sadeh, B., Yagel, S., Sohn, C., Schwartz, N., Warsof, S., … Reches, A. (2022). A novel, cardiac-derived algorithm for uterine activity monitoring in a wearable remote device. *Frontiers in Bioengineering and Biotechnology*, *10*, 1187.

Minonzio, J.-G., Talmant, M., & Laugier, P. (2010). Guided wave phase velocity measurement using multi-emitter and multi-receiver arrays in the axial transmission configuration. *The Journal of the Acoustical Society of America*, *127*(5), 2913–2919.

Minonzio, J.-G., Talmant, M., & Laugier, P. (2011). Measurement of guided mode wave vectors by analysis of the transfer matrix obtained with multi-emitters and multi-receivers in contact. In *Journal of physics: Conference series* (Vol. 269, p. 012003).

Miorelli, R., Kulakovskyi, A., Chapuis, B., D'almeida, O., & Mesnil, O. (2021). Supervised learning strategy for classification and regression tasks applied to aeronautical structural health monitoring problems. *Ultrasonics*, *113*, 106372.

ONORATI, R., Sampson, P., Guttorp, P., et al. (2013). A spatio-temporal model based on the svd to analyze daily average temperature across the sicily region. *Journal of Environmental Statistics*, *5*.

Qing, X., Li, W., Wang, Y., & Sun, H. (2019). Piezoelectric transducer-based structural health monitoring for aircraft applications. *Sensors*, *19*(3), 545.

Qing, X., Liao, Y., Wang, Y., Chen, B., Zhang, F., & Wang, Y. (2022). Machine learning based quantitative damage monitoring of composite structure. *International Journal of Smart and Nano Materials*, *13*(2), 167–202.

Rao, J., Qiu, H., Teng, G., Al Mukaddim, R., Xue, J., & He, J. (2022). Ultrasonic array imaging of highly attenuative materials with spatio-temporal singular value decomposition. *Ultrasonics*, *124*, 106764.

Rose, J. L. (2004). Ultrasonic guided waves in structural health monitoring. In *Key engineering materials* (Vol. 270, pp. 14–21).

Rose, J. L. (2014). *Ultrasonic guided waves in solid media.* Cambridge university press.

Salama, K., & Ling, C. (1980). The effect of stress on the temperature dependence of ultrasonic velocity. *Journal of Applied Physics*, *51*(3), 1505–1509.

Sarafin, T. P., & Larson, W. J. (1995). Spacecraft structures and mechanisms: from concept to launch.

Shull, P. J. (2002a). *Nondestructive evaluation: theory, techniques, and applications.* CRC press.

Shull, P. J. (2002b). *Nondestructive evaluation: theory, techniques, and applications.* CRC press.

Singh, A., & Moore, K. (2021). An open-source, scalable, low-cost automatic modal hammer for studying nonlinear dynamical systems. *Experimental Techniques*, 1–18.

Steinbauer, P. (2018). Mechatronic modal hammer.

Sun, W., & Zhang, C. (2018). Analysis and forecasting of the carbon price using multi—resolution singular value decomposition and extreme learning machine optimized by adaptive whale optimization algorithm. *Applied energy*, *231*, 1354–1371.

Tan, S. C. (2017). *Stress concentrations in laminated composites.* Routledge.

Tempelman, J. R., Wachtor, A. J., Flynn, E. B., Depond, P. J., Forien, J.-B., Guss, G. M., … Matthews, M. J. (2022). Detection of keyhole pore formations in laser powder-bed fusion using acoustic process monitoring measurements. *Additive Manufacturing*, *55*, 102735.

Thien, A. B., Chiamori, H. C., Ching, J. T., Wait, J. R., & Park, G. (2008). The use of macro-fibre composites for pipeline structural health assessment. *Structural Control and Health Monitoring: The Official Journal of the International Association for Structural Control and Monitoring and of the European Association for the Control of Structures*, *15*(1), 43–63.

Vallée, J.-C., Ploix, M.-A., Baqué, F., Cavaro, M., & Chaix, J.-F. (2022). Edge and notch detection in a plate using time reversal process of leaky lamb waves. *Applied Sciences*, *12*(1), 228.

Wall, M. E., Dyck, P. A., & Brettin, T. S. (2001). Svdman—singular value decomposition analysis of microarray data. *Bioinformatics*, *17*(6), 566–568.

Wasalathanthri, D. P., Feroz, H., Puri, N., Hung, J., Lane, G., Holstein, M., …

others (2020). Real-time monitoring of quality attributes by in-line fourier transform infrared spectroscopic sensors at ultrafiltration and diafiltration of bioprocess. *Biotechnology and Bioengineering*, *117*(12), 3766–3774.

Welch, P. (1967). The use of fast fourier transform for the estimation of power spectra: A method based on time averaging over short, modified periodograms. *IEEE Transactions on Audio and Electroacoustics*, *15*(2), 70-73. doi: 10.1109/TAU.1967.1161901

Yue, N., & Aliabadi, M. (2020). A scalable data-driven approach to temperature baseline reconstruction for guided wave structural health monitoring of anisotropic carbon-fibre-reinforced polymer structures. *Structural Health Monitoring*, *19*(5), 1487–1506.